Adoption of the LoRa Transmission Protocol for a Low Power Indoor Air Quality Monitoring System

Matthew Meli

Supervisor: Prof. Ing. Edward Gatt

Co-supervisor: Prof. Ing. Owen Casha

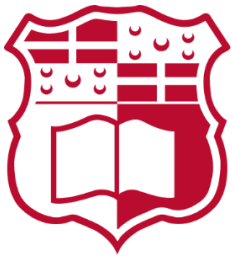

L-Università ta' Malta

Department of Microelectronics and Nanoelectronics

University of Malta

May 2025

Submitted in partial fulfilment of the requirements for the degree of

Doctor of Philosophy (Microelectronics and Nanoelectronics).

Plagiarism Declaration

Plagiarism is defined as “the unacknowledged use, as one's own, of work of another person, whether or not such work has been published, and as may be further elaborated in Faculty or University guidelines" (University Assessment Regulations, 2009, Regulation 39 (b)(i), University of Malta).

I, the undersigned, declare that the Dissertation report submitted is my work, except where acknowledged and referenced.

I understand that the penalties for committing a breach of the regulations include loss of marks; cancellation of examination results; enforced suspension of studies; or expulsion from the degree programme.

Title of Work Submitted:	Adoption of the LoRa Transmission Protocol for a Low Power Indoor Air Quality Monitoring System
Date:	23rd May 2025

Matthew Meli

Student

Signature

Copyright Notice

Abstract

Indoor air quality (IAQ) is a critical, often-overlooked public health concern, driving the need for robust Internet of Things (IoT) monitoring systems to optimise building ventilation and energy efficiency. This research addresses two major gaps: the high power consumption of existing wireless sensor nodes and the lack of cost-effective, scalable big data systems for large-scale IAQ monitoring.

The core contribution is an ultra-low-power, low-cost wireless sensor node integrating state-of-the-art (SOA) sensors for carbon dioxide, volatile organic compounds, particulate matter, temperature, humidity, and pressure. Utilising dynamic power management, a sleep mode current draw of 270 nA and an average active current of 38 mA is achieved. This translates to an overall energy consumption of approximately 327 µAh per hour, and a projected battery life of 40 months on a 10,500 mAh battery. The achieved power efficiency is significantly better than both comparable academic and commercial SOA devices, even while offering a broader range of sensing capabilities.

Complementary to this, the work introduces a cost-effective, LoRa-based big data system for large-scale IAQ monitoring. This system features a novel data forwarding server that calculates Air Quality Index (AQI) and Thermal Comfort Index (TCI) values, storing the enriched data in a document-oriented database. The research also validated a theoretical simulation model for indoor LoRa propagation. Advanced data visualisation was also developed, including a coordinate-based AQI heatmap, enabling smarter building management system (BMS) control.

This research establishes a new benchmark for ultra-low-power, modular IAQ technology, coupled with a proven, scalable big data solution, accelerating the adoption of high-density IoT for healthier, smarter buildings.

Acknowledgments

This dissertation is part of the research work undertaken by the Department of Microelectronics and Nanoelectronics in Environmental Sensors for Air Quality (ESAIRQ), which is a PENTA-EUREKA project co-funded by Malta Enterprise.

I would like to express my deepest gratitude to my family for their unwavering support throughout this journey. In particular, I am profoundly thankful to my wife, whose patience and encouragement made this work possible. Her love and understanding provided the foundation I needed to persevere through the most challenging moments.

I am also sincerely grateful to all the lecturers at the Faculty of ICT for their hard work and diligence, especially my supervisor, Prof. Ing. Edward Gatt, B. Eng. (Hons.), M.Phil., Ph.D. (Sur.), M.I.E.E.E and my co-supervisor, Prof. Ing. Owen Casha, B.Eng. (Hons.) (Melit.), Ph.D. (Melit.), M.I.E.E.E. Their hard work and professionalism motivated me to come this far and also inspired and encouraged me to progress further in my academic career.

List of Publications

To ensure that this research is of peer-reviewed publishable quality, parts of the research work presented have been published in four international peer-reviewed IEEE conferences, ICECS 2020, CSCI 2020, ICOMP 2021 and CSCI 2021. Lecture presentations of the four published research papers were held during these four conferences. Furthermore, a chapter has been published in an open access book.

The published research papers and book chapter along with their abstract are listed below:

1. “A Novel Low Power and Low-Cost IoT Wireless Sensor Node for Air Quality Monitoring”, published in the 27th IEEE International Conference on Electronics Circuits and Systems (ICECS), Glasgow, November 2020.

2. “A Low-Cost LoRa-based IoT Big Data Capture and Analysis System for Indoor Air Quality Monitoring”, published in the 2020 International Conference on Computational Science and Computational Intelligence (CSCI), Las Vegas, December 2020.

3. “An improved novel low power and low-cost IoT wireless sensor node for air quality monitoring”, published in the 22nd International Conference on Internet Computing & IoT, ICOMP '21, Las Vegas, July 2021.

4. “A Novel Modular Low Power and Low-Cost IoT Wireless Sensor Node for Air Quality Monitoring”, published in the 2021 International Conference on Computational Science and Computational Intelligence (CSCI), Las Vegas, December 2021.

5. “Adaptation of the LoRa Transmission Protocol for a Low Power Low-Cost Indoor Air Quality Monitoring System”, published in "Urban Pollution - Environmental Challenges in Healthy Modern Cities", ISBN 978-1-83769-937-7, October 2024.

List of Abbreviations

ABP	Activation by Personalisation
AC	Alternating Current
ADC	Analogue to Digital Convertor
AMQP	Advanced Message Queuing Protocol
API	Application Interface
AQI	Air Quality Index
ASIC	Application Specific Integrated Circuit
BLE	Bluetooth Low Energy
BMS	Building Management System
CoAP	Constrained Application Protocol
COM	Communication Port
DC	Direct Current
DPM	Dynamic Power Management
DSP	Digital Signal Processor
DVS	Dynamic Voltage Scaling
EUI	Extended Unique Identifier
FPGA	Field Programmable Gate Array
GPIO	General Purpose Input Output
GPS	Global Positioning System
HTTP	Hyper Text Transport Protocol
I2C	Inter-Integrated Circuit
IAQ	Indoor Air Quality
IFTTT	If This Then That
IoT	Internet of Things
IPSO	Internet Protocol for Smart Objects
ISM	Industrial, Scientific, Medical
JSON	JavaScript Object Notation
LDO	Low Drop Out
LED	Light Emitting Diode
Li-Ion	Lithium-Ion
LOS	Line-of-Sight
LPP	Low Power Payload
LPWAN	Low Power Wide Area Network
MAC	Medium Access Control
MQTT	Message Queuing Telemetry Transport Protocol

NLOS	Non-Line-of-Sight
OTAA	Over the Air Activation
PCB	Printed Circuit Board
PLR	Packet Loss Rate
QoS	Quality of Service
REST	Representational State Transfer
RF	Radio Frequency
RSSI	Received Signal Strength Indicator
RTC	Real Time Counter
SF	Spreading Factor
SNR	Signal to Noise Ratio
SOA	State-of-the-Art
SPI	Serial Peripheral Interface
SQL	Structured Query Language
TCI	Thermal Comfort Index
UART	Universal Asynchronous Receiver/Transmitter
USB	Universal Serial Bus
WHAN	Wireless Home Area Network
WPAN	Wireless Personal Area Network
WSN	Wireless Sensor Network

Table of Contents

List of Figures

List of Tables

Chapter 1 – Introduction

1.1 – Background

Air quality is increasingly deteriorating due to urbanisation and industrialisation. While outdoor pollution is widely recognised, indoor air pollution is often overlooked, despite people spending approximately 90% of their time indoors. Although certain pollutants enter from the outdoors, a significant number of pollutants are generated indoors through activities like cooking, heating, cleaning, painting, and from materials such as furniture. Inadequate ventilation can cause these indoor pollutants to build up quickly, potentially resulting in health problems such as Sick Building Syndrome and Building Related Illness [1].

In recent years, several entities such as the World Health Organisation and the European Union have established stringent regulations on permissible air pollutant concentrations. As a result, air quality monitoring systems based on the Internet of Things (IoT) have become increasingly popular, especially in the context of controlling indoor environments. Monitoring indoor air quality (IAQ) allows building management systems (BMS) to optimise ventilation, which not only improves energy efficiency but also ensures proper air filtration and the introduction of fresh air, contributing to healthier indoor spaces [1, 2, 3].

Additionally, many state-of-the-art (SOA) air quality sensor nodes documented in current research tend to consume a significant amount of power, often requiring a constant power supply or offering only limited battery operation [4]. Furthermore, these studies frequently lack in-depth analysis of power consumption and comprehensive performance data. This study aims to address these gaps by developing an innovative, low-cost, and energy-efficient wireless sensor node for air quality monitoring, integrating advanced low-power features and extensive sensing capabilities.

Moreover, IAQ monitors are frequently large and costly, making them impractical for widespread use in most buildings. Consequently, buildings that do implement IAQ monitoring often have only a limited number of devices, resulting in sparse, location-specific data [5]. To overcome this limitation, this research introduces the design and development of a cost-effective LoRa-based IoT system for large-scale IAQ data collection and analysis. This approach supports the deployment of numerous sensor nodes across a building, enabling more detailed and comprehensive location-based IAQ monitoring.

1.2 – Aims and Objectives

The main aim of this dissertation is to design, develop, and validate an innovative, low-cost, and energy-efficient IAQ monitoring system capable of supporting large-scale deployment and comprehensive data analysis. This core aim can be broken down into 10 specific objectives below. These objectives define the scope and expected outcomes of the research as demonstrated by the technical chapters and final results presented in the thesis.

1.2.1 – Sensor Node Design and Implementation Objectives

1. Design and implement an innovative wireless sensor node that offers a low production cost and low power consumption for air quality monitoring, exceeding the performance of state-of-the-art SOA commercial and academic alternatives.

2. Incorporate advanced, low-cost sensors to achieve comprehensive air quality monitoring, including measurements of temperature, relative humidity, atmospheric pressure, carbon dioxide, volatile organic compounds, and particulate matter.

3. Utilise and optimise a dynamic power management (DPM) strategy, along with other low-power design features, to maximise battery life to achieve an estimated operational lifespan of at least 16 months.

4. Fabricate and test multiple prototype iterations of the sensor node, comparing the actual power consumption metrics against theoretical models and established SOA benchmarks.

5. Develop a modular sensor node architecture with digital and analogue interfaces to ensure the device is expandable, adaptable, and easily integrated with new sensors for future applications.

1.2.2 – LoRa-based Big Data Capture and Analysis System

6. Develop a cost-effective LoRa-based IoT system architecture for big data capture and analysis that is capable of supporting the widespread deployment of numerous sensor nodes across a large building or campus environment.

7. Develop an integrated theoretical modelling and simulation framework to predict and analyse LoRa link quality, scalability, and packet loss rate (PLR) in a dense indoor setting.

8. Conduct extensive, large-scale deployment of the wireless sensor network (WSN) to collect LoRa metadata and compare these empirical results against the theoretical propagation simulation models to validate and fine-tune network performance.

9. Implement a robust data forwarding server to bridge the LoRaWAN server and database, including data processing steps to calculate the AQI and TCI.

10. Develop a comprehensive set of analytical graphs and visualisations, including a location-specific AQI heatmap, using tools like MongoDB Charts and myDevices to provide detailed, intuitive, and real-time IAQ insights to end-users.

1.3 – Chapters Overview

Chapter 2 explores existing methodologies and ongoing research in WSNs. It begins with a discussion on design constraints and application requirements, followed by an overview of WSN platforms and wireless communication protocols. The chapter concludes with SOA implementations and an analysis of the current research gap.

Chapter 3 focuses on research into wireless sensor nodes, specifically battery power air quality sensor nodes. It details the design of four prototype iterations along with the low-power design methodology used. Additionally, a theoretical power consumption estimation for each iteration is generated.

Chapter 4 presents research on the LoRa-based big data capture and analysis system. It covers the design methodology, the LoRa network architecture, and the big data tools employed. Additionally, a theoretical propagation simulation model for the LoRa network within an enclosed building is introduced.

Chapter 5 discusses the results obtained, emphasising novelty and innovation. It highlights the performance of the wireless sensor node and the big data capture and analysis system during testing.

Finally, Chapter 6 summarises the research, outlining key achievements, potential improvements, and directions for future work.

Chapter 2 – Background and Literature Review

2.1 – Introduction

This section reviews existing methods and recent research developments in the area of WSNs. It begins by evaluating key design constraints and application needs, then explores various WSN platforms and wireless communication protocols. The chapter concludes with an overview of SOA battery powered air quality sensor nodes and SOA LoRa-based systems for large-scale data collection and analysis.

2.2 – Design Constraints & Application Requirements

This section discusses the design constraints of WSNs. Specifically, the application requirements of various WSN applications are discussed.

2.2.1 – Design Constraints

WSN design constraints are established in the initial stages, shaping network specifications and component design. Key constraints include power consumption, operational spectrum, quality of service (QoS), fault management, scalability, congestion, deployment, mobility, security, production cost, and lifespan.

A – Power Consumption

Wireless sensor nodes generally function autonomously and without physical connections, relying primarily on batteries as their power source. Since batteries offer limited and non-renewable energy, it is crucial to design these nodes with energy efficiency in mind to prolong their operational life. This requires implementing low-power strategies across sensing, data processing, and communication modalities. In particular, incorporating power saving mechanisms such as idle and power down modes is vital for maximising the lifespan of the sensor node [6, 7].

B – Operational Spectrum and QoS

Regional spectrum authorities govern the operational frequency ranges and available bandwidth. They also enforce rules on how the spectrum can be used, such as limits on transmission power and duty cycles. Wireless communication protocols must adhere to these regulations, which directly influence the QoS that WSN can deliver. Ensuring a baseline level of QoS is particularly important for real-time and critical WSN applications. Key QoS indicators in WSNs include throughput, PLR, and transmission delay. Meeting these QoS requirements is complex due to challenges like uneven data traffic and limited sensor node energy resources. Hence, the design of compliant and efficient communication protocols is made more difficult [8, 9, 10].

C – Fault Detection, Localisation and Tolerance

Factors such as physical damage, power depletion, or environmental interference, make sensor nodes vulnerable to failure. As a result, incorporating fault detection mechanisms is crucial. Localisation algorithms are also typically integrated into wireless communication protocols to enable automatic fault identification, thereby reducing maintenance time and costs. Furthermore, the resilience of WSN to these faults determines the overall reliability of the network. Ensuring that faults do not disrupt the functionality of the network is key. The wireless communication protocol must be designed to handle potential sensor node failures. This is typically accomplished using adaptive routing and dynamic network configuration algorithms that enhance reliability and resilience [7, 10, 11].

D – Scalability & Congestion

WSN deployments can include anywhere from hundreds to thousands of sensor nodes, with some applications requiring dense placement within confined areas. This density can lead to network congestion and degraded performance. To mitigate these issues and improve network capacity, scalability must be a key consideration in the design

of the wireless communication protocol. Furthermore, if the communication protocol is fixed, scalability can still be enhanced by adjusting the network topology such as deploying additional gateways or relay nodes [7, 8].

E – Deployment

The deployment of sensor nodes can take different forms but is typically categorised into three stages: deployment, post-deployment, and re-deployment. In the initial deployment phase, nodes can be strategically positioned or randomly distributed. The post-deployment phase involves refining the network layout, often by relocating nodes to improve coverage. In the re-deployment phase, new nodes may be added to extend the network or replace those that have failed. The deployment strategy must be decided during the initial design phase, as it significantly influences network dynamics. The form factor and visual impact of the sensor node must also be considered especially in sensitive environments. For example, small low-visibility nodes are critical in battlefields [7, 12].

F – Mobility

Once deployed, sensor nodes may experience mobility, which can occur in two main ways: unintentionally due to environmental factors or intentionally through autonomous capabilities. Whether this mobility is frequent or occasional, it has a significant effect on network behaviour. To handle mobility efficiently, a dedicated mobility management system is required. This system should be incorporated into the wireless communication protocol from the outset to ensure that both routing and medium access control (MAC) algorithms can accommodate movement effectively [8, 12].

G – Security

Security is a critical aspect of many WSN applications, especially in sensitive settings like airports or hospitals. Confidential data within a WSN may include sensor readings, location information, and other context-specific details. In a distributed WSN, this data can

be transmitted in three primary ways: between sensor nodes, from a sensor node to a gateway, and from a gateway to a central server. To protect the integrity and confidentiality of this information, the wireless communication protocol must incorporate strong authentication mechanisms. Furthermore, the design of the WSN must account for potential security threats such as spoofing, passive eavesdropping, denial-of-service attacks, jamming, and sinkhole attacks [9, 10].

H – Production Cost & Lifetime

The overall production cost of a WSN is largely determined by the cost of its sensor nodes and gateways. This cost plays a crucial role in assessing the feasibility of the network, especially for large-scale deployments involving numerous nodes. As a result, incorporating low-cost components into sensor node design is vital for making the network economically viable. At the same time, depending on the intended lifespan of the network; which can vary from a few days to several years, these sensor nodes must also be sufficiently durable and reliable [7, 13].

2.2.2 – Application Requirements

Selecting an appropriate wireless communication protocol is essential and depends heavily on the specific requirements of the application. Table 2.1 outlines the application needs across various WSN use cases. Most applications tend to demand long communication range, low data rates, and high energy efficiency. These conditions are well-suited to low-power wide area network (LPWAN) technologies. In contrast, applications like healthcare typically require short-range communication with high data rates and lower power efficiency, making standards such as IEEE 802.11 and IEEE 802.15 more appropriate. In contrast, for scenarios that demand both long range and high data rates but can tolerate lower energy efficiency, cellular or satellite communication technologies are generally preferred.

Table 2.1 – Wireless sensor network application requirements

Application	Category	Range	Data Rate	Energy Efficiency	Preferred Protocol	Reference
Sniper Localisation	Military Operations	High	High	Low	Cellular/Satellite	[14]
Military Vehicle Localisation	Military Operations	High	Low	High	LPWAN	[15]
Self-Healing Mine Field	Military Operations	High	Low	High	LPWAN	[16]
Outdoor Air Quality	Environmental Monitoring	High	Low	High	LPWAN	[17]
Gas Leak Detection	Environmental Monitoring	Medium	Low	High	LPWAN	[18]
Forest Fire Detection	Environmental Monitoring	High	Low	High	LPWAN	[19]
Ocean Water Quality	Environmental Monitoring	High	Low	High	LPWAN	[20]
Glacier Monitoring	Environmental Monitoring	High	Low	High	LPWAN	[21]
Wild Animal Observation	Environmental Monitoring	High	Medium	High	LPWAN	[22]
Vital Sign Monitoring	Health Care	Low	High	Low	IEEE 802.11/ 802.15	[23]
Chronic Disease Monitoring	Health Care	Low	High	Low	IEEE 802.11/ 802.15	[24]
ECG Heart Monitoring	Health Care	Low	High	Low	IEEE 802.11/ 802.15	[25]
Remote Patient Monitoring	Health Care	Medium	Low	Low	LPWAN	[26]
Avalanche Rescue	Health Care	High	Low	Medium	LPWAN	[27]
Cattle Herding	Farming and Agriculture	High	Low	High	LPWAN	[28]
Plant Disease Monitoring	Farming and Agriculture	High	Low	High	LPWAN	[29]
Agricultural Water Management	Farming and Agriculture	High	Low	High	LPWAN	[30]
Vineyard Monitoring	Farming and Agriculture	High	Low	High	LPWAN	[31]
Distribution Chain	Industry	Medium	Low	High	LPWAN	[32]
Power Consumption Monitoring	Industry	Medium	Low	Low	LPWAN	[33]
Maintenance Scheduling	Industry	High	Low	High	LPWAN	[34]
Home Monitoring	Smart Homes	Medium	Medium	Medium	IEEE 802.11/ 802.15	[35]
Security Access and Monitoring	Smart Homes	Medium	Medium	Medium	IEEE 802.11/ 802.15	[36]
Dumpster Management	Smart Cities	High	Low	High	LPWAN	[37]
Water Leak Detection	Smart Cities	High	Low	High	LPWAN	[38]
Traffic Monitoring	Smart Cities	High	High	Low	Cellular/Satellite	[39]
Parking Management	Smart Cities	High	Low	High	LPWAN	[40]

2.3 – Wireless Sensor Network Platforms

This section provides an overview of WSN platforms, which generally consist of multiple sensor nodes arranged in a specific network topology and connected to one or more gateways. These gateways are linked to servers that offer application programming interface (API) services for end users.

2.3.1 – Sensor Node

A wireless sensor node plays a key role in gathering and processing data, as well as transmitting it efficiently to the nearest sink or gateway. Typically, a sensor node includes one or more sensors or actuators, a microcontroller, a radio transceiver, an antenna, and a power source, as illustrated in Figure 2.1 [6, 7].

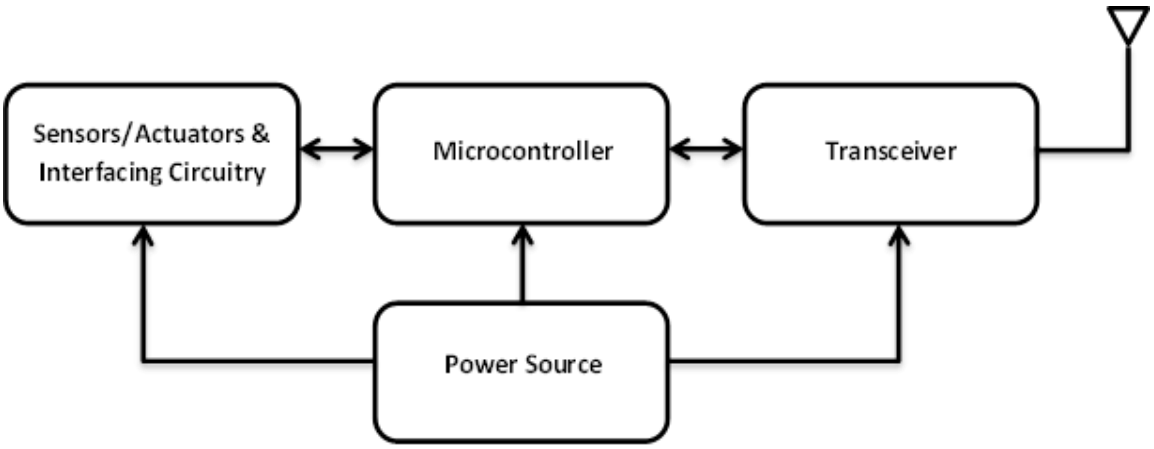

Figure 2.1 – Block diagram of a typical wireless sensor node

A key component of the sensor node is the sensor, which can be of two types either active or passive. Active sensors, like radar or seismic sensors, actively probe the environment, while passive sensors need energy to amplify their analogue signal and do not probe the environment. Passive sensors can be omnidirectional, like temperature sensors, with no directional perception, or narrow-beam, like cameras, with a defined directional focus. Furthermore, sensors can also be either analogue or digital. Analogue sensors make

use of an analogue-to-digital converter (ADC) whereas digital sensors use interfaces like Serial Peripheral Interface (SPI), Universal Asynchronous Receiver Transmitter (UART), or Inter-Integrated Circuit (I2C). Three main factors must be considered during sensor selection: power consumption, accuracy, and cost. The power consumption depends on the average current usage and response time, and is crucial for extending battery life. Often, a balance between accuracy and cost is needed in large-scale networks [6].

The sensor data is managed by a controller, which also oversees the operation of all components and peripherals within the wireless sensor node. These controllers are generally designed with low power consumption and limited processing capability. Flash memory is commonly embedded within the controller to support both device programming and storage of application data. Controllers in sensor nodes may include microcontrollers, field-programmable gate arrays (FPGAs), application-specific integrated circuits (ASICs), or digital signal processors (DSPs). The choice of controller depends on the specific needs for programmability, flexibility, and energy efficiency. Typically, microcontrollers used in sensor nodes operate on 8- to 16-bit architectures with clock speeds ranging from 1 to 24 MHz [6].

Table 2.2 – Wireless Communication Modalities

Technology	Transmission Range	Power Consumption per Burst	Reference
Radio	Medium-Long	~50 µAh	[41]
Infrared	Short	~10 µAh	[42]
Optical	Short	~5 µAh	[43]
Acoustic	Short	~20 µAh	[44]
Inductive	Near-Field	~2 µAh	[45]

To be able to transmit sensor data, nodes are generally equipped with wireless communication capabilities. The transmission range and power consumption characteristics of different wireless communication modalities are gathered in Table 2.2. Inductive coupling has the lowest power consumption but is only suitable for near field communication. Optical and infrared communication also have very low power consumption but have limited broadcasting range and require direct line of sight.

Additionally, acoustic communication has higher power consumption despite the limited range. Radio frequency (RF) technology, while having the highest power consumption among wireless communication options, is widely adopted due to its ability to support medium to long-range transmission using compact antennas. Typically, sensor nodes are equipped with an RF transceiver, which integrates both the transmitter and receiver into a single unit. These RF transceivers commonly operate within the 433 MHz to 2.4 GHz frequency range [6, 7, 12].

The power source in a sensor node typically consists of one or more batteries, delivering an output voltage between 3V and 6V with a capacity ranging from 1000mAh to 6000mAh. These batteries may be either rechargeable or non-rechargeable, with common types including Lithium-Ion (Li-Ion), Nickel Cadmium, Nickel Metal Hydride and Nickel Zinc. In some cases, capacitors are used as an alternative power source. Certain applications may also support energy harvesting methods, such as solar power, to recharge the batteries. The power source is typically connected to a power management circuit, which ensures appropriate voltage levels and facilitates energy-saving strategies. The most commonly implemented power-saving techniques are DPM, which powers down unused components, and dynamic voltage scaling (DVS), which adjusts voltage and clock frequency based on the current processing demand [6, 10, 12].

Table 2.3 shows the specifications and properties of first generation and current sensor node development platforms. Specifically, the specifications of several current predominant LoRa sensor node development platforms are shown. Current generation sensor node development platforms feature faster processors with more resources compared to first generation platforms. However, these newer generation platforms are noted to consume similar or in certain cases less current than their counterparts. The average cost of a typical sensor node development platform with an integrated radio transceiver is around €35. The size of such platforms is generally less than 50 cm^2 and the weight is only a few grams.

Table 2.3 – Sensor node development platforms

Platform	Processor	Radio Transceiver	Sleep Current
Rene 2	Atmel ATmega163	TR1000	1 µA
TelosB	TI MSP430F1611	CC2420	5.1 µA
Mica 2	Atmel ATmega128L	CC1000	15 µA
Mica Z	Atmel ATmega128L	CC2420	15 µA
Shimmer	TI MSP430F1611	CC2420	5.1 µA
Sun SPOT	Atmel AT91FR40162S	CC2420	36 µA
EZ430-RF2500T	TI MSP430F2274	CC2500	100 nA
IRIS	Atmel ATmega1281	AT86RF230	8 µA
Waspmote	Atmel ATmega1281	Libelium	700 nA
ONE	Atmel ATSAMD21G18	RN2483	N/A
Feather	Atmel Atmega32U4	RFM95W	30 µA
LoRa Mini-868	Atmega ATMega328P	SX1276/78	22 µA
mDot	ST STM32F411RET	N/A	40 µA
G76S	ST MCU	SX1276	N/A
LoPy4	Tensilica Xtensa LX6	SX1276 / ESP32	18.5 µA
Mini Ultra Pro V3	Atmel ATSAMD21G18	RFM95W	20 µA
Moteino	Atmel Atmega1284P	RFM95W	2 µA
UX2001	Atmel Atmega32U4	RN2483	N/A
WiMOD Mote II	ST STM32F10CBT6	iM881A	N/A
WisNode-LoRa	ST STM32L	RAK811	N/A
CC1312R1	ARM® Cortex®-M4F	CC1312R	30 nA
CC1310	ARM® Cortex®-M3	CC1310	185 nA
Grasshopper	ST STM32L082	CMWX1ZZABZ	2.1 µA
MKR WAN 1300	Atmel ATSAMD21G18	CMWX1ZZABZ	N/A

2.3.2 – Gateways and Topology

The backbone of a WSN, shown in Figure 2.2, typically comprises one or more gateways connected through a router to an application server. Unlike sensor nodes, gateways are generally not constrained by strict power consumption limits. Their primary role is to forward data packets from sensor nodes to the server. Additionally, gateways support two-way communication, enabling functions such as topology management, authentication, acknowledgments, and firmware updates. Many gateways are also

equipped with a global positioning system (GPS) module to facilitate the localisation of sensor nodes [6, 46].

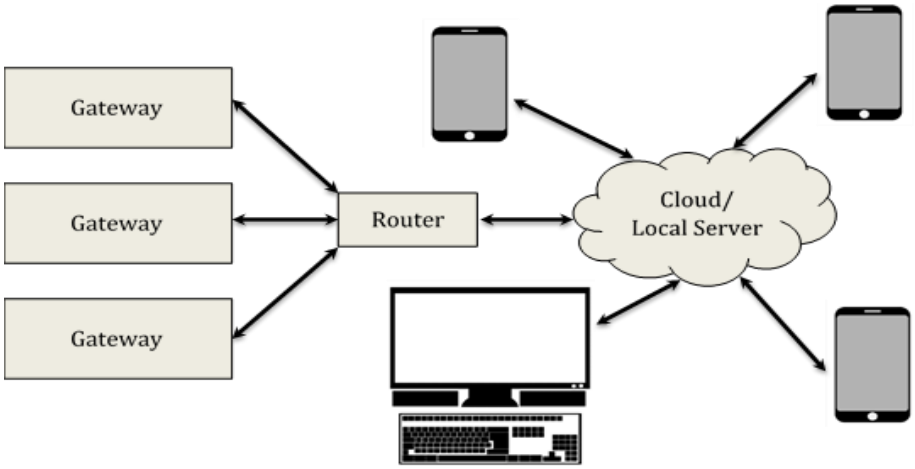

Figure 2.2 – Wireless sensor network backbone architecture

In order to ensure adequate coverage within a target area, the placement of the gateways is critical. To increase coverage, cheaper relay nodes equipped with just packet forwarding capabilities, can be deployed between the sensor nodes and gateways to extend the WSN coverage at a lower cost. Depending on the application, the communication interface of the gateway to the server can be either wired or wireless. Ethernet or fibre optic are generally used as wired interfaces. Alternatively, Wi-Fi and Bluetooth are used for wireless applications. Additionally, satellite or cellular are alternative communication modalities often used for gateways located in more remote areas. [46].

Subject to the arrangement of the gateways and the sensor nodes, the topologies of a WSN, depicted in Figure 2.3, can be of various types. Table 2.4 compares energy efficiency, network robustness, and scalability of different WSN topologies. A star topology consumes the least power but yields the lowest coverage since sensor nodes link directly with a central base station. Contrastingly, a tree topology organises nodes hierarchically for data aggregation, uses additional power and has greater coverage. The mesh topology offers improved reliability and coverage through multi-hop routing but consumes the most

power. Meanwhile, a hybrid topology combines both elements of star and mesh topologies optimising energy consumption whilst maintaining optimal coverage [6, 12, 46].

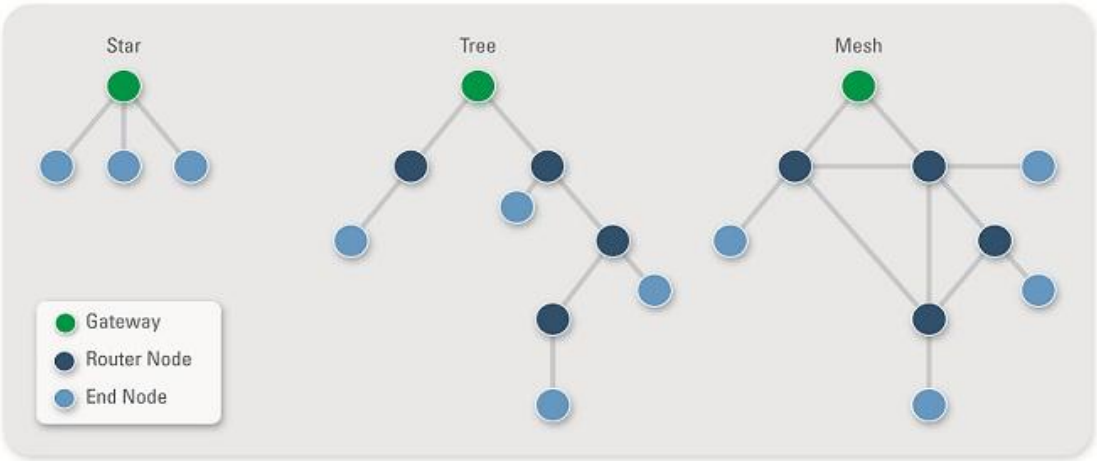

Figure 2.3 – Wireless sensor network topologies

Table 2.4 – Wireless sensor network topology properties

Topology	Power Consumption	Coverage	Multi-Hop	Reference
Star	~0.8 mAh	Low	No	[47], [48]
Tree	~1.2 mAh	High	Yes	[48], [49]
Mesh	~1.5 mAh	High	Yes	[49], [50]
Hybrid	~1.0 mAh	High	Yes	[47], [50]

2.3.3 – Cloud-Based Internet of Things Platforms

Cloud-based IoT platforms are commonly utilised during the development phase of a WSN to monitor network performance and behaviour under various loads and operating conditions. These platforms have largely replaced traditional test beds and are also used to assess the scalability and viability of a WSN by providing analytics such as data rates and PLR. Serving as an application server for the WSN, these platforms offer a range of additional functions, including device management, data collection, analysis, and visualisation [51, 52].

Table 2.5 – Cloud-based IoT platforms

Platform	REST API	Security	Data Collection Protocols	Real-time Analytics	Graphical Visualisations	Open Source
AirVantage IoT	Yes	TLS, SIM	MQTT, CoAP	Yes	Yes	No
Appcelerator	Yes	SSL, Ipsec, AES-256	MQTT, HTTP	Yes	Yes	Yes
Amazon Web Services IoT	Yes	TLS, SigV4, X.509	MQTT, HTTP1.1	Yes	Yes	No
Bosch IoT	Yes	N/A	MQTT, CoAP, AMQP, STOMP	Yes	Yes	No
Carriots	Yes	N/A	MQTT	Yes	Yes	No
Cayenne	Yes	N/A	MQTT, CoAP	Yes	Yes	No
Device Hive	Yes	JWT	MQTT, Web Sockets	Yes	Yes	Yes
DSA	Yes	N/A	HTTP	N/A	No	Yes
Ericsson DCP IoT	Yes	SSL/TLS, SIM	CoAP	N/A	No	No
Eurothech Device Cloud	Yes	N/A	MQTT	Yes	Yes	No
EVRYTHNG IoT	Yes	SSL	MQTT, CoAP, Web Sockets	Yes	Yes	No
Exosite	Yes	SSL	CoAP, Web Sockets	Yes	Yes	No
IBM Watson IoT	Yes	TLS, SSO, LDAP	MQTT, HTTPS	Yes	Yes	No
Intel IoT	Yes	N/A	MQTT	N/A	Yes	No
Google Cloud IoT	Yes	N/A	MQTT, HTTP	Yes	Yes	No
Kaa	Yes	SSL, RSA, AES-256	MQTT. CoAP, HTTP, XMPP. TCP	Yes	Yes	Yes
Lelylan	Yes	SSL/TLS, SIM	MQTT, Web Sockets	Yes	Yes	No
Litmus Loop	Yes	N/A	MQTT	Yes	Yes	No
Microsoft Azure IoT	Yes	SSL/TLS	MQTT, HTTP, AMQP	Yes	Yes	No
ParStream IoT	N/A	N/A	MQTT	Yes	Yes	No
PLAT.ONE IoT	Yes	SSL, LDAP	MQTT, SNMP	N/A	Yes	No
ResIOT	Yes	N/A	MQTT, Web Sockets	Yes	Yes	No
Samsung ARKTIK Cloud	Yes	SSL	MQTT, CoAP, HTTP, Web Sockets	Yes	Yes	No
SiteWhere	Yes	SSL	MQTT, AMQP, STOMP, Web Sockets	Yes	No	Yes
Temboo	Yes	N/A	MQTT, CoAP	Yes	Yes	No
The Things Network	Yes	N/A	MQTT, HTTP	Yes	Yes	No
thethings.iO	Yes	SSL	MQTT, CoAP, HTTP, Web Sockets	Yes	Yes	No
thinger.io	Yes	SSL/TLS	MQTT, CoAP, HTTP	Yes	Yes	Yes
ThingsBoard.io	Yes	N/A	MQTT, CoAP, HTTP	Yes	Yes	Yes
ThingSpeak.com	Yes	N/A	MQTT, HTTP	N/A	No	Yes
ThingWorx PTC IoT	Yes	ISO27001, LDAP	MQTT, CoAP, AMQP, XMPP. DDS, Web Sockets	Yes	Yes	No
WSo2	Yes	SSL	MQTT, HTTP, WSo2 ESB	Yes	Yes	Yes
Xively PaaS IoT	Yes	SSL/TLS	MQTT, HTTP, HTTPS, Web Sockets	N/A	Yes	No
Zetta	Yes	N/A	HTTP	N/A	No	Yes

Table 2.5 shows the properties of predominantly used cloud-based IoT platforms. Amazon, Microsoft and Google IoT platforms have the largest market share. A key feature of these platforms is device management, which includes tasks such as device configuration, measuring received signal strength indicator (RSSI) and signal-to-noise ratio (SNR), location estimation, error handling and reporting, as well as firmware updates. Additionally, most platforms support representational state transfer (REST) API integration, enabling them to expose data and functions through standardised APIs. This integration helps reduce development time, lower costs, and accelerate time-to-market. Another critical aspect is robust encryption for the communication link between the platforms and sensor nodes. Since most sensor nodes are designed to be low-cost and low-power, they can only implement basic security measures. Therefore, the platforms must adopt additional security strategies such as various authentication protocols, security keys, and digital signatures to ensure a high level of protection [52, 53].

2.4 – Wireless Communication Protocols

As detailed previously RF is the predominant communication modality used in wireless sensor nodes and therefore RF communication protocols are reviewed in this section. Table 2.6 gathers the specifications and properties of these wireless communication protocols. IEEE 802.11 technologies are recognised for delivering the highest data rates among wireless standards. However, the range they provide varies significantly based on the operating frequency. For instance, IEEE 802.11n, which operates in the 2.4 GHz and 5 GHz Industrial, Scientific, and Medical (ISM) bands, typically offers a range about ten times shorter than the approximately 1 km range achieved by IEEE 802.11ah using the sub-1 GHz ISM band. These IEEE 802.11 standards also tend to consume a high amount of power. On the other hand, IEEE 802.15 technologies generally provide short-range communication, typically spanning only a few tens of meters. Among these, Bluetooth, ZigBee, and Thread are all IEEE 802.15 protocols, with Bluetooth offering

comparatively higher data rates. Nevertheless, except for classic Bluetooth, IEEE 802.15 technologies are known for their low power consumption.

Table 2.6 – Wireless Communication Protocols

Protocol	Type	Frequency	Range	Maximum Data Rate	Topology	Maximum Devices	Power Consumption	Reference
802.11n Wi-Fi	IEEE 802.11	2.4/5 GHz	40- 100 m	600 Mbps	Star	255	High	[54]
802.11ah Wi-Fi-ah	IEEE 802.11	Sub-1 GHz	1 km	347 Mbps	Star/Tree	8191	Medium	[55]
Bluetooth 2.0	IEEE 802.15	2.4 GHz	40- 100 m	3 Mbps	Star	8	Low	[54],[56]
Bluetooth 4.0	IEEE 802.15	2.4 GHz	40- 100 m	1 Mbps	Star/Mesh	8/32,767	Low	[54],[56]
Bluetooth 5	IEEE 802.15	2.4 GHz	100-200 m	2 Mbps	Star/Mesh	very large	Low	[56]
ZigBee	IEEE 802.15	2.4 GHz	30- 100 m	250 kbps	Star/Mesh/ Tree	250/32,767	Low	[54]
Thread	IEEE 802.15	2.4 GHz	30- 100 m	250 kbps	Mesh	250	Low	[57]
LoRa	LPWAN	Sub-1 GHz	2-5 km	50 kbps	Star of Stars	10,000	Low	[54]
Sigfox	LPWAN	Sub-1 GHz	3- 10 km	1 kbps	Star	1,000,000	Low	[54],[55], [58]
Weightless-W	LPWAN	Sub-1 GHz	5 km	10 Mbps	Star	not defined	Low	[55],[58]
Weightless-N	LPWAN	Sub-1 GHz	3 km	100 bps	Star	1,000,000	Low	[55],[58]
Weightless-P	LPWAN	Sub-1 GHz	2 km	100 kbps	Star	32,767	Low	[55],[58]
Telensa	LPWAN	Sub-1 GHz	2 km	500 bps	Star	5,000	Low	[55],[58]
DASH7	LPWAN	Sub-1 GHz	1-5 km	167 kbps	Star/Tree	100,000	Low	[55],[58]
Ingenu	LPWAN	2.4 GHz	10 km	624 kbps	Star/Tree	384,000	Low	[55],[58]
LTE-M	Cellular LPWAN	Cellular	5 km	1 Mbps	Star	20,000	Medium	[55]
NB-IoT	Cellular LPWAN	Cellular	1-5 km	250 kbps	Star	very large	Medium	[55],[58]
Z-Wave	WHAN	Sub-1 GHz	30 m	100 kbps	Mesh	232	Low	[59]
ANT	WPAN	2.4 GHz	30 m	1 Mbps	Star/Mesh/ Tree	65,533	Low	[60]

LPWAN protocols are known to offer significantly longer ranges compared to IEEE 802.11 and IEEE 802.15 technologies, typically spanning several kilometres while maintaining low power consumption. All LPWAN protocols utilise a star topology, which helps reduce power usage since receivers do not need to continuously listen for messages,

unlike mesh topologies found in IEEE 802.15 networks. Although cellular communication protocols also provide long-range coverage, they tend to consume the most power. Other protocols like Z-Wave, a wireless home area network (WHAN) and ANT, a wireless personal area network (WPAN), have low power consumption but offer limited range. Consequently, LPWAN protocols are preferred for WSN deployments because they combine long-range capability with low energy use. Additionally, the relatively low data rates of LPWAN technologies are adequate for most WSN applications. Specifically, LoRa, an LPWAN technology, not only supports low power consumption but also achieves very high link budgets and strong robustness, making it particularly well-suited for WSN deployments.

2.5 – State-of-the-Art Implementations and Research Gap

SOA implementations highlighting current research work being carried out in the field of WSNs is described in this section. Specifically, SOA battery air quality IoT sensor nodes and SOA LoRa-based big data capture and analysis implementations are presented. The research gap which is not being currently addressed by these SOA works is also presented.

2.5.1 – State-of-the-Art Battery Powered Air Quality Sensor Nodes

SOA battery powered air quality sensor nodes found in literature and commercially available SOA nodes are reviewed in this section.

A – Battery Powered Air Quality Sensor Nodes Found in Literature

Locating sensor nodes with low power consumption proved difficult since most devices typically consume high amounts of energy, necessitating mains power or resulting in limited battery life. Many SOA air quality sensor nodes discussed in the literature, such as those reviewed in [4], which covers recent progress in low-cost indoor air quality monitoring devices, exhibit high-power usage. Furthermore, most of these SOA studies do not provide thorough analyses or detailed results regarding power consumption.

For example, [61], [62], [63] and [64] all present the design of SOA battery powered devices but no information about the power consumption characteristics achieved is mentioned. Similarly, [65], [66] and [67] describe battery powered SOA air quality monitoring devices which are equipped with solar energy harvesting abilities. Once again in these works, detailed power consumption characteristics are not presented. Other SOA battery monitoring devices such as [68], [69] and [70] only achieve limited battery lifetime, this being 160 minutes, 30 hours and 30 hours, respectively.

In [71], a battery powered air quality sensor node for early wildfire prevention is developed. The sensor node measures carbon monoxide, particulate matter, temperature, humidity and wind speed. The sensor node communicates using the LoRa transmission protocol. The developed prototype has a sleep mode current of 34.26 mA and an average active current of 130 mA. Additionally, the sensor node is active for a total of 66 seconds during a read and transmit cycle. If we assume one read and transmit cycle per hour the device results in an average power consumption of approximately 36 mAh. Equipped with a 1600 mAh battery the sensor node can be operated for up to 2 days.

Another air quality monitoring device which achieves similar battery longevity is the work in [72]. In this work a battery powered flue gas air quality node is developed. The sensor node is capable of measuring up to 15 air quality parameters using a combination of infrared and electrochemical sensors. The collected sensor data is transmitted via Wi-Fi to a cloud based service. The proposed device achieves an active current 44 mA, a sleep current of 33 mA and an average current of 38.5 mA. This results in a battery life of approximately 6 days when using a 5000 mAh battery.

In [73], a battery powered IoT node capable of measuring carbon dioxide, temperature and humidity is presented. The carbon dioxide sensor is switched on continuously whilst the other two sensors are only switched on when the carbon dioxide levels exceed a threshold. The collected data is transmitted via Global System for Mobile Communication technology. Adaptive data fetching intervals are employed in order to

minimise power consumption resulting in an average active current of 74.62 mA. Despite using a large 15600 mAh battery, the fabricated device is only capable of reaching a maximum battery life of approximately 9 days.

In [74], another battery powered air quality monitoring sensor node is presented. This time LoRa is used along with Wi-Fi by the authors as the wireless communication protocols. The developed device incorporates electrochemical sensors for carbon monoxide and nitrogen dioxide, along with an infrared sensor for particulate matter detection. It is capable of operating on battery power for up to 26 days when readings are taken every 10 seconds, and up to 45 days with a 10-minute interval between readings. However, the battery capacity used for these estimates is not specified. Additionally, important power consumption metrics such as the sleep mode current, average active current, and average hourly power consumption are not reported by the authors.

In [75], the authors designed another SOA battery-powered air quality sensor node, this time intended for crowd sensing applications. This wearable device features two electrochemical sensors for detecting carbon monoxide and nitrogen dioxide, and it also monitors temperature, relative humidity, and atmospheric pressure. Data is transmitted using a Bluetooth transceiver. The sensor node records a sleep mode current of 500 µA and has an active duration of 16 seconds per read cycle, with an average active current of 15.8 mA. Assuming one read and transmission cycle per hour, the device consumes approximately 568 µAh on average. Equipped with a 600 mAh battery and factoring in a 10% safety discharge margin, the device achieves an estimated operational lifespan of around 40 days.

Another battery powered sensor node for air quality monitoring is developed in [76]. The proposed device is equipped with a LoRa transceiver and it can measure particulate matter, temperature, humidity and atmospheric pressure. The sensor node has a sleep mode current of 1 mA and an average active current of 70 mA over 50 seconds. Assuming one read and transmit cycle every hour the device has an average power consumption of

approximately 2 mAh. A battery life of approximately 3 months is achieved when using a 5200 mAh battery and accounting for 10% safety discharge.

Another notable SOA battery-powered device developed by the authors in [77], is used for ambient monitoring. This device measures temperature, relative humidity, atmospheric pressure, carbon dioxide levels, and light intensity. It uses Wi-Fi as the wireless communication protocol to transmit the collected data. The device achieves a sleep mode current of 10 µA. With an active time of 28 seconds per read cycle and an average active current of 19.89 mA, the average energy consumption per hour is approximately 165 µAh when assuming one read and transmit cycle per hour. Powered by a 1500 mAh battery, and allowing for a 10% safety discharge, the estimated battery life is around 11 months.

The work in [78] presents another battery powered device capable of measuring carbon dioxide, temperature and humidity. Data is transmitted over Bluetooth Low Energy (BLE) and sensors communicate via a mesh network. The proposed device has a sleep current of 41.4 µA and an average current of 130 µA. The authors claim a battery life of approximately 27 months when sampling carbon dioxide every 30 seconds and utilising a 7500 mAh battery. Despite these results, no information is given about how often data is transmitted and how long a read and transmit cycle takes.

Table 2.7 – Specifications of SOA battery powered sensor nodes found in literature

Specification	**[74]**	**[75]**	**[76]**	**[77]**	**[78]**
Temperature/Humidity/Pressure	No	Yes/Yes/Yes	Yes/Yes/Yes	Yes/Yes/Yes	Yes/Yes/No
Carbon Dioxide	No	No	No	Yes (±3%)	Yes (±3%)
Volatile Organic Compounds	No	No	No	No	No
Particulate Matter	Yes	No	Yes	No	No
Additional Sensors	CO, NO2	CO, NO2	No	Light	No
Wireless Interface	LoRa/Wi-Fi	Bluetooth	LoRa	Wi-Fi	BLE
Active time per read cycle	N/A	16 seconds	50 seconds	28 seconds	N/A
Average active current	N/A	15.8 mA	70 mA	19.89 mA	130 µA
Sleep mode current	N/A	500 µA	1 mA	10 µA	10 µA
Average power consumption	N/A	568 µAh	2 mAh	165 µAh	N/A
Battery capacity	N/A	600 mAh	5200 mAh	1500 mAh	7500 mAh
Battery life (10% discharge safety)	~45 days	~40 days	~3 months	~11 months	~27 months

B – Commercially Available SOA Battery Powered Air Quality Sensor Nodes

Several commercially SOA air quality sensor nodes were gathered to obtain a comprehensive view of the current SOA air quality monitoring devices. Similar to SOA nodes found in literature, several commercially available SOA air quality devices have high power consumption and are therefore are mains powered. Examples of such devices include the Awair Element, Purple Air PA-II-SD, uRAD Monitor A3, and the Air Mentor 2S. Others, like the Kaiterra Laser Egg, IQ AirVisual Pro, Honeywell Air Quality Monitor, and PocketLab Air, are battery operated but offer only limited operational time, typically just a few hours or days. Among the battery-powered options, the Airthings Wave Plus stands out with the longest battery life, lasting up to 16 months [79].

Table 2.8 – Specifications of commercial SOA battery powered sensor nodes

Specification	IQAir Visual Pro [80]	Kaiterra Laser Egg [81]	Honeywell Air Quality Monitor [82]	PocketLab Air [83]	Airthings Wave Plus [84]
Temperature	Yes	Yes	Yes	Yes	Yes
Humidity	Yes	Yes	Yes	Yes	Yes
Pressure	No	No	No	Yes	Yes
Carbon Dioxide	Yes (N/A)	Yes (±3%)	Yes (N/A)	Yes (±3%)	Yes (±3%)
Volatile Organic Compounds	No	No	Yes (N/A)	No	Yes (N/A)
Particulate Matter	PM2.5 (N/A)	PM2.5 (±10%)	PM2.5 (N/A)	PM1.0, 2.5,10 (±10%)	No
Additional Sensors	No	No	HCHO (N/A)	Ozone (±15%)	Radon (±20%)
Data Analysis	App + Cloud	App	App	App	App + Cloud
Wireless Interface	Wi-Fi, BLE	Wi-Fi	Wi-Fi	BLE	BLE, 868MHz
Battery	Li-Po (1900mAh)	Li-Po (2200mAh)	Li-Po (2600mAh)	Li-Po (3500mAh)	2xAA (6000mAh)
Battery Life	4 hours	8 hours	24 hours	~3 days	~16 months

The specifications of the commercially available SOA battery powered sensor nodes are gathered in Table 2.8. All the SOA devices listed in the table are equipped to measure temperature, humidity, and carbon dioxide levels. In addition, all except the Airthings Wave

Plus are capable of detecting particulate matter. The Airthings Wave Plus, however, offers measurements of atmospheric pressure, volatile organic compounds, and radon. Likewise, the Honeywell Air Quality Monitor can also detect volatile organic compounds and formaldehyde. While the table includes sensor accuracy where available, this information is missing from many of the product datasheets.

The wireless communication interfaces commonly used by these devices are BLE and Wi-Fi. However, the Airthings Wave Plus also utilises a proprietary 868 MHz-based wireless protocol, enabling it to operate with lower power consumption. These commercially available air quality monitoring solutions typically rely on smartphone applications or cloud-based dashboards for data analysis and visualisation.

2.5.2 – State-of-the-Art LoRa-Based Big Data Capture and Analysis Systems

A number big data capture and analysis systems which are LoRa-based are reviewed in this section. The implementations vary significantly in functionality and deployment environment. A range of environments including rural, urban outdoor, and indoor locations are reviewed. The performance results achieved by LoRa through experimentation in these solutions are analysed and the suitability of LoRa in different environments is hence verified.

A – Outdoor Implementations

A LoRa-based WSN for monitoring the performance and health of solar photovoltaic systems is described in [85]. The solar-powered sensor nodes include sensors for voltage, current, temperature, irradiance, orientation, and tampering detection. For testing, a node was installed on a university campus rooftop, and data was collected using a mobile gateway. Even under non-line-of-sight (NLOS) conditions, the results demonstrated that LoRa could reach a maximum transmission distance of 9.27 km, using a 125 kHz bandwidth and a spreading factor (SF) of 12.

In [86], a severe convective weather warning system based on LoRa is implemented. Sensor nodes, which can be powered via both 220 V alternating current (AC) or 12/24V direct current (DC), are equipped with sensors which measure lightning distance and air pressure at normal time steps. The data is then sent over LoRa and an alarm is raised if threshold values are exceeded. The alarm also triggers continuous monitoring with the sensor nodes utilising a shorter time step in between measurements. When values below the alarm threshold are noted, the alarm is cancelled and the normal time step is re-introduced. The sensor nodes are equipped with LoRa transceivers and a 3dBi antenna, have their gain set to 20 dBm and the frequency of operation is 433 MHz. Experimental results show that a range of more than 2 km was achieved by LoRa.

A LoRa-based vehicle location system is implemented in [87]. Sensor nodes are equipped with a GPS module and transmit their position via LoRa to a gateway. The data is then uploaded to a cloud server to enable users to access the smart transportation system. Four sensor nodes were deployed on buses along with three gateways which were deployed in an urban environment. Experimental results show that the maximum transmission distance with stable coverage, PLR less than 1.5%, is 1.2 km.

Another LoRa-based system proposed in [88] features a water quality monitoring and metering system. The proposed gateways have sensors for both water quality monitoring, such PH and ion sensors, as well as ultrasonic sensors for water metering. A gateway was deployed in an urban city environment and with tests conducted to establish the number of gateways required for optimal coverage. Initial tests showed that a coverage of 2.5 km can be achieved by using a single gateway.

In [89], a smart city pilot project based on LoRa is presented. Sensor nodes are fitted with luminosity, humidity, temperature, and carbon dioxide sensors will be deployed within buildings in the city. The sensed data will then be transmitted using LoRa to a control centre. An experimental test bed was developed by deploying a gateway on top of a 71 m school tower along with a battery powered sensor node moving around the city at a pedestrian

speed. The sensor nodes feature a LoRa transceiver and are equipped with a 2 dBi antenna operating in the 868 MHz frequency band. During testing the transceiver gain is set to 14 dBm, the SF is set to 12 and a bandwidth of 125 kHz is utilised. Experimental results show that stable coverage is attainable up to a range of 2.39 km.

Another LoRa implementation described in [90] features a smart grid is designed to operate in rural areas and allows for real-time remote metering. Sensor nodes are fitted with LoRa transceivers and electricity metering sensors. A 915 MHz gateway is deployed on top of a 10-storey building in a sub-urban area achieving a coverage area radius of 4 km. During testing the transceiver gain is set to 14 dBm, the SF is cycled from 7 up to 12 and a bandwidth of 125 kHz is utilised. Average PLRs of 19.74% and 5.27% are achieved when using a 2 dBi and a 9 dBi antenna, respectively.

In [91], LoRa is proposed as the communication protocol for a marine temperature measurement WSN. Sensor nodes are fitted with temperature sensors to measure the temperature of the ocean. A 433 MHz gateway is initially deployed on top of a 6-storey building in a suburban area. During experimentation, the gain of the LoRa transceivers was set to 20dBm, a value of 10 was used for the SF and a bandwidth of 125 kHz was utilised. PLRs of 0%, 1%, 3% and 10% are observed at distances of 400 m, 700 m, 1 km and 1.4 km respectively.

In [92] a LoRa-based environmental monitoring system for remote and rural areas is presented. The system monitors temperature, humidity, air quality, and sound levels. It is designed in a star topology, with sensors connected to a router node that acts as a relay for the gateway node. The system boasts a reliable long-range communication of up to 2 km in line-of-sight (LOS) conditions.

In [71] a WSN based on LoRa technology for early wildfire prevention is presented. The system consists of several LoRa nodes with sensors to measure environmental variables such as temperature, humidity, carbon monoxide, particulate matter, and wind speed. The

data is sent to a central gateway where it is processed using cloud-based services. Field tests were carried out using different SFs in a suburban environment. The presented work demonstrated a communication range of up to 500 m in NLOS conditions with a single gateway.

B – Indoor Implementations

A LoRa-based WSN industrial sensing solution is implemented in [93]. The sensor nodes are fitted with temperature, humidity, and pressure sensors to monitor environmental conditions within an industrial setting. Five sensor nodes are deployed across a multi-storey industrial building, all connected to a single gateway. During testing, the transceiver gain was varied between 2 dBm and 14 dBm, and different SF settings were tested. The average PLRs recorded were 23%, 18%, 15%, and 11% for SFs of 7, 8, 9, and 10, respectively. These results indicate that the average PLR decreases as the spreading factor increases.

In [94], a LoRa-based WSN is employed to develop a smart paging system designed for elderly care. The system features two types of nodes: a pager node and a wrist monitoring node. The battery-powered pager node enables elderly residents to send a paging signal by pressing a button, while the wrist monitoring node, also battery-powered, is used by nursing staff to track these paging requests. A pager node is installed in each of the 129 rooms within the elderly care facility, and 12 nursing staff members carry wrist monitoring nodes. All nodes communicate with a single gateway located on the middle floor of the building.

A large-scale LoRa WSN for smart indoor environment monitoring was deployed in [95]. The system was set up in a four-story multi-arena centre covering an area of 33,000 m². Battery-powered sensor nodes, each equipped with eight sensors, measured temperature, humidity, air pressure, sound pressure, ambient light, carbon dioxide, acceleration, and magnetic field. Initially, a single gateway was installed to achieve optimal

coverage throughout the centre. For the final deployment, the number of gateways was increased to four to enhance reliability through macroscopic diversity. In total, 33 sensor nodes were strategically placed across the multi-arena centre. During testing, the LoRa transceivers in the sensor nodes operated at a gain of 14 dBm with a SF of 10. Using the 868 MHz frequency band and a bandwidth of 125 kHz, the system achieved optimal coverage with a PLR below 1.2%.

In [96], a LoRa-based WSN is proposed for ship automation and information monitoring. The wireless sensor nodes installed on-board monitor real-time data, enabling preventative maintenance. Additionally, the system reduces the need for cabling, which lowers ship manufacturing costs. Experimental tests were conducted inside the ship to evaluate the performance of LoRa in this enclosed indoor environment. The tests operated in the 433 MHz frequency band with a bandwidth of 62.5 kHz, a transceiver gain of 17 dBm, and a SF of 12. Results demonstrated PLRs of 0% at 110 meters and 5% at 120 meters.

In [97], a LoRa-based monitoring system for underground fire water supply pipelines is presented. The sensor nodes are equipped with pressure sensors and a LoRa module. The system is built on a star topology to address the challenges of long pipe length, signal shielding, and difficult data transmission in underground environments. Through application testing in an underground parking lot, coverage of 700 meters was achieved along with a packet loss rate of less than 4%.

In [98] an indoor wireless sensor network to test a new LoRa link-layer protocol is presented. The protocol is designed to improve the reliability and energy-efficiency of indoor LoRa networks. Booster nodes are used to strengthen packet signals at the gateway and relay packets to end-devices. A real testbed with 20 nodes and a single gateway was deployed inside a 9 x 6 m single storey building having rooms made up of concrete walls. Using SF values between 7 and 10 and a CR of 4/5 the deployed network showed that without booster nodes a PLR of 38% is achieved. However, when 15% of the nodes act as boosters the reliability improves dramatically and the PLR decreases to 5%.

C – Hybrid Implementations

In [99], a WSN designed for safety applications is deployed in a university campus setting. The sensor nodes monitor harmful indoor and outdoor environmental conditions using temperature, humidity, carbon dioxide, and ultraviolet sensors. These wearable nodes are self-sustained through solar energy harvesting. Data collected by the sensors is transmitted via a 915 MHz RFM95 LoRa transceiver with a 3 dBi antenna to a remote cloud server, which provides cloud-based data visualisation. Two wearable sensor nodes are worn by individuals moving around the campus, while a gateway facilitates communication. Experimental results indicate that LoRa achieves a maximum range of 520 meters in dense urban outdoor environments and 230 meters indoors.

In [100], a LoRa-based smart mouse trap WSN is developed. The battery-powered traps include an infrared triggering sensor, a motor driver for cage operation, and battery monitoring circuitry. When triggered or when battery voltage is low, the trap sends status updates over LoRa to a base station, which monitors the status and location of each node. The traps use an 868 MHz RN2483 LoRa transceiver and operate under NLOS conditions. A mouse trap was tested at 5.26 km from the gateway, and packet loss rates PLR were measured with varying transceiver gain and SF settings. A 0% PLR was achieved with a gain of 11 dBm and SF of 12, as well as with SF 11 and gain of 13 dBm. However, when the SF was reduced to 10 and the gain maximised at 15 dBm, the PLR increased to 25%.

Table 2.9 summarises the experimental results from the LoRa WSN implementations discussed in this section. Overall, LoRa demonstrated strong performance in terms of range and PLRs in both outdoor and indoor settings. Additionally, the performance of LoRa generally surpassed that of other LPWAN protocols. However, the observed results fall short of the theoretical maximum performance predicted for LoRa. This performance gap is mainly due to non-ideal operating conditions, such as losses caused by NLOS scenarios, dense cluttered environments, and interference.

Table 2.9 – Specifications of state-of-the-art LoRa implementations

Application	Testing Environment	Environment Type	Sensor Nodes	Gateways	Spreading Factor	Range	PLR	Reference
Solar PV Monitoring	University Campus	Outdoor	1	1	12	9.27 km	N/A	[85]
Severe Weather Warning	Urban City	Outdoor	N/A	N/A	N/A	> 2 km	N/A	[86]
Bus Positioning	Urban City	Outdoor	4	3	N/A	1.2 km	< 1.5%	[87]
Water Quality Monitoring	Urban City	Outdoor	N/A	1	N/A	2.5 km	N/A	[88]
Environment Monitoring	Urban City	Outdoor	1	1	12	2.39 km	N/A	[89]
Smart Grid	Suburban	Outdoor	1	1	7 to 12	4 km	19.74%	[90]
							5.27%	
Marine Temperature Measurement	Suburban	Outdoor	1	1	10	400 m	0%	[91]
						700 m	1%	
						1 km	3%	
						1.4 km	10%	
Air Quality Monitoring	Suburban	Outdoor	N/A	N/A	N/A	2 km	N/A	[92]
Early Fire Detection	Suburban	Outdoor	1	1	7	100 m	0%	[71]
						300 m	20%	
						500 m	70%	
					10	100 m	0%	
						300 m	30%	
						500 m	60%	
					12	100 m	0%	
						300 m	0%	
						500 m	30%	
Industrial Sensing	Industrial Multi-Storey	Indoor	5	1	7	N/A	23%	[93]
					8		18%	
					9		15%	
					10		11%	
Elderly Care Paging System	Elder Care House	Indoor	141	1	N/A	N/A	N/A	[94]
Environment Monitoring	Multi-Arena Centre	Indoor	33	4	10	N/A	< 1.2%	[95]
Ship Monitoring	Ship	Indoor	N/A	N/A	12	110 m	0%	[96]
						120 m	5%	
Water Supply Monitoring	Underground Parking Lot	Indoor	4	2	N/A	700 m	4%	[97]
Protocol Testing	Office Building	Indoor	20	1	7 to 10	<10 m	38%	[98]
			17	4			5%	
Wearable Environment Monitor	University Campus	Outdoor	2	1	N/A	520 m	N/A	[99]
		Indoor				230 m		
Smart Mousetrap	N/A	N/A	1	1	12	5.26 km	0%	[100]
					11		0%	
					10		25%	

Most of the reviewed studies were conducted in varying environments and under different testing parameters. Additionally, the available frequency spectrum and maximum transceiver gain depend on the specific region where the network operates, making direct performance comparisons challenging. Furthermore, some studies omit crucial details such as the gain or SF settings used during testing, while others do not report key outcomes like range or PLR. Despite these limitations, certain patterns and conclusions can still be drawn from the collected data.

The range achieved by LoRa varies significantly based on environmental conditions. In both indoor and outdoor scenarios, the highest range and lowest PLRs were generally obtained using the maximum SF value of 12. However, this setting results in the longest transmission time, which increases power consumption in sensor nodes and may cause greater interference in large-scale WSN deployments. The impact of such interference is not fully captured in these results, as most reviewed implementations involved only a single sensor node and gateway.

2.5.3 – Research Gap

Most SOA air quality sensor nodes reported in the literature exhibit very high power consumption, restricting them to either mains power or very short battery lifetimes. Furthermore, many SOA studies lack detailed analyses and reporting of power consumption metrics. Despite the high manufacturing costs of these SOA devices, their accuracy and sensing capabilities are often quite limited. Therefore, this research focuses on developing innovative wireless sensor nodes for air quality monitoring that offer low power consumption, low-cost, and SOA-level performance alongside comprehensive sensing capabilities.

Additionally, SOA IAQ monitors tend to be bulky and expensive, which limits their practicality for large-scale deployment. The data collected in existing SOA LoRa deployments is also limited, as most involve only a few sensor nodes deployed primarily as

proof-of-concept demonstrations. Consequently, this work aims to develop a scalable, cost-effective big data capture and analysis system. Keeping costs low is essential to facilitate widespread deployment. Distributing multiple nodes throughout a building will generate extensive location-specific IAQ data and LoRa metadata, enabling thorough data analysis.

Drawing from this background and previous research, target specifications to achieve SOA performance have been established. These specifications, outlined in Table 2.10, will guide the WSN design and be used to assess the performance of the implemented device.

Table 2.10 – SOA WSN target specifications

Specification	Target
Sensing ability	Temperature, Humidity, Pressure, Particulate Matter, Carbon Dioxide, Volatile Organic Compounds
Sleep mode current	<10 µA
Battery life	>16 months
Sensor node cost	<€199
Network Size	50+ sensor nodes
Packet loss rate	<1.2%

Specifically, the chosen air quality parameters are: temperature, humidity, pressure, particulate matter, carbon dioxide and volatile organic compounds. This selection directly addresses key limitations identified in current SOA academic and commercial devices. Specifically, many published SOA systems either focus on a limited set of pollutants or omit crucial indicators like volatile organic compounds or particulate matter entirely. While commercial options generally include carbon dioxide, temperature, and humidity, many still lack the comprehensive range of sensing, such as volatile organic compounds and multiple particulate size classifications offered by the proposed node. Therefore, incorporating this comprehensive set of measurements was deemed essential to establish a new SOA benchmark.

Additionally, the choice of parameters to measure represented a critical trade-off between achieving truly comprehensive IAQ monitoring and maintaining low power consumption. While minimising the measured parameters would simplify the design and lower the power draw, this would compromise the core objective of developing an innovative system. To tackle the concern that comprehensive sensing could lead to high power usage, a strategy focused on minimising the active time of the sensors is required. This can be achieved through a DPM policy engineered to dynamically enable or disable each individual sensor and peripheral, ensuring that they are only powered during the brief period required for measurement and transmission, thereby dramatically reducing the overall average energy consumption without compromising the comprehensive nature of the collected data.

Chapter 3 – Sensor Node Design and Implementation

3.1 – Introduction

The research carried out on the proposed low-cost and low power battery powered air quality wireless sensor nodes is discussed in this section. The main components and target specifications are first derived based on the background information collected. Four different iterations of the proposed prototype air quality sensor nodes are then presented. The design methodology along with the theoretical power consumption estimation calculations for each iteration are presented with special attention to the power management circuitry, were a design focused on DPM will be utilised.

3.2 – Main Components and Target Specifications

The previous chapter outlined how IoT wireless sensor nodes function by collecting, processing, and transmitting data to the nearest gateway. These devices are typically untethered and powered by limited, non-rechargeable energy sources, making energy-efficient design a critical priority for maximising battery life. This focus on energy efficiency will be consistently applied throughout the wireless sensor node design process [10, 12].

In air quality monitoring systems, sensor performance plays a central role. The overall effectiveness of the sensor node is determined by the accuracy and sensitivity of the sensors used. Moreover, the choice of sensors influences the requirements for other IoT components such as communication interfaces, voltage compatibility, power demands, operational lifespan, and cost. Since the core objectives of this research are to develop a low-cost, energy-efficient, and comprehensive IAQ monitoring system, sensor selection required a careful evaluation of the trade-offs between accuracy, power consumption, and cost. For instance, while high precision reference sensors exist, their high cost and significant power demands make them unsuitable for a scalable, battery powered network.

Conversely, extremely low-cost electrochemical sensors for gases like carbon dioxide often suffer from significant cross-sensitivity and long-term drift, compromising the objective of reliable data collection [3, 4, 10].

Table 3.1 – Low-cost SOA air quality sensors

Sensor	Sensing Ability	Sensing Accuracy (%)	Response Time (s)	Typical Average Current (mA)	Electric Charge per Reading (mAs)	Input Voltage Level (V)	Interface	Typical Cost (€)
HPMA115 C0	PM 1.0, 2.5, 4.0, 10	±15	6	80	480	5	UART	30
SPS30	PM 1.0, 2.5, 4.0, 10	±15	8	60	480	5	I²C/UART	28
SN-GCJA5	PM 1.0, 2.5, 10	±10	8	100	800	5	I²C/UART	20
SCD30	CO_2, RH, T	±3	20	19	380	3.3 - 5	I²C	35
T6713	CO_2	±3	180	25	4500	3.3	I²C	65
CCS811	TVOC, eCO_2	N/A	1	30	30	1.8 - 3.3	I²C	5
SGP30	TVOC, eCO_2	±15	15	48	720	1.8	I²C/UART	7
iAQ-Core	TVOC, eCO_2	N/A	300	20	6000	3.3	I²C	10
BME680	hPa, RH, T, TVOC	±15	8	12	96	1.8 - 3.3	I²C/SPI	6
BME280	hPa, RH, T	±3%	1	1.4	1.4	1.8 - 3.3	I²C/SPI	3
MICS-6814	CO, CO_2, NH_3	N/A	N/A	88	N/A	5	Analogue	9
MICS-5524	CO	N/A	N/A	32	N/A	5	Analogue	7

Therefore, this work focused on SOA sensors that balance these competing constraints. A selection of these SOA affordable gas sensors was compiled and presented in Table 3.1. This table demonstrates that, despite their low-cost, many of these sensors offer high accuracy and the ability to detect multiple environmental parameters. They support either digital or analogue interfaces and operate within voltage ranges of 1.8 V to 5 V.

Additionally, several sensing alternatives were assessed but omitted following comparison against the specifications. For example, electro chemical sensors, such as nitrogen dioxide or carbon monoxide, were excluded during early design phases due to their high standby power draw and shorter operational lifetime. These choices ensured that the sensor node maintained the desired longevity and compactness objectives. [3, 4, 10].

Furthermore, Table 3.1 lists the specifications for each sensor together with key parameters to understand their power consumption characteristics. Using Equation (1) these parameters are used to calculate the electric charge required per sensor reading. For some sensors, this charge is relatively high, and thus has a significant impact on the battery longevity of the sensor node. Furthermore, the electric charge value for some of the sensors can be further reduced by altering the default measurement rate and utilising low power modes.

$$Q_{Reading}(\mathrm{mAs}) = I_{Average}(\mathrm{mA}) \times T_{Reponse}(\mathrm{s}) \qquad (1)$$

Based on the SOA sensing capabilities defined in the target specifications and the critical trade-offs discussed, the selected sensor suite was chosen for its balanced performance, efficiency, and cost-effectiveness. The SPS30 was favoured for its comprehensive particulate matter detection across multiple size ranges while maintaining moderate power consumption to alternatives like the more power-hungry SN-GCJA5 sensor. Similarly, the SCD30 was chosen to monitor carbon dioxide due to its relatively low power requirements compared to the slower T6713 sensor. In order to monitor volatile organic compounds, the SGP30 sensor was selected as it offers a good balance between accuracy, response time and current draw when compared to similar sensors. Finally, the BME280 which has very low power requirements and an affordable cost, was selected to capture atmospheric pressure, humidity, and temperature data.

Similarly, Table 3.2 presents a selection of low-cost microcontrollers commonly used in IoT applications. These microcontrollers feature bus widths between 8 and 32 bits and

operate at clock speeds ranging from 1 MHz to 120 MHz. They offer up to 512 kB of flash memory and include multiple general-purpose input output (GPIO) pins. Their typical current consumption is only a few milliamps, and most support power-saving modes. Additionally, their cost is generally under €10, making them well-suited for use in this project.

Table 3.2 – Low-cost Microcontrollers used in IoT applications

Microcontroller	Bus (bit)	Speed (MHz)	RAM (KB)	Flash (KB)	GPIO Pins	Typical Current (mA)	Typical Cost (€)
ATmega32U4	8	16	2	32	26	10	4
ATmega1281	8	16	8	128	54	14	6
ATmega328P	8	20	2	32	23	4	3
MSP430F1611	16	8	10	48	48	4	3
STM32L082	32	32	20	192	40	4.5	3
ATSAMD21G18	32	48	32	256	38	5	4
STM32F411CE	32	100	128	512	81	10	7
ATSAMD51J19	32	120	192	512	51	16	10

Hence, the amount of resources required by the specific application determines which microcontroller is selected. In this case, the ATSAMD21G18 was selected for the optimal balance of performance, power efficiency, and resource availability at a moderate price point. With a 32-bit bus operating at 48 MHz, it delivers sufficient processing speed for complex sensor data processing without the higher power consumption of more powerful alternatives. It has a random access memory of 32 KB size and flash memory of 256 KB providing ample space for sophisticated firmware while still outperforming many 8-bit microcontrollers in terms of capability. Additionally, offering 38 GPIO pins, it facilitates flexible connectivity with various sensors and peripherals.

As explained in the previous chapter, IoT sensor nodes typically transmit data using RF technologies, with most transceivers operating in the 433 MHz to 2.4 GHz frequency range. Table 3.3 outlines several low-cost RF transceivers commonly used in IoT systems. While Wi-Fi transceivers provide the highest data throughput, they also consume

considerably more power. On the other hand, Sigfox, LoRa, BLE, and ZigBee transceivers are far more energy-efficient. Specifically, as LPWAN protocols, Sigfox and LoRa offer greater radio link budgets but at lower data rates when compared to ZigBee and BLE. The higher radio link budgets compared to other protocols is crucial for providing wide coverage in large indoor environments such as multi-story buildings.

Table 3.3 – Low-cost radio frequency transceivers used in IoT applications

Transceiver Module	Wireless Protocol	Tx Power (dBm)	Rx Sensitivity (dBm)	Current			Typical Cost (€)
				Tx (mA)	Rx (mA)	Sleep (µA)	
ATA8520	Sigfox	14.5	-121.5	32.7	10.4	0.005	5
RFM95W	LoRa	7/13/17/20	-148	20/29/87/120	10.3	0.2	5
RAK811	LoRa	14	-130	30	5.5	7.2	10
RN2483	LoRa	14	-148	28/39	14.2	2	8
CMWX1ZZABZ	LoRa	14	-135.5	47	23.6	1.4	8
AT86RF230	ZigBee	3	-101	16.5	15.5	0.02	6
CC2420	ZigBee	0	-90	17.4	19.7	1	7
Xbee3 Pro	ZigBee	19	-103	135	15	1.7	25
nRF52805	BLE	4	-97	8	6.1	0.6	3
ESP32	Wi-Fi-n/ BLE	14/0	-93/-89	180/130	95	0.2	4

LoRa is identified as the most appropriate communication protocol due to the ability to support long-range communication with low power consumption. This enables it to cover significantly larger areas than Wi-Fi, ZigBee, or BLE, as demonstrated by the SOA implementations reviewed in [4, 12]. Furthermore, LoRa is an energy efficient protocol. This aligns perfectly with the objective on developing battery-powered wireless sensor nodes with extended operational lifespans. Additionally, the data rate for the IAQ monitoring system is minimal because the collected environmental data is small, only a 42-byte payload size, and only needs to be updated once per hour. The application does not require the high speeds of Wi-Fi but rather a low throughput and high reliability link. Therefore, LoRa is ideal and is more than capable of meeting up the demands with a maximum data rate of 50 kbps. Moreover, LoRa allows for system performance to be optimised by adjusting parameters like bandwidth and SF. This feature enables a tailored trade-off among data rate, coverage, and energy consumption, offering flexibility that other protocols may not.

Specifically, the RFM95W was chosen over its counterparts due to its exceptional balance between performance, energy efficiency, and cost. Operating under the LoRa protocol, it offers versatile transmit power ranges that can be optimised based on range and power requirements, while achieving an impressive receiver sensitivity of -148 dBm. Its moderate current consumption during transmission and reception, along with an extremely low sleep current of 0.2 µA, ensures energy efficiency which is crucial for this application. Moreover, with a typical cost of €5, the RFM95W not only meets the technical demands but also provides a cost-effective solution compared to other transceivers that either compromise on sensitivity or come at a higher price.

Table 3.4 – Prototype sensor node main components and power consumption characteristics

Main Component	Selected Devices	Voltage Level (V)	Active Time (s)	Average Current (mA)	Electric Charge per Reading (mAs)
Sensors	SPS30 [101]	5	8	60	480
	SCD30 [102]	3.3-5	20	19	380
	SGP30 [103]	1.8	15	48	720
	BME280 [104]	1.8-3.3	1	1.4	1.4
Radio Transceiver	LoRa RFM95W [105]	1.8-3.3	1	29	29
Microcontroller	ATSAMD21G18 [106]	3.3	30	5	150

Following this discussion, Table 3.4 summarises the key components chosen for the wireless sensor node along with their typical power consumption characteristics. The table assumes that the sensors are functioning in their default state using standard measurement rates and power modes. Additionally, the LoRa transceiver and microcontroller are assumed to operate in their default modes for 1 second and 30 seconds, respectively. Following these assumptions, Equation (2) is used to derive the active average current which is estimated at 58.68 mA if the maximum active time of the sensor node is considered to be 30 seconds. This value will serve as the initial target specification for designing the initial prototype IoT sensor node.

$$I_{Average}(\text{mA}) = \frac{Q_{Total}(\text{mAs})}{T_{ActiveMax}(\text{s})}$$

$$I_{Average} = \frac{480 + 380 + 720 + 1.4 + 29 + 150}{30} = 58.68\ \text{mA} \qquad (2)$$

Table 3.5 – Prototype sensor node initial target specifications

Specification	Target
Sensing ability	Temperature, Humidity, Pressure, Carbon Dioxide, Volatile Organic Compounds, Particulate Matter
Sensor supply voltage levels	1.8 V, 3.3 V, 5 V
Sensor signal interface voltage	3.3 V
Sensor signal interface	I²C, UART, SPI, Analogue
Wireless Interface	LoRa
Maximum active time per read cycle	30 seconds
Maximum average active current per read cycle	58.68 mA
Maximum sleep mode current	<10 µA
Maximum electric charge (1 read/transmit cycle per hour)	499 µAh
Battery capacity	6387 mAh
Battery life (10% discharge safety)	>16 months

Using the components selected and the SOA performance benchmarks outlined in Section 2.5.3, the initial target specifications for the prototype sensor node are compiled in Table 3.5. The chosen sensor set enables the node to monitor temperature, relative humidity, atmospheric pressure, carbon dioxide, volatile organic compounds, and particulate matter. These sensors require various input voltage levels, specifically 1.8 V, 3.3 V, and 5 V. Since the microcontroller functions at 3.3 V, proper level shifting is necessary for communication across I2C, UART, SPI, and analogue interfaces.

The sensor node is anticipated to carry out one read and transmit cycle per hour and sleep for the rest of the time. Furthermore, the active cycle of the device is expected to last a maximum of 30 seconds. As defined previously in section 2.5.3, a maximum sleep current

draw of 10 µA are required to achieve SOA performance. Using this information and the maximum average active current found previously (2), the maximum target electric charge per hour of the wireless sensor node, 499 µAh, was calculated using Equation (3).

$$Q_{Charge}(\mu\text{Ah}) = \frac{(I_{Active} \times T_{Active}) + (I_{Sleep} \times T_{Sleep})}{1\text{ h}}$$

$$Q_{Charge} = \frac{(58.68\text{ mA} \times 30\text{ s}) + (10\ \mu\text{A} \times 3570\text{ s})}{3600\text{ s}} \approx 499\ \mu\text{Ah} \qquad (3)$$

Furthermore, the maximum target electric charge per hour can be used to determine the battery capacity required in order to achieve the 16-month battery life defined previously. Assuming 10% battery safety discharge allowance the battery capacity required by the wireless sensor node was calculated to be 6,387 mAh using Equation (4).

$$B_{Capacity}(\text{mAh}) = \frac{B_{Life} \times Q_{Charge}}{B_{Safety}}$$

$$B_{Capacity} = \frac{16\text{ months} \times 499\ \mu\text{Ah}}{1 - 10\%} = \frac{16 \times 30 \times 24 \times 499\ \mu\text{Ah}}{0.9} \approx 6387\text{ mAh} \qquad (4)$$

3.3 – 1st Prototype Sensor Node

The 1st prototype sensor node served as an initial proof-of-concept to validate the core sensor suite and LoRa communication. The design was intentionally simplified, combining an off-the-shelf microcontroller board with a custom-designed sensor and power management board. This approach is intended to accelerate development and achieving the ultra-low-power objective is challenging. The microcontroller board selected is the Rocket Scream Mini Ultra Pro V3 [107]. This board, shown in Figure 3.1, was selected as it incorporates the ATSAMD21G18 microcontroller and the RFM95W LoRa transceiver. The board has a built-in 3.3V ME6210A33PG low drop out (LDO) regulator that has a wide input

voltage range of 5 to 10 V. Furthermore, board includes a serial flash chip for data storage, a MAC address chip for device identification and a battery charging circuitry.

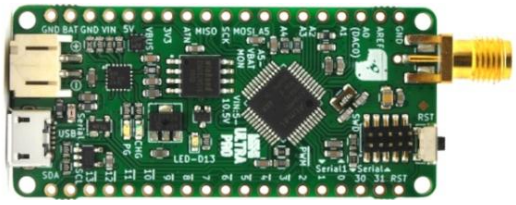

Figure 3.1 – Rocket Scream Mini Ultra Pro V3 microcontroller board

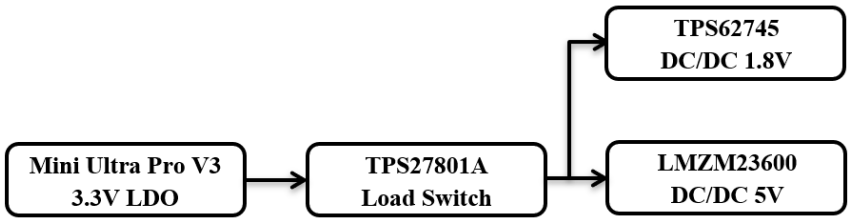

Figure 3.2 – 1st prototype sensor node DPM circuitry

Once the microcontroller board was identified, the sensor interfacing and power management board was designed. The DPM for this iteration was rudimentary, as shown in Figure 3.2. It relied on the 3.3V LDO on-board the microcontroller board and used a single TPS27801A low-power load switch to gate power to the 1.8V and 5V DC/DC converters. The TPS62745 and LMZM23600 were chosen for their high efficiency and low quiescent currents to power the respective sensors. The TPS62745 DC/DC convertor is used to supply 1.8 V to the BME280 and SGP30 sensors while the LMZM23600 DC/DC convertor is used to supply power to the SCD30 and SPS30 sensors. Additionally, the TPS27801A low power load switch, is utilised to isolate the 1.8 V and 5 V DC/DC convertors from the 3.3 V LDO on the Mini Ultra Pro V3.

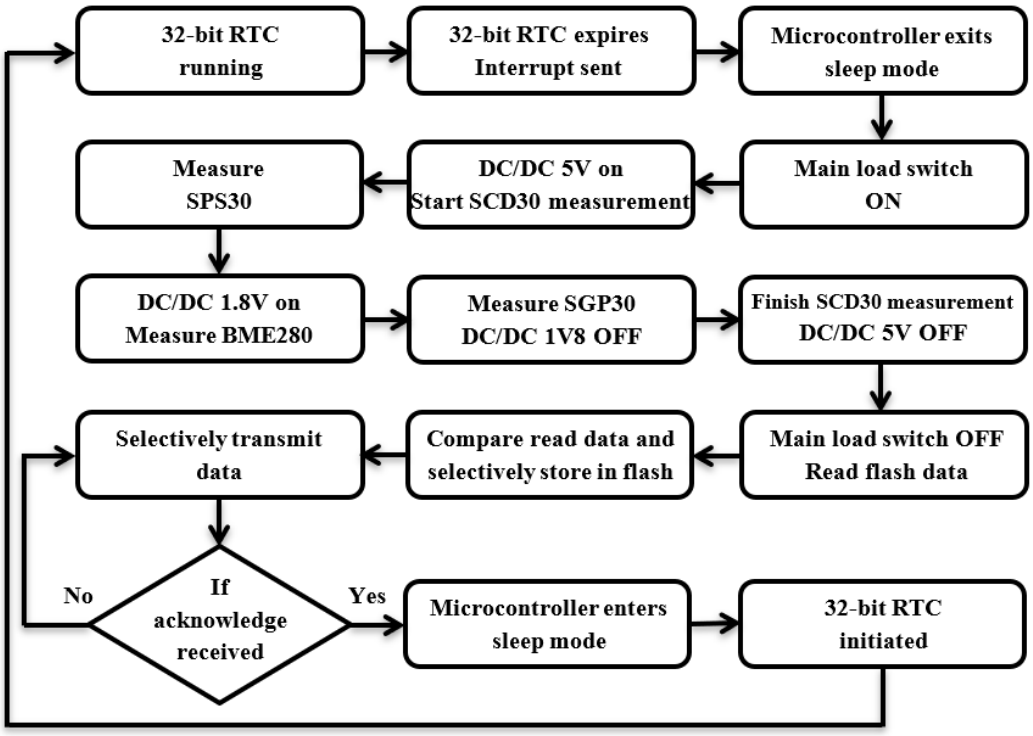

Figure 3.3 – 1st prototype sensor node procedural flowchart

A procedural flowchart describing this program is shown in Figure 3.4. The 32-bit real-time counter (RTC) expires and triggers a wake-up call to from the sleep state of the microcontroller. The main load switch is then switched on followed by the 5 V DC/DC convertor which powers on the SCD30 and SPS30. Since the SCD30 measurement is the longest one out of all the sensor measurements, this is the first one which is initiated. Since the 5 V DC/DC converter is already active, the SPS30 sensor measurement is performed first. Next, the 1.8 V DC/DC converter is enabled to allow the BME280 and SGP30 sensors to take their readings. Once these measurements are completed, the SCD30 sensor reading is carried out, after which the 5 V DC/DC converter is turned off, followed by the main load switch. This sequential control of power supplies is part of the DPM strategy to minimise energy consumption by powering down sensors when not in use. The collected sensor readings are then compared to previously stored flash data, and only any differences are updated in memory. The data is formatted using the Cayenne Low Power Payload (LPP)

protocol and transmitted selectively via the LoRa transceiver. After a successful transmission, the microcontroller enters sleep mode and the RTC is reset.

Table 3.6 – 1st Prototype Sensor Node Theoretical Power Consumption

Description	Device	30 Second Read and Transmit Cycle					Sleep Time (s)	Typical Sleep Current
		Active Time (s)	Typical Active Current	Idle Time (s)	Typical Idle Current	Electric Charge (mAs)		
Mini Ultra Pro V3	ME6210A33PG [d08]	30	1.6 µA	0	1.6 µA	0.048	3570	1.6 µA
	ATSAMD21G18 [106]		5 mA		4 µA	150		4 µA
	RFM95W [105]		29 mA		200 nA	870		200 nA
	W25Q16JVSNIM [109]		20 mA		10 µA	600		10 µA
	24AA025E64T [110]		3 mA		1 µA	90		1 µA
Sensors	SPS30 [101]	8	60 mA	12	8 mA	576	0	OFF
	SCD30 [102]	20	19 mA	0	OFF	380	0	OFF
	SGP30 [103]	15	48 mA	0	OFF	720	0	OFF
	BME280 [104]	1	1.4 mA	14	100 nA	1.401	0	OFF
Power Management	TPS27801A [111]	20	30 nA	10	30 nA	0.001	3570	30 nA
	TPS62745 1.8V [112]	15	400 nA	5	130 nA	0.007	0	OFF
	LMZM23600 5V [113]	20	7 µA	0	OFF	0.14	0	OFF

The theoretical power consumption characteristics of this 1st prototype sensor node are gathered in Table 3.6. Once again, a single transmission cycle per hour is considered and assumed to take 30 seconds. The average electric charge during a single transmission cycle is calculated for each device using Equation (5). Additionally, by summing the resulting electrical charge values for each device, the theoretical average active current of the proposed device was calculated to be equivalent to 112.9 mA using Equation (2). In sleep mode all the devices on the Mini Ultra Pro V3 as well as the TPS27801A are not fully switched off. The combined sleep mode current of these devices should theoretically result in a total sleep mode current of 16.8 µA. Furthermore, using Equation (3), the theoretical total electric charge per reading was calculated to be approximately 958 µAh.

$$Q_{Reading}(\text{mAs}) = \left(I_{Average}(\text{mA}) \times T_{Active}(\text{s})\right) + \left(I_{Idle}(\text{mA}) \times T_{Idle}(\text{s})\right) \quad (5)$$

This initial prototype revealed excessive idle current draw and limited control over peripheral states, which highlighted the need to further integrate dynamic power management features in subsequent revisions. Lessons from this version informed the transition towards increased autonomy in power domain switching strategies, improving alignment with low-power deployment objectives.

3.4 – 2nd Prototype Sensor Node

This 2nd iteration was designed specifically to solve the high sleep current problem of the 1st prototype. The primary design choice was to abandon the off-the-shelf board and integrate all components, including the ATSAMD21G18 microcontroller and RFM95W transceiver, onto a single custom board. This allowed for a complete re-design of the DPM strategy. Furthermore, this 2nd integration enables more precise control over the power usage of peripheral devices such that the sleep mode current is reduced significantly when compared to the 1st prototype node. Moreover, the C++ code written for this prototype is optimised to put devices such as the RFM95W and W25Q16JVSNIM into sleep mode when not being used. Once again, the target specifications set initially were followed and the main components were kept unaltered.

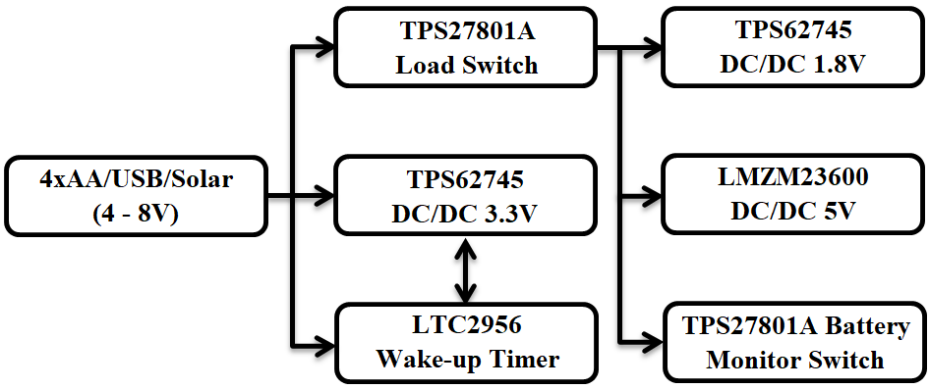

Figure 3.4 – 2nd prototype sensor node DPM circuitry

The power management circuitry, illustrated in Figure 3.4, was developed following a significant advancement of the DPM architecture. The core component of this circuitry is the LTC2956 low-power wake-up timer. This timer was chosen because it could operate independently and activate the main TPS62745 3.3V DC/DC converter when it expires. This in turn powers up the entire microcontroller and its peripherals. This allows the microcontroller to be in a true off state, rather than a deep sleep mode and therefore bypassing the ~4 µA sleep current of the ATSAMD21G18. Unlike the previous design, the 3.3 V LDO found on the off-the-shelf microcontroller board no longer constrained the power management architecture.

Table 3.7 – 2nd prototype sensor node DPM devices

Device	Device Type	Input Voltage	Output Voltage	Output Current	Shutdown Current	Quiescent Current
TPS62745 [112]	DC/DC	3.3 - 10 V	1.8 V, 3.3 V	300 mA	130 nA	400 nA
LMZM23600 [113]	DC/DC	4 - 36 V	5V	500 mA	1.8 µA	7 µA
TPS27081A [111]	Switch	1.8 - 8 V	1.8 - 8 V	3 A	30 nA	30 nA
LTC2956 [114]	Timer	1.5 - 36 V	1.5 - 36 V	N/A	300 nA	800 nA

The specifications of the DPM devices used in the design of this 2nd prototype are gathered in Table 3.7. These specific TPS62745 and LMZM23600 DC/DC convertors were selected for their high efficiency and, critically, their very low shutdown and quiescent currents ensuring minimal leakage when disabled. The overlapping input voltage ranges of these components define the input voltage range for the prototype sensor node, which is established to be between 4 and 8 V. This allows multiple power supplies to be used to power up the prototype sensor node. The allowable options include 4 x AA batteries, 5 V universal serial bus (USB) and 6 V solar. Another limiting factor when selecting the power management devices is the input current requirements of the sensors and other on-board devices. The output current of the power management devices must be able to supply the required current to these devices.

Three low-power DC/DC converters are employed to generate the required 1.8 V, 3.3 V, and 5 V supply rails. The 1.8 V converter powers the SGP30 sensor, while the 3.3 V converter supplies the BME280 sensor, the microcontroller, the LoRa transceiver, and other peripherals including the flash memory and MAC ID chip. The 5 V converter is dedicated to powering the SCD30 and SPS30 sensors. In alignment with the DPM strategy, a low-power load switch is used to disconnect the 1.8 V and 5 V converters from the main power supply when not in use. An additional load switch controls power to a potential divider circuit used for monitoring the input voltage. The DPM framework is further refined with the integration of a low-power wake-up timer, which governs the activation of the main 3.3 V converter. The sleep duration of this timer is adjustable, ranging from two minutes to two hours, by configuring different jumper positions on a resistor array.

Figure 3.5 presents a flowchart outlining the logic of the implemented C++ code. When the wake-up timer expires, it activates the main 3.3 V DC/DC converter, which powers up the microcontroller. Upon start-up, the microcontroller runs an initialisation routine and then enables the main load switch to begin the measurement process. As part of the DPM strategy, the measurement routine involves sequentially enabling specific power supplies. First, the load switch connected to the potential divider is briefly activated to measure the battery voltage. Next, data is collected from the BME280 sensor. Following this, the 5 V DC/DC converter is switched on to begin the SCD30 sensor measurement. While the SCD30 sensor is collecting data, the SPS30 and SGP30 sensors are also measured. Once the SCD30 reading is complete, the 5 V converter is turned off, concluding the sensor measurement routine. Subsequently, the main load switch is turned off. The collected data is then formatted and selectively transmitted via the LoRa transceiver. After a successful transmission, the system sets a flag indicating that the wake-up timer has completed, and the 3.3 V DC/DC converter is powered down. This action turns off the microcontroller and restarts the sleep cycle, awaiting the next timer-triggered wake-up.

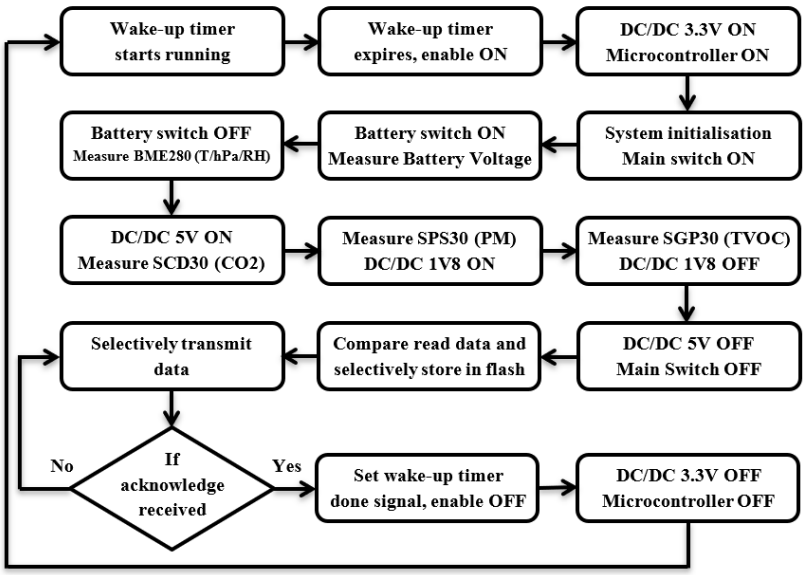

Figure 3.5 – 2nd prototype sensor node procedural code flowchart

Additionally, the continuous switching on and off of the sensors in the proposed DPM strategy is a common challenge in battery powered IoT devices that can affect sensor accuracy. For most low-power sensors, just waiting for the first reading is often not enough, as the initial data points may be unstable or reflect transient states. However, the design of the prototype node explicitly incorporates procedures to mitigate this risk, ensuring that the sensors stabilise and produce accurate readings within the active measurement cycle. The implemented measurement routine accounts for the sensor specific response and start up times within the total 31 second active window before reading and storing the final values.

For example, the SCD30 measurement is initiated first and is allotted its full 20 second response time. This response time is defined as the time it takes to reach $T_{63\%}$ which is a standard metric used in sensor data sheets to quantify the sensors response time to a sudden change in physical quantity. Given that the changes in air quality are slow, this full period ensures the sensor has sufficient time to complete its internal process before the data is read allowing it to reach an accurate reading. Additionally, the project acknowledges that sensor aging and drift over time is a separate issue that affects long-term accuracy,

which future work aims to address by collecting empirical data to develop models that compensate for this drift.

Table 3.8 gathers the theoretical power consumption of the 2nd prototype sensor node. As before a single transmission cycle lasting 30 seconds is assumed. The average electric charge consumed for every device during each active cycle was determined using Equation (5). The theoretical average active current is calculated to be 63.2 mA using Equation (2). In sleep mode, only the wake-up timer, the 3.3 V DC/DC converter, and the main load switch remain partially active, yielding a combined sleep current of approximately 960 nA. Furthermore, using Equation (3), the total theoretical electric charge per reading is estimated to be about 528 µAh.

Table 3.8 – 2nd Prototype Sensor Node Theoretical Power Consumption

Description	Device	30 Second Read and Transmit Cycle					Sleep Time (s)	Typical Sleep Current
		Active Time (s)	Typical Active Current	Idle Time (s)	Typical Idle Current	Electric Charge (mAs)		
Peripheral Devices	ATSAMD21G18 [106]	30	5 mA	0	4 µA	150	0	OFF
	RFM95W [105]	1	29 mA	29	200 nA	29.006	0	OFF
	W25Q16JVSNIM [109]	2	20 mA	28	10 µA	40.28	0	OFF
	24AA025E64T [110]	0	3 mA	30	1 µA	0.03	0	OFF
	LTC2956 Timer [114]	30	800 nA	0	300 nA	0.024	3570	800 nA
Sensors	SPS30 [101]	8	60 mA	12	8 mA	576	0	OFF
	SCD30 [102]	20	19 mA	0	OFF	380	0	OFF
	SGP30 [103]	15	48 mA	0	OFF	720	0	OFF
	BME280 [104]	1	1.4 mA	29	100 nA	1.403	0	OFF
DC/DC Convertors	TPS62745 3.3V [112]	30	400 nA	0	130 nA	0.012	3570	130 nA
	LMZM23600 5V [113]	20	7 µA	0	OFF	0.14	0	OFF
	TPS62745 1.8V [112]	15	400 nA	5	130 nA	0.007	0	OFF
Switches	TPS27801A Battery [111]	1	30 nA	19	30 nA	0.001	0	OFF
	TPS27801A Main [111]	30	30 nA	0	30 nA	0.001	3570	30 nA

The introduction of a custom PCB layout enabled a notable improvement in standby power consumption and gave higher control over subsystem activation. However, it also highlighted unnecessary power wasted through always-active power domains, motivating additional fine-grained DPM refinements to reduce sleep-state current. This iteration served as a proving stage for improved efficiency while maintaining functional stability.

3.5 – 3rd Prototype Sensor Node

The 3rd prototype sensor node was re-designed with the target of bettering the SOA power consumption results achieved by the 2nd prototype sensor node. Specifically, by addressing the limited control over the 3.3 V devices which spend unnecessary time in idle mode. These devices, such as the RFM95W transceiver and the serial flash chip, can only be controlled via a single 3.3 V DC/DC converter on board the 2nd prototype node and hence end up being idle for most of the 30 second read and transmit cycle.

This 3rd iteration, therefore, introduced a highly fragmented DPM strategy. Figure 3.6 shows the improved and re-designed power management circuitry. First, to solve the sleep current issue, the LTC2956 timer was replaced with the TPL5111, an ultra-low-power timer chosen specifically for its minuscule 35 nA quiescent current, which is approximately 20 times lower than the LTC2956. Second, to solve the active-state inefficiency, the single 3.3V rail was broken apart. The 3.3 V DC/DC convertor now powers a series of TPS22860 load switches. These switches were chosen for their low on-resistance and, crucially, their ability to be controlled individually by the microcontroller. Each load switch is individually connected to a specific peripheral device or sensor. This fragmented approach allows each connected device to be individually powered on or off as required.

Powered also from the 3.3 V DC/DC convertor are a TCA9548 I2C switch and a PCF8575 GPIO expander. The I2C switch is used as a buffer to avoid conflicts on the I2C bus when hot-swapping I2C devices. The GPIO expander is used to control the load switches without using the GPIOs on the microcontroller. Another device which was added to this

design is the MAX5419 digital potentiometer. The digital potentiometer was added to digitally adjust the sleep time of this wake-up timer. Furthermore, this digital potentiometer can be switched off to further reduce power consumption. Despite the digital potentiometer being switched off, the sleep period of the wake-up timer can still be adjusted to pre-defined time intervals via switches on a resistor bank. The other devices which are connected directly to the main power source are the 1.8 V LDO, 5 V DC/DC convertor and the battery monitoring potential divider switch.

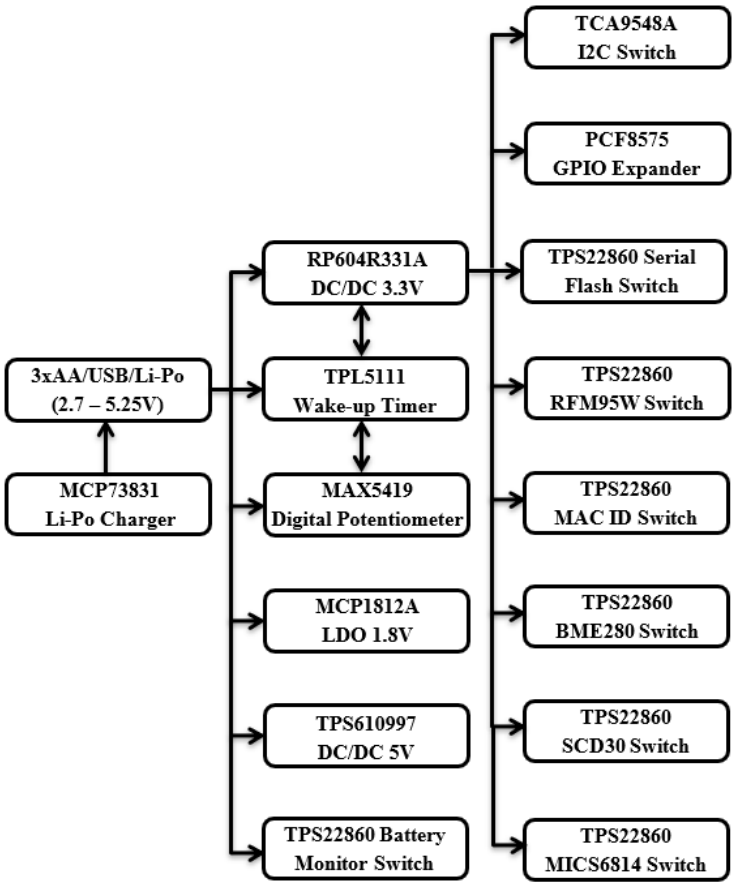

Figure 3.6 – 3rd prototype sensor node DPM circuitry

The specifications of the power management devices used are gathered in Table 3.9. This time more power efficient components are used when compared to the components used for the 2nd prototype sensor node. Using these components, the input voltage range

of the sensor node is shifted to 2.7 to 5.25 V from the previous 4 to 8 V. This allows 3 x AA, USB, or Li-Po power sources to be used to power up the device. For this reason, AA battery connectors, a micro-USB port and a JST connector for the Li-Po battery were built into the device. Moreover, a Li-Ion battery charger was also added to provide on-board Li-Ion charging. The Li-Po charger is powered via the micro-USB connector and can be activated using a switch.

Table 3.9 – 3rd prototype sensor node DPM devices

Device	Device Type	Input Voltage (V)	Output Voltage (V)	Output Current (mA)	Shutdown Current (nA)	Quiescent Current (nA)
TPS610997 [115]	DC/DC	0.7 – 5.5	5	800	500	1000
RP604K331 [116]	DC/DC	1.8 – 5.5	3.3	300	10	300
MCP1812A [117]	LDO	1.8 – 5.5	1.8	300	10	250
TPS22860 [118]	Switch	1.65 – 5.5	1.65 – 5.5	200	12	10
TPL5111 [119]	Timer	1.8 – 5.5	1.8 – 5.5	N/A	N/A	35
MAX5419 [120]	Potentiometer	2.7 – 5.25	N/A	N/A	N/A	500

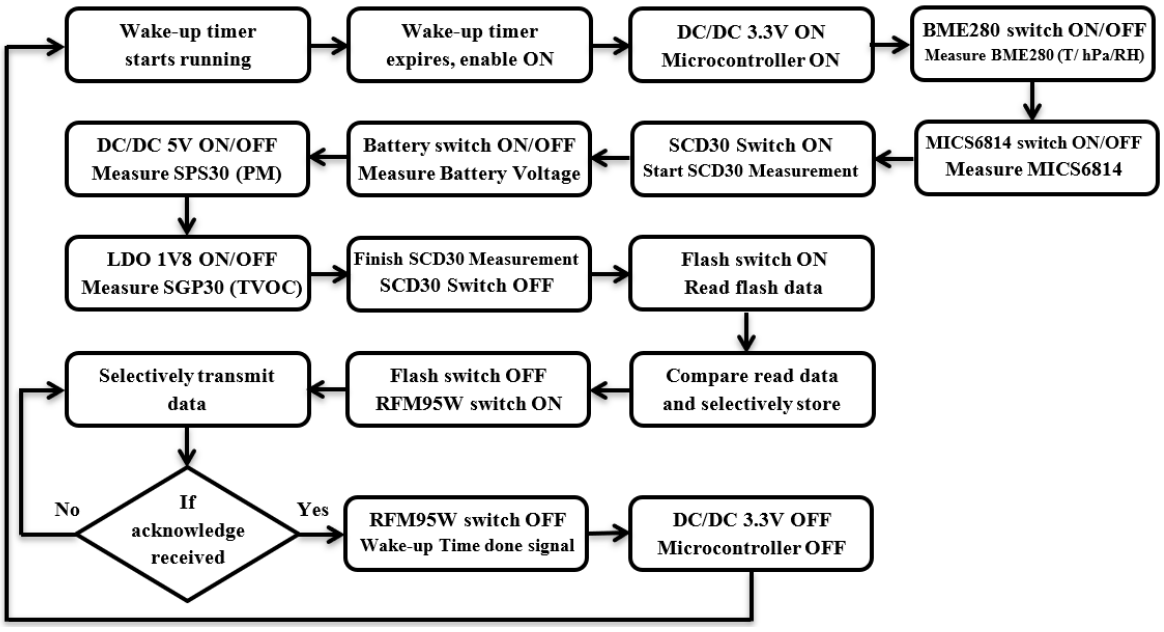

Figure 3.7 – 3rd prototype sensor node procedural code flowchart

Figure 3.7 shows the flowchart describing the C++ code written for this prototype. An expired wake-up timer enables the main 3.3 V DC/DC convertor which powers up the microcontroller and initialises the system. The load switch supplying power to the BME280 sensor is then temporarily switched on while the BME280 measurement is performed. A similar procedure follows to measure data from the MICS6814 sensor. The accuracy of this sensor is questionable, but it was still included in this design for testing purposes. Furthermore, during the power consumption measurements of this device this sensor was powered off. The load switch supplying power to the SCD30 sensor is then turned on and the SCD30 measurement is initialised.

During the SCD30 measurement the battery voltage, SGP30 and SPS30 measurements are taken. The load switch supplying power to the battery monitoring potential divider circuit is momentarily switched on until the battery voltage measurement is carried out. A similar procedure is used to measure the SPS30 and SGP30 sensors by momentarily powering the DC/DC convertor and 1.8 V LDO until the two measurements are finalised. An SCD30 measurement is then concluded and the switch supplying power to that sensor is turned off. The switch supplying power to the serial flash chip is then momentarily turned on to read stored data and selectively store the read data. The formatted data is then selectively transmitted over LoRa by momentarily powering the RFM95W transceiver through another load switch. Ensuing a successful radio broadcast, the wake-up timer is reset and the 3.3 V DC/DC convertor is switched off. This in turn switches off the microcontroller and sets the wake-up timer running once again.

Table 3.10 presents the theoretical power consumption for the 3rd prototype sensor node. As before, the analysis assumes one read and transmit cycle per hour, with each cycle lasting 30 seconds. The average electric charge consumed by each device during its active phase was calculated using Equation (5), and applying Equation (2) yields a theoretical average active current of 36.5 mA. In sleep mode, only the wake-up timer and the three DC/DC converters remain partially active, resulting in a combined sleep current of

approximately 567 nA. Moreover, using Equation (3), the total theoretical electric charge per reading is estimated to be around 305 µAh.

Table 3.10 – 3rd Prototype Sensor Node Theoretical Power Consumption

Description	Device	30 Second Read and Transmit Cycle					Sleep Time (s)	Typical Sleep Current
		Active Time (s)	Typical Active Current	Idle Time (s)	Typical Idle Current	Electric Charge (mAs)		
Peripheral Devices	ATSAMD21G18 [106]	30	5 mA	0	4 µA	150	0	OFF
	RFM95W [105]	1	29 mA	0	OFF	29	0	OFF
	W25Q16JVSNIM [109]	2	20 mA	0	OFF	40	0	OFF
	24AA025E64T [110]	0	3 mA	0	OFF	0	0	OFF
	TCA9548A [121]	20	5 µA	10	100 nA	0.101	0	OFF
	PCF8575 [122]	30	25 µA	0	2.5 µA	0.75	0	OFF
	MAX5419 [120]	0	OFF	0	OFF	0	0	OFF
	TPL5111 Timer [119]	30	35nA	0	35 nA	0.001	3570	35 nA
	MCP73831 Charger [123]	0	OFF	0	OFF	00	0	OFF
Sensors	SPS30 [101]	8	60 mA	0	OFF	480	0	OFF
	SCD30 [102]	20	19 mA	0	OFF	380	0	OFF
	SGP30 [103]	15	48 mA	0	OFF	720	0	OFF
	BME280 [104]	1	1.4 mA	0	OFF	1.4	0	OFF
	MICS6814 [124]	0	OFF	0	OFF	0	0	OFF
DC/DC Convertors	RP604R331A 3.3V [116]	30	300 nA	0	10 nA	0.009	3570	10 nA
	TPS610997 5V [115]	8	1 µA	22	500 nA	0.019	3570	500 nA
	MCP1812A 1.8V [117]	1	250 nA	29	10 nA	0.001	3599	10 nA
Switches	TPS22860 Flash [118]	2	10 nA	28	12 nA	0	0	OFF
	TPS22860 Radio [118]	1	10 nA	29	12 nA	0	0	OFF
	TPS22860 MAC ID [118]	0	10 nA	30	12 nA	0	0	OFF
	TPS22860 BME280 [118]	1	10 nA	29	12 nA	0	0	OFF
	TPS22860 SCD30 [118]	20	10 nA	10	12 nA	0	0	OFF
	TPS22860 MICS6814 [118]	0	10 nA	30	12 nA	0	0	OFF
	TPS22860 Battery [118]	1	10 nA	29	12 nA	0	3599	12 nA

This 3rd prototype incorporated enhanced component-level switching, enabling stronger reductions in active-mode overheads and improving battery longevity. These design advancements continued to move the system closer to the required performance targets.

3.6 – 4th Prototype Sensor Node

The 4th and final prototype sensor node was developed to build upon the successful ultra-low power DPM strategy of the 3rd prototype, while also directly addressing a key project objective: modularity and expandability. While Prototype 3 was power-efficient, its monolithic PCB was inflexible. This final iteration adopted a modular, two-board stackable design. It consists of two stackable boards: one dedicated to power management and the microcontroller, and another serving as a shield that houses the air quality sensors and LoRa transceiver. This modular configuration simplifies future upgrades of the sensor node and enhances flexibility. By simply swapping the shield, the power management and microcontroller board can be easily adapted for use in a variety of other WSN applications.

Figure 3.8 shows the DPM circuity of the 4th prototype, which was further refined to reduce power consumption. While most power management components from the 3rd prototype were retained, a final DPM optimisation was made by replacing the 1.8 V LDO with a TPS62746 1.8 V DC/DC converter. This choice was made as this DC/DC convertor offers significantly higher power efficiency. This iteration also advances DPM strategy used previously by fragmenting it further. As shown in Figure 3.8, the DPM is now fully hierarchical. The TPL5111 wake-up timer no longer triggers the 3.3V DC/DC converter directly but instead it triggers a main TPS22860 load switch which in turn powers the 3.3V converter. This extra layer of control isolates the 3.3V converter completely from the battery during sleep, eliminating its 10 nA shutdown current and leaving only the timer and the load switch drawing power.

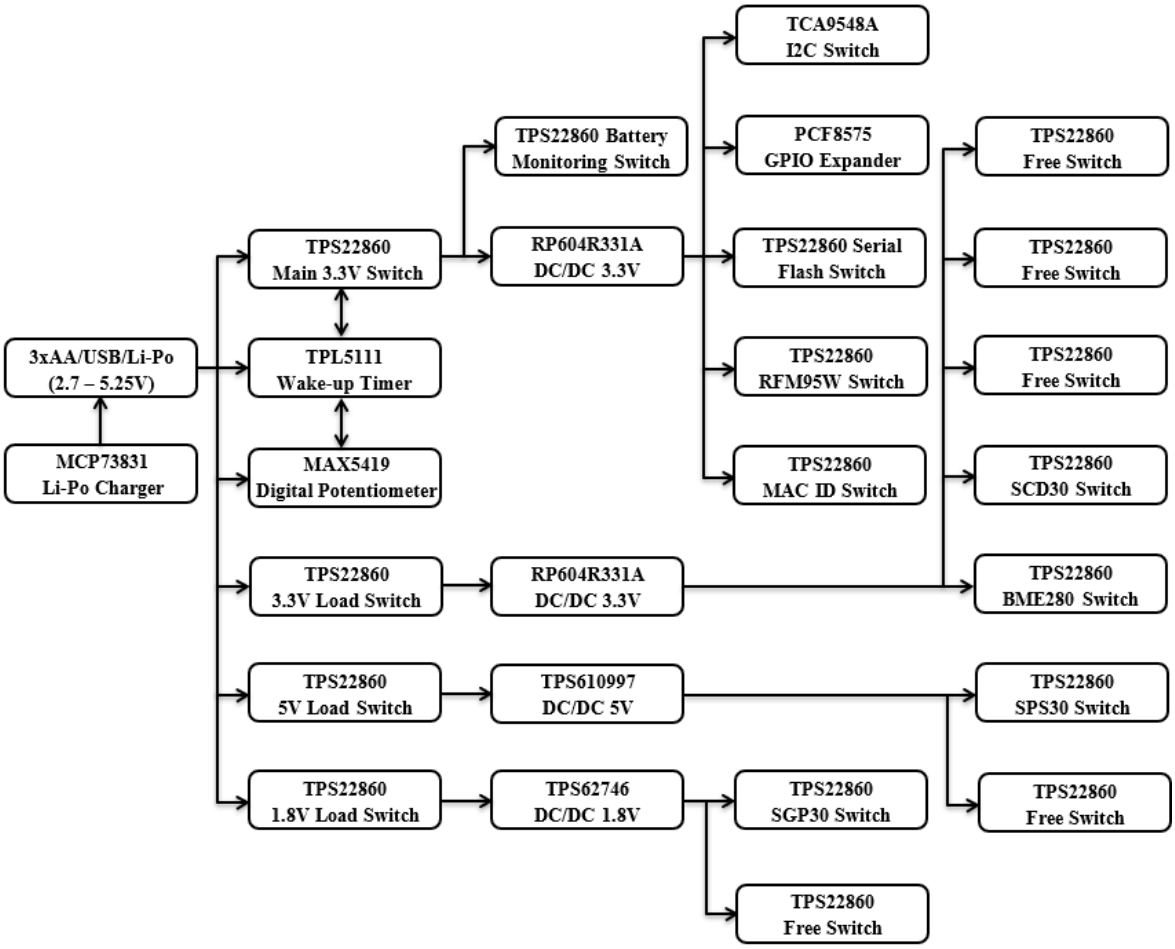

Figure 3.8 – 4th prototype sensor node DPM circuitry

Additionally, the battery monitoring circuit is similarly powered via this main load switch, further isolating it from the supply during inactive periods. The main 3.3 V converter supplies power to the microcontroller, an I2C switch, a GPIO expander, and other load switches that independently manage power to the flash memory, LoRa transceivers, and the MAC ID chip. Furthermore, three other load switches draw power directly from the input source to activate separate DC/DC converters. Each of these converters is linked to at least two load switches that independently power specific sensors. Several unused load switches, marked as free, were also incorporated to facilitate power control for potential future sensors and devices. Moreover, while previous designs relied on a single 3.3 V converter, this version includes two such convertors. This dual-converter

setup distributes the load, making it easier to accommodate future expansions without overloading individual power components.

The flowchart defining the purposely written C++ code is shown in Figure 3.9. This flowchart is very similar to the flowchart used to describe the program for the 3rd prototype sensor node. The main difference is the greater amount of load switches which need to be controlled. Furthermore, the MICS6814 sensor, was omitted from this design due to the low accuracy of this sensor. This sensor was added as a test in the previous prototype as an attempt to further enhance the measuring capabilities of the sensor node even though measuring carbon monoxide was not part of the original specifications. Additionally, other attempts to find more accurate sensor which is able to accurately measure carbon monoxide at a low-cost price point proved to be challenging.

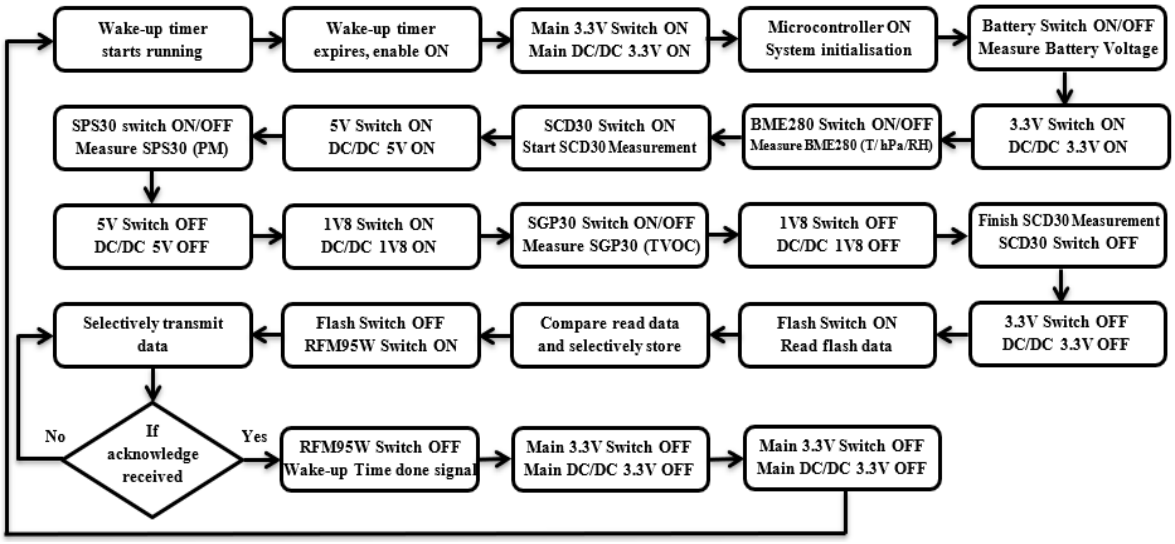

Figure 3.9 – 4th prototype sensor node procedural code flowchart

Table 3.11 outlines the theoretical power consumption for the 4th prototype sensor node. As previously, the analysis assumes one read and transmit cycle per hour, each lasting 30 seconds. The average electric charge drawn by each device during its active phase was computed using Equation (5), and applying Equation (2) gives a theoretical average active current of 36.5 mA. In sleep mode, only the wake-up timer and the four load switches

powering the DC/DC converters remain partially active, resulting in a combined sleep current of roughly 83 nA. Additionally, using Equation (3), the total theoretical electric charge per reading is estimated at approximately 304 µAh.

Table 3.11 – 4th Prototype Sensor Node Theoretical Power Consumption

Description	Device	30 Second Read and Transmit Cycle					Sleep Time (s)	Typical Sleep Current
		Active Time (s)	Typical Active Current	Idle Time (s)	Typical Idle Current	Electric Charge (mAs)		
Peripheral Devices	ATSAMD21G18 [106]	30	5 mA	0	4 µA	150	0	OFF
	RFM95W [105]	1	29 mA	0	OFF	29	0	OFF
	W25Q16JVSNIM [109]	2	20 mA	0	OFF	40	0	OFF
	24AA025E64T [110]	0	3 mA	0	OFF	0	0	OFF
	TCA9548A [121]	20	5 µA	10	100 nA	0.101	0	OFF
	PCF8575 [122]	30	25 µA	0	2.5 µA	0.75	0	OFF
	MAX5419 [120]	0	OFF	0	OFF	0	0	OFF
	TPL5111 Timer [119]	30	35nA	0	35 nA	0.001	3570	35 nA
	MCP73831 Charger [123]	0	OFF	0	OFF	0	0	OFF
Sensors	SPS30 [101]	8	60 mA	0	OFF	480	0	OFF
	SCD30 [102]	20	19 mA	0	OFF	380	0	OFF
	SGP30 [103]	15	48 mA	0	OFF	720	0	OFF
	BME280 [104]	1	1.4 mA	0	OFF	1.4	0	OFF
DC/DC Convertors	RP604R331A 3.3V Main [116]	30	300 nA	0	10 nA	0.009	0	OFF
	RP604R331A 3.3V 2nd [116]	20	300 nA	0	10 nA	0.006	0	OFF
	TPS610997 5V [115]	8	1 µA	0	500 nA	0.008	0	OFF
	TPS62746 1.8V [125]	15	360 nA	0	70 nA	0.005	0	OFF
Main Switches	TPS22860 3.3V Main [118]	30	10 nA	0	12 nA	0	3570	12 nA
	TPS22860 3.3V 2nd [118]	20	10 nA	10	12 nA	0	3570	12 nA
	TPS22860 5V [118]	8	10 nA	22	12 nA	0	3570	12 nA
	TPS22860 1.8V [118]	15	10 nA	15	12 nA	0	3570	12 nA
Secondary Switches	TPS22860 Battery [118]	1	10 nA	29	12 nA	0	0	OFF
	TPS22860 Flash [118]	2	10 nA	28	12 nA	0	0	OFF
	TPS22860 Radio [118]	1	10 nA	29	12 nA	0	0	OFF
	TPS22860 MAC ID [118]	0	10 nA	30	12 nA	0	0	OFF
	TPS22860 3.3V Free x3 [118]	0	30 nA	20	36 nA	0	0	OFF
	TPS22860 BME280 [118]	1	10 nA	19	12 nA	0	0	OFF
	TPS22860 SCD30 [118]	20	10 nA	0	12 nA	0	0	OFF
	TPS22860 SPS30 [118]	8	10 nA	0	12 nA	0	0	OFF
	TPS22860 5V Free [118]	0	10 nA	8	12 nA	0	0	OFF
	TPS22860 SGP30 [118]	15	10 nA	0	12 nA	0	0	OFF
	TPS22860 1.8V Free [118]	0	10 nA	15	12 nA	0	0	OFF

The 4th prototype sensor node featured a modular, stackable design with separate boards for power management/microcontroller and the sensor shield. The DPM was refined

from the 3rd prototype by replacing the 1.8V LDO with a more efficient DC/DC converter and adding hierarchical load switches to completely power down components, including the converters themselves, during sleep. Additionally, this node theoretically achieved the lowest power consumption out of all the proposed prototypes.

Chapter 4 – LoRa-based Big Data Capture and Analysis System

4.1 – Introduction

The research and development performed on the proposed low-cost LoRa-based big data capture and analysis system is discussed in this section. First, the LoRa network architecture is presented. This is followed by the work carried out on the IoT messaging and data forwarding server along with the big data capture and analysis tools. Finally, a LoRa scalability and theoretical propagation simulation model within an enclosed building is presented.

4.2 – LoRa Network Architecture

The core component of any IoT system is its wireless communication protocol, which is typically chosen based on specific design constraints and application needs, as outlined in Section 2.2. In this study, LoRa an LPWAN protocol, was selected as the most suitable option due to its high link budget and low power consumption. Although LPWAN protocols like LoRa offer lower data rates compared to IEEE 802.11 and IEEE 802.15 standards, they significantly outperform them in terms of communication range and energy efficiency. Nonetheless, the maximum data rate of 50 Kbps achievable by LoRa is sufficient for IAQ monitoring applications. Additionally, LoRa allows for optimisation of system performance by adjusting parameters such as bandwidth and SF, enabling a tailored trade-off between data rate, coverage, and energy usage [54, 55].

After determining that LoRa is the most appropriate choice for this air quality monitoring application, the big data capture and analysis system was designed based on a LoRa WSN architecture. The WSN adopts a star topology, where multiple sensor nodes communicate directly via LoRa with one or more gateways strategically placed around the Faculty of ICT. These gateways then transmit the collected data to a central router using either Wi-Fi or Ethernet. From there, the router relays the data to either a local server or a

cloud-based platform. A range of tools will be employed to collect, visualise, and analyse the data. This approach also enhances accessibility, allowing data to be viewed remotely from personal computers, smartphones, or tablets via Wi-Fi or 3G/4G connectivity.

The chosen star network topology fundamentally impacts the scalability and robustness the WSN. This structure connects all sensor nodes directly to a central gateway. A key advantage of this design is its energy efficiency. The lowest power consumption is achieved out of all topologies because sensor nodes do not need to constantly listen for messages or participate in multi-hop routing, unlike in mesh networks. In terms of scalability, the star topology is well-suited for adding numerous sensor nodes. However, the central gateway can eventually become a bottleneck, potentially increasing packet collisions and reducing throughput as node density increases beyond the theoretical maximum [47, 48].

Additionally, the star topology inherently suffers from low robustness, as the entire network collapses if the single central gateway fails due to a lack of alternative communication paths. The superior alternative in terms of reliability is the mesh topology, where nodes connect to each other to create multiple routing paths, offering high fault tolerance and enabling network data to be rerouted around failed nodes. This robustness, however, comes at the cost of the highest power consumption as nodes must engage in power hungry routing and listening activities. A hybrid approach attempts to leverage the best of both by combining the mesh robustness with the star efficiency, creating a scalable and resilient middle ground. Since the main objective of this work is achieving an extended battery life, the star topology was still chosen despite the aforementioned disadvantages. To mitigate some of these disadvantages multiple gateways will be deployed across the large scale network such that robustness and scalability are ensured [47, 48, 49, 50].

Two approaches to the big data capture and analysis system are proposed: a local-based approach and a cloud-based approach. A diagram for each of these two approaches is depicted in Figure 4.1 and Figure 4.2. The local-based approach processes all collected

data through an on-site LoRaWAN data forwarding server, ensuring complete control and privacy by eliminating the involvement of third parties in handling the data. In contrast, the cloud-based approach relies on various cloud services for data processing, transmission, storage, and analysis. This results in a system that is more straightforward to maintain and upgrade while also providing more convenient access to the data from remote locations.

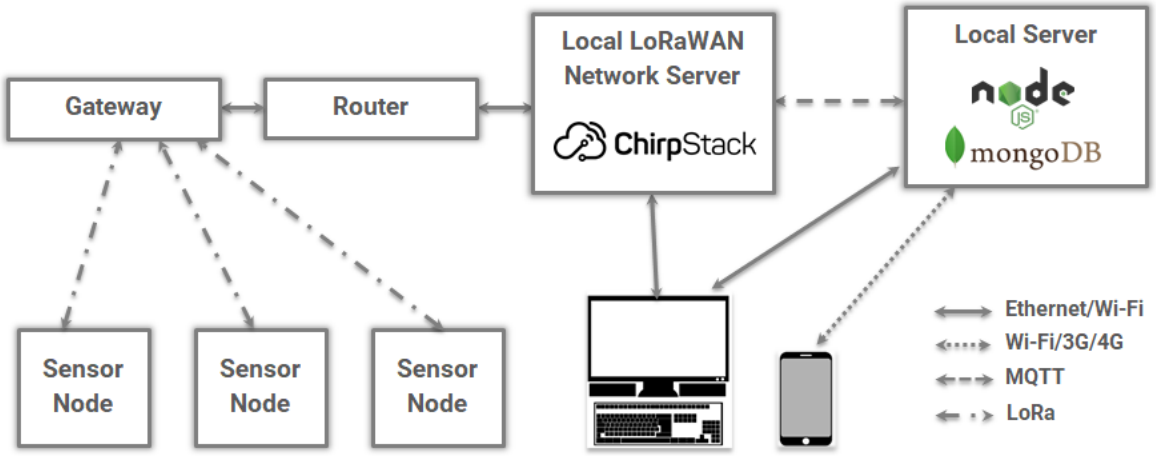

Figure 4.1 – Local-based big data capture and analysis solution

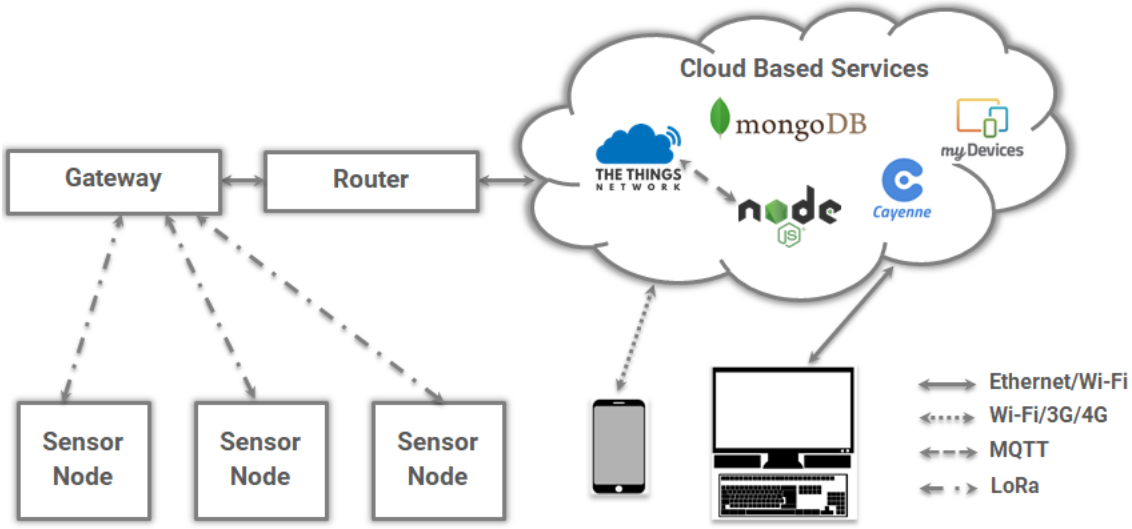

Figure 4.2 – Cloud-based big data capture and analysis solution

The basic building block of the two solutions being proposed is the actual sensor node. The LoRa transceiver embedded within the sensor node is crucially important as it has an impact on both the available radio link budget as well as the global cost of the system. A number of low-cost LoRa transceiver modules are therefore presented in Table 4.1. Most of these transceivers are built on the Semtech SX1276 chipset transceiver and have similar specifications. The RFM95W was selected as being most suitable due to it being both low-cost and low-power. Not only is this LoRa transceiver the cheapest available on the market but it also has the highest receiver sensitivity.

Table 4.1 – Low-cost LoRa transceivers

Transceiver Module	**Tx Power (dBm)**	**Rx Sensitivity (dBm)**	**Current**			**Cost**
			Tx (mA)	***Rx (mA)***	***Sleep (µA)***	
CMWX1ZZABZ	14	-135.5	47	23.6	1.4	€ 15
iM88A-XL	10/13/15	-138	25/29/38	11.2	1.4	€ 12
RAK811	14	-130	30	5.5	7.2	€ 10
RN2483	14	-148	28/39	14.2	2	€ 8
RFM95W	7/13/17/20	-148	20/29/87/120	10.3	0.2	€ 6

Table 4.2 – Low-cost LoRa gateways

Gateway	**Ethernet/Wi-Fi/ LTE/GPS**	**Rx Channels**	**Rx Sensitivity (dBm)**	**Cost**
TTN Gateway	Yes/Yes/No/Yes	8	N/A	€ 280
WLRGFM-100	Yes/Yes/No/No	8	-142	€ 180
RAK831 & Raspberry Pi	Yes/Yes/No/Yes	8	-142	€ 175
RAK7258	Yes/Yes/No/No	8	-142	€ 140
LG02	Yes/Yes/No/No	2	-148	€ 80
TTN Indoor	No/Yes/No/No	8	-140	€ 65
LG01-S	Yes/Yes/No/No	1	-148	€ 50

Similarly, Table 4.2 presents several affordable LoRa gateways most of which utilise the Semtech SX1301 baseband processor in combination with the SX1257 transceiver chipset, enabling support for eight simultaneous reception channels. The RAK7258 was deemed the most suitable due to its cost-effectiveness and its inclusion of both Ethernet

and Wi-Fi connectivity. Additionally, the OpenWRT firmware allows for real-time monitoring of key LoRa parameters such as duty cycle, data traffic, RSSI, and SNR.

After selecting the gateway and transceiver, the LoRaWAN network server was chosen following the same cost-effective approach. While several commercial providers such as Loriot and Senet offer proprietary network server solutions, free open-source options are limited to primarily two platforms: The Things Network and ChirpStack. Their specifications are outlined in Table 4.3. Both platforms support the deployment of unlimited gateways and IoT nodes with the key distinction lying in their network structure. The Things Network operates as a public network, whereas ChirpStack is a private solution. As a result, ChirpStack is more suitable for local-based implementations, while The Things Network is better aligned with cloud-based architectures.

Table 4.3 – Free LoRaWAN servers with an open-source architecture

LoRaWAN Server	Open Source	Network Type	Maximum Number of Gateways/Devices	API Support
The Things Network	Yes	Public	Unlimited/Unlimited	Yes
Chirp Stack	Yes	Private	Unlimited/Unlimited	Yes

After selecting the core components of the LoRa network architecture, a series of tests were conducted to validate the system's functionality. Two RAK7258 gateways were configured, one registered with the ChirpStack server and the other with The Things Network. Wireless sensor nodes equipped with the RFM95W LoRa transceiver were also registered on these open-source LoRaWAN platforms. Devices were added to the network using two available authentication methods: Over-the-Air Activation (OTAA) and Activation by Personalisation (ABP). OTAA offers enhanced security, as it involves dynamic assignment of the device address and secure key exchange during the join process. However, this method leads to greater power consumption in the sensor nodes. In contrast, ABP is faster and more power-efficient but provides a lower level of security.

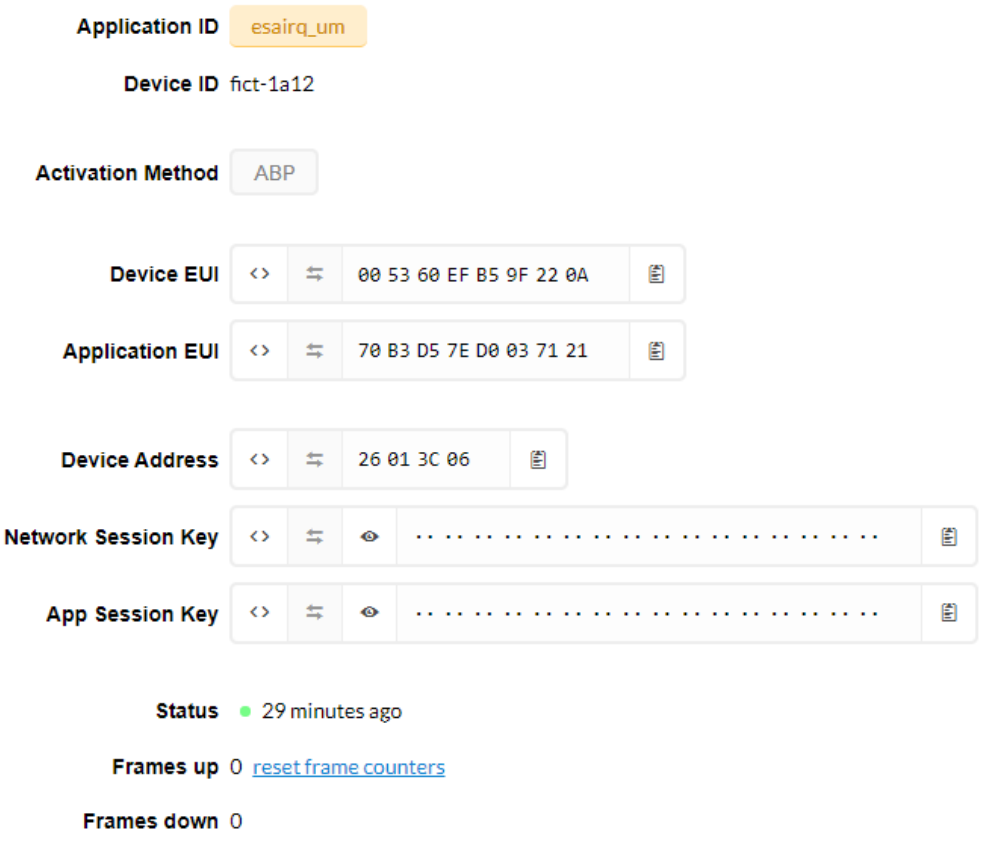

Figure 4.3 – Device registered on The Things Network using ABP

Since this implementation is focused on low power design, ABP was preferred to OTAA even though ABP is less secure than OTAA. Figure 4.3 shows one of the wireless sensor nodes which is registered using ABP on The Things Network LoRaWAN server. The device extended unique identifier (EUI) and device address fields are unique fields used for device identification on the LoRaWAN network whilst the network session and app session keys are pre-agreed and used for device authentication. The application EUI field is used to identify the LoRaWAN application that the wireless sensor node is registered to. Other fields such as the status and frames up fields are used to keep track of the device.

The individual packets being transmitted by the sensor node can be monitored using two tools either the LoRaWAN server or else the OpenWRT software on the LoRa gateway. Figure 4.4 shows a LoRa packet being captured by The Things Network. Apart from the raw

payload being displayed, the decoded payload as well as decode metadata are also generated. The Cayenne LPP integration is being used to decode the Cayenne LPP encoded messages from the sensor nodes. This protocol follows the internet protocol for smart objects (IPSO) guidelines. Similarly, Figure 4.5 shows a packet being captured by OpenWRT. Once again, the raw payload as well as the metadata are being captured. LoRa metadata fields include parameters such as the bandwidth, SF, coding rate and frequency. Other fields showing the channel conditions such as RSSI, SNR and airtime are also generated.

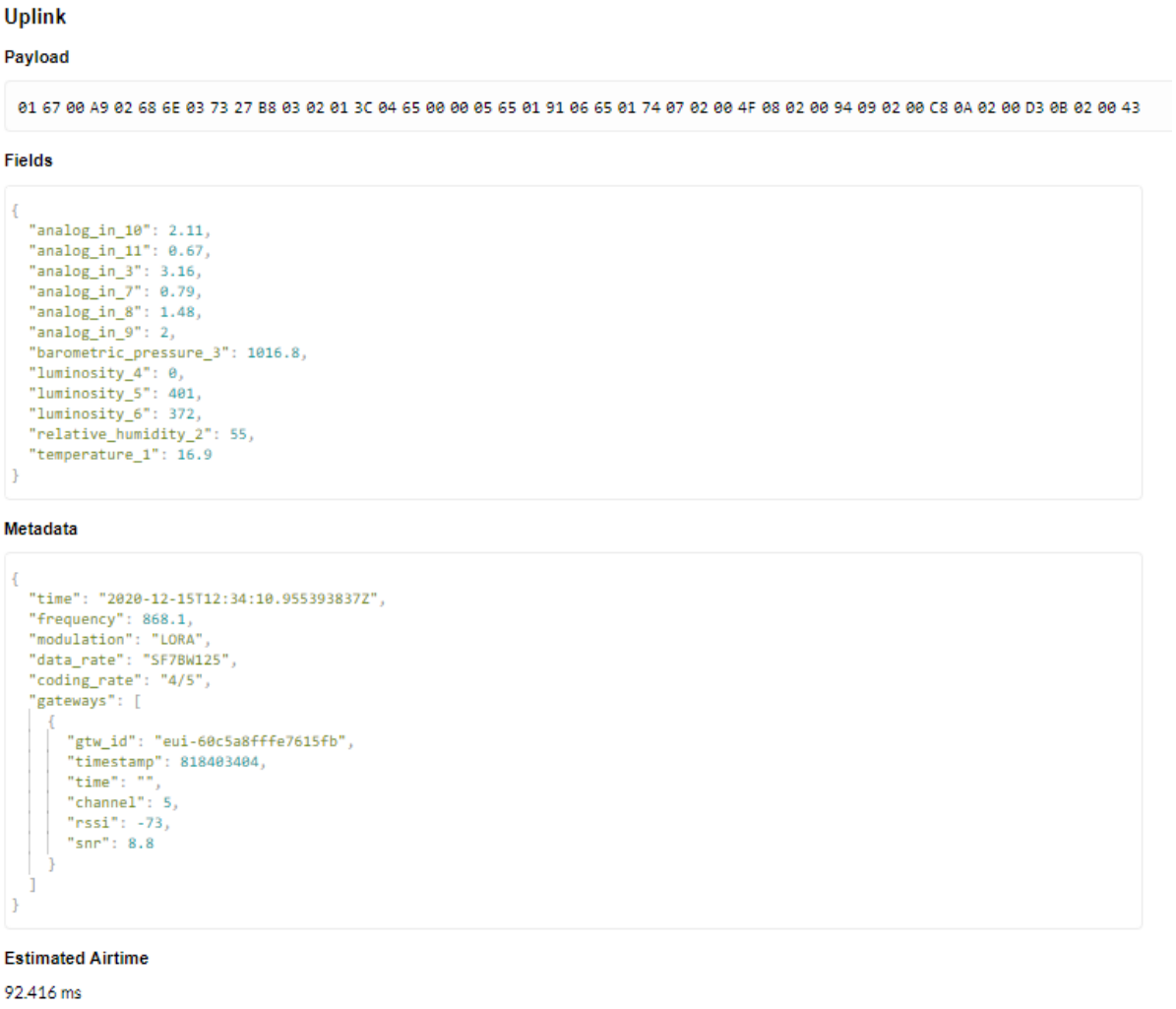

Figure 4.4 – LoRa packet captured on The Things Network

Time	Freq.	RSSI	SNR	TxPwr	CRC	mod.	CR	DataRate	FCnt	AirTime	DevAddr	FPort	Payload Size
13:23:01	867.7	-67	10.5	-	CRC_OK	LORA	4/5	SF7BW125	0	108	26011EAE	1	47


```
{
    "freq": 867700000,
    "chan": 3,
    "tmst": 146634747,
    "utmms": 1608034979155,
    "rfch": 0,
    "stat": 1,
    "rssi": -67,
    "size": 60,
    "modu": "LORA",
    "datr": "SF7BW125",
    "codr": "4/5",
    "lsnr": 10.5,
    "data": "QK4eASaAAAABc6PmdrglCZndDe4ISpToENhDaqcOdy/pTNkQHGB36Tzrb8pTCK6lzeHg5z2+CFC+d6SQ"
}
{
    "MHDR": {
        "MType": "Unconfirmed Data Up",
        "RFU": 0,
        "Major": 0
    },
    "MACPayload": {
        "FHDR": {
            "DevAddr": "26011EAE",
            "FCtrl": {
                "ADR": true,
                "ADRACKReq": false,
                "ClassB": false,
                "ACK": false,
                "FOptsLen": 0
            },
            "FCnt": 0
        },
        "FPort": 1,
        "FRMPayload": "01 73 A3 E6 76 B8 25 09 99 DD 0D EE 08 4A 94 E8 10 D8 43 6A A7 0E 77 2F E9 4C D9 10
1C 60 77 E9 3C EB 6F CA 53 08 AE A5 CD E1 E0 E7 3D BE 08 "
    },
    "MIC": "BE77A490"
}
```


Figure 4.5 – LoRa packet captured using OpenWRT software

The OpenWRT software was also used to generate several metadata visualisations used for LoRa network performance measurement and analysis. Figure 4.6 shows the values of SNR and RSSI of the different LoRa packets being received over the network. This can be used to ensure that the optimal LoRa propagation is achieved throughout the deployment environment.

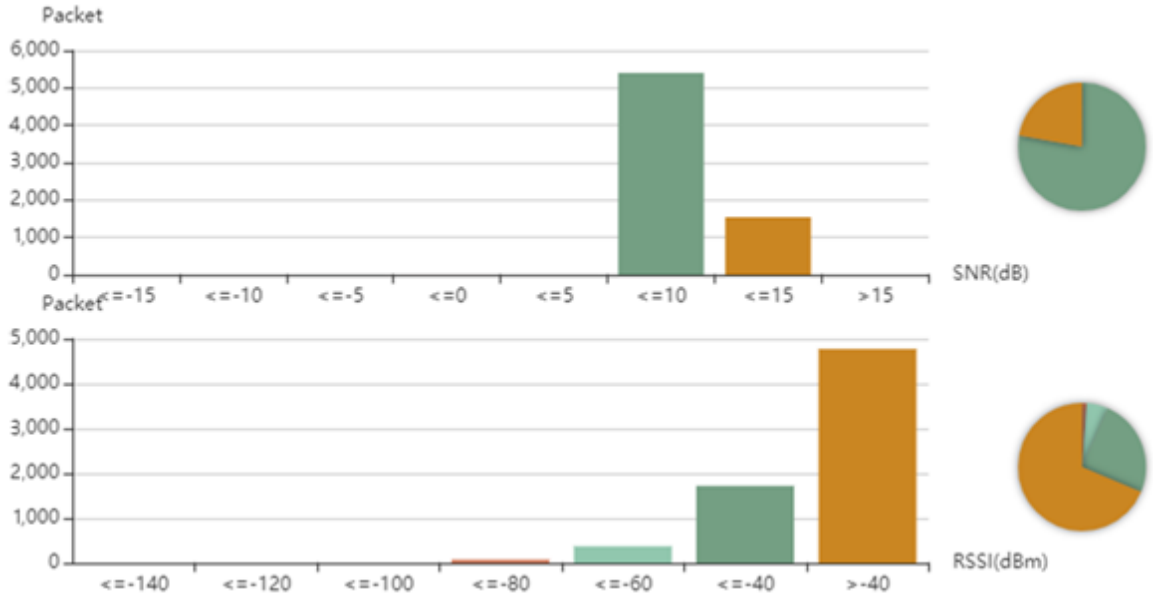

Figure 4.6 – LoRa packets RSSI and SNR

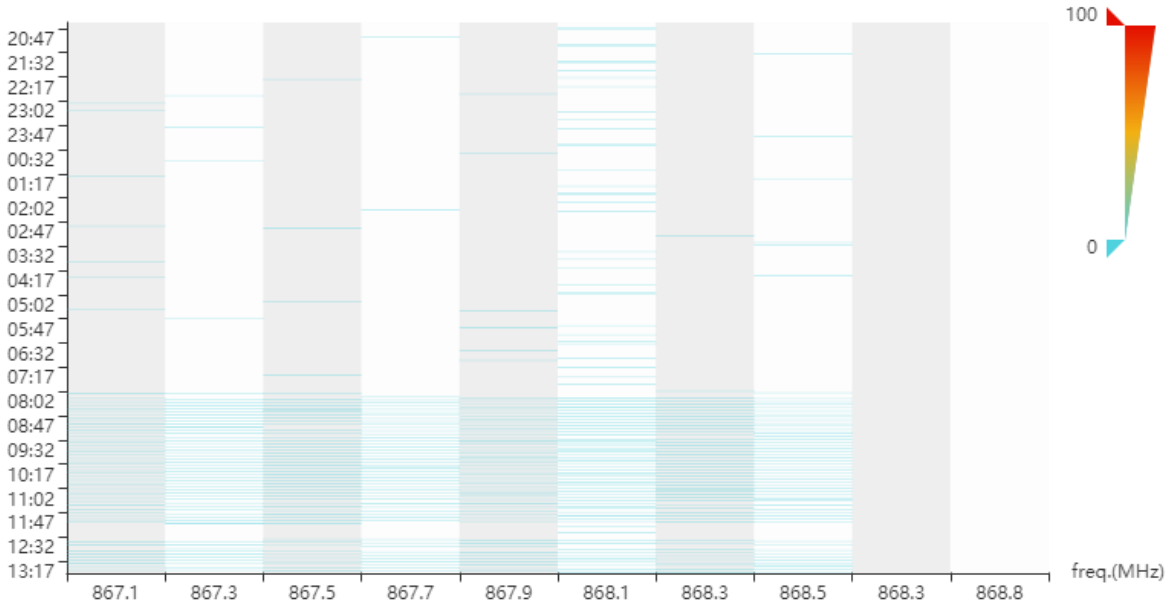

Figure 4.7 – LoRa channel duty cycle

Additionally, Figure 4.7 shows the LoRa channel duty cycle graph. This graph is vital to ensure that no device is exceeding 1% duty cycle which in Europe is enforceable on the 868 MHz ISM band. Figure 4.8 shows the uplink traffic data rate graph. This graph is useful

as it shows the number of packets being received by the gateway as well as the airtime of these packets. Additionally, the gaps were the values in the graph are equivalent to zero show us that no packets are being transmitted at that particular point in time.

Figure 4.8 – LoRa uplink traffic data rate

4.3 – LoRa Scalability and Theoretical Propagation Simulation Model

This section presents an integrated modelling and simulation framework which was developed for LoRa indoor wireless sensor networks. Equations for RSSI, SNR, and collision probability are derived to assess link quality and overall network performance under stringent European duty cycle constraints in the 868 MHz ISM band. Simulation results demonstrate how wall attenuation, multipath effects, and increased node density affect network scalability and reliability.

4.3.1 – Simulation Setup

The simulation framework is developed in MATLAB to emulate an office building constructed of concrete and fully enclosed by glass. The Faculty of ICT building shown in

Figure 4.9 was identified as a testbed. The structure is made up of two shifted 40 m x 40 m blocks interconnected via a 5m x 20m central corridor and spanning over four floors. Furthermore, the building has a concrete substructure with a steel framed upper structure which is fully walled by glass.

Figure 4.9 – Faculty of ICT building used as WSN testbed

The simulated indoor air quality monitoring sensor nodes are fitted with RFM95W LoRa transceivers. These sensor nodes and are randomly distributed throughout the building. Similarly, a single RAK7258 LoRa gateway is simulated and strategically located at the centre to maximise coverage and service these sensor nodes. The sensor nodes periodically transmit data and contend with multipath propagation, wall attenuation, and interference from simultaneous transmissions. Additionally, the network must adhere to European duty cycle regulations, which limit both transmission duration and power levels.

Figure 4.10 shows the simulated position of randomly distributed sensor nodes on each floor of the two blocks within the building. Furthermore, the simulated centrally located gateway in the connecting corridor on Level 0 is also shown. In addition, Figure 4.11 shows the distances between the simulated sensor nodes across all floors to the gateway. These distances range from a few meters for the closest sensor nodes up to 50 m for the furthest sensor nodes on Level -2, with the average overall distance across all four levels being equivalent to 23 m.

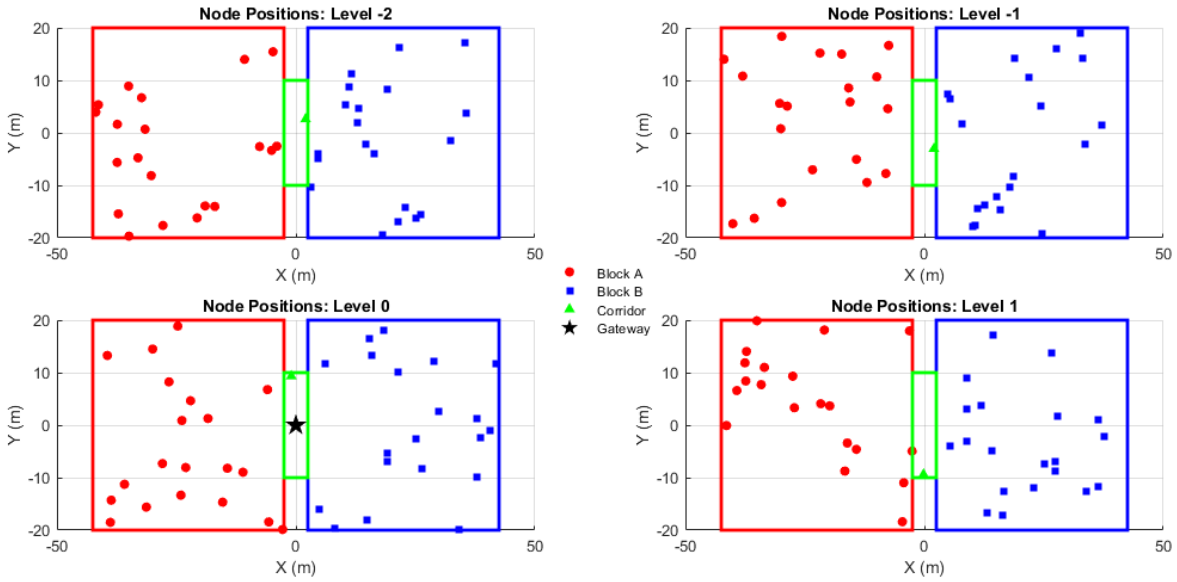

Figure 4.10 – Simulated randomly distributed sensor nodes inside the building

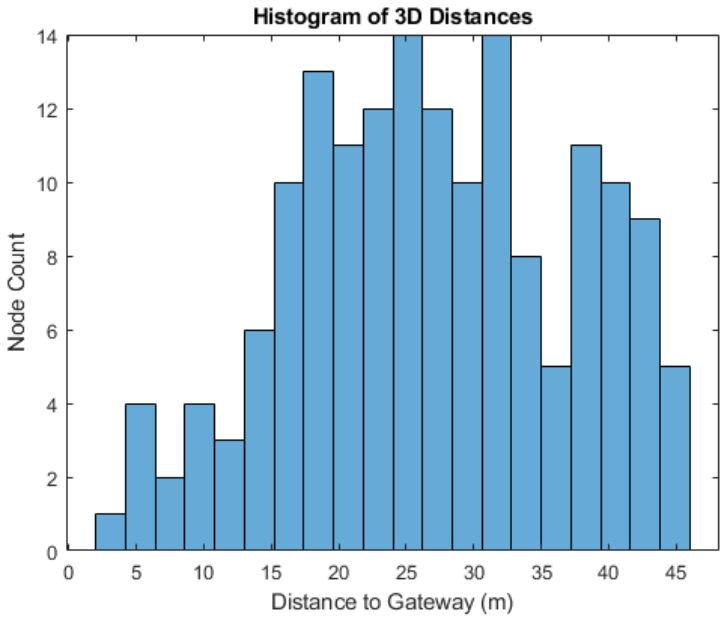

Figure 4.11 – Histogram of sensor node distance to the simulated gateway

4.3.2 – Propagation Models

As mentioned previously in Chapter 2, LoRa WSNs are increasingly deployed in indoor environments such as multi-storey office buildings. Signal propagation in these

environments is heavily influenced by concrete walls, glass facades, and inter-floor obstructions. Four different propagation models, namely the COST-231 Multi-Wall model, the Log-Distance Path Loss model, the ITU-R P.1238 model and the 3GPP Indoor Hotspot model, are proposed to be used in this simulation framework. These four propagation models are employed to capture the complex indoor radio effects of the proposed indoor wireless sensor network deployment [126, 127].

Additionally, other indoor propagation models such as the work in [128] propose slight variations to the selected propagation models. In [128], a variation of the multi-wall model is proposed. This modified model incorporates the use of polarisation and angle of incidence of the beam by automatically detecting walls and their orientation from a blueprint. This work claims an improved accuracy of 0.5 dB per measurement location. However, given this fractional increase in accuracy, the original multi-wall model was still utilised for this framework.

A – COST-231 Multi-Wall Model

Indoor propagation in environments with significant obstacles can be effectively captured by the COST-231 Multi-wall Model. The path loss $PL(d)$ at a distance d is given by Equation (6).

$$PL(d) = PL(d_0) + 10\, n \log_{10}\left(\frac{d}{d_0}\right) + \sum_{i=1}^{N_w} L_{w,i} \qquad (6)$$

In this Equation, $PL(d_0)$ is the baseline path loss at a reference distance d_0. Considering that $d_0$is typically taken as being equivalent to 1 m the reference path loss can be worked out using Equation (7). Furthermore, considering European regulations, the operation frequency of LoRa is 868 MHz and therefore λ can be worked out using Equation (8) to be approximately equivalent to 0.345m [129, 130].

$$PL(d_0) = 20\log_{10}\left(\frac{4\pi d_0}{\lambda}\right) \qquad (7)$$

$$\lambda = \frac{c}{f} \approx \frac{3 \times 10^8 \text{ m/s}}{868 \times 10^6 \text{ Hz}} \approx 0.345 \text{ m} \qquad (8)$$

Additionally, in Equation (6), n is the path loss exponent which captures the rate of increase of the path loss with distance. This value typically ranges between 2 to 4 for indoor environments. Furthermore, N_w is the number of walls or partitions between the receiver and the transmitter whilst $L_{w,i}$ represents the attenuation due to the i^{th} wall. For example, if a concrete wall is considered, this value generally ranges from 5 to 10 dB [129, 130].

B – Log-Distance Path Loss Model

Another model utilised for indoor LoRa propagation modelling is the Log-Distance Path Loss model. This model accounts for large-scale fading and shadowing via a stochastic term and is given by Equation (9) [126, 131].

$$PL(d) = PL(d_0) + 10\,n\log_{10}\left(\frac{d}{d_0}\right) + X_\sigma \qquad (9)$$

Similar to the COST-231 multiwall model, $PL(d_0)$ is the path loss at the reference distance d_0 and n is the path loss exponent. X_σ is a zero-mean Gaussian random variable with standard deviation σ representing shadow fading. Typical values for σ range from 4 to 8 dB in indoor environments [126, 131].

C – ITU-R P.1238 Model

The ITU-R P.1238 is another indoor propagation model which can be adapted to simulate indoor LoRa propagation. The formulation for this model is given below in Equation (10) [132].

$$PL(d) = 20\ \log_{10}(f) + N\ \log_{10}(d) + L_f(n) - 28 \qquad (10)$$

In this Equation, f is the frequency, in this case 868 MHz, and d is the distance between the receiver and the transmitter. Additionally, N is the path loss exponent factor, with typical values for indoor concrete environments ranging from 35 to 40. Finally, $L_f(n)$ represents the floor penetration loss factor whilst -28 is a constant derived from the free-space path loss expression and used to normalise the equation [132].

D – 3GPP Indoor Hotspot Model

The final model which will be utilised in this framework to model indoor LoRa propagation is the 3GPP Indoor Hotspot propagation model. The non-line of sight variant of this model is given by Equation (11) [133].

$$PL(d) = 36.7 \log_{10}(d) + 22.7 + 26 \log_{10}(f) \qquad (11)$$

Similarly to the previous model f is the frequency and d is the distance between the receiver and the transmitter. Furthermore, this model is only valid over distances of around 4 to 50 m [133].

4.3.3 – Link Quality Metrics

In order to evaluate the quality of the radio link in dense indoor environments, two metrics are derived namely the RSSI and SNR. The received power RSSI in dBm at the gateway can be computed using the standard link budget Equation (12). In this Equation, $P_{transmit}$ is the transmit power in dBm, $G_{transmitter}$ and $G_{receiver}$ are the transmitter and receiver antenna gains in dBi, and $PL(d)$ is the path loss computed from the propagation models describe previously using Equation (6),(9), (10) or (11) [131, 134, 135].

$$RSSI = P_{transmit} + G_{transmitter} + G_{receiver} - PL(d) \qquad (12)$$

Additionally, the SNR at the receiver quantifies the quality of the link. The SNR is determined by the difference between the RSSI and the noise floor and is therefore given

by Equation (13). The noise floor N_0 in dBm can be estimated as shown in Equation (14). In this Equation, BW is the receiver bandwidth in Hz, and NF is the receiver noise figure in dB [131, 134, 135].

$$\text{SNR} = \text{RSSI} - N_0 \qquad (13)$$

$$N_0 = -174\ \text{dBm/Hz} + 10\log_{10}(BW) + NF \qquad (14)$$

For each simulated sensor node, the propagation losses are determined via the four indoor propagation models presented using Equations (6), (9), (10) and (11). The link quality is hence evaluated by obtaining the RSSI directly from Equation (12) and by computing the SNR using Equations (13) and (14).

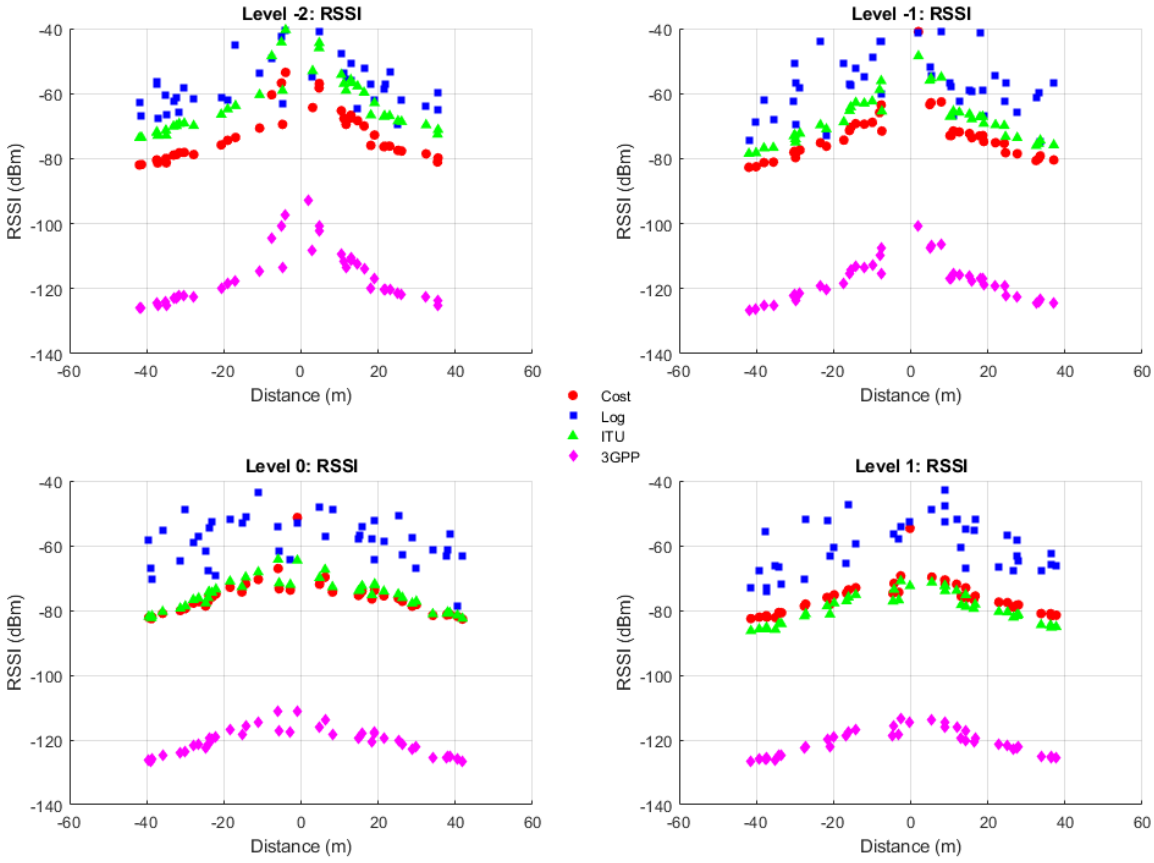

Figure 4.12 – RSSI vs distance for the simulated sensor nodes

Figure 4.12 and Figure 4.13, respectively show the simulated RSSI and SNR link quality metrics per floor level within the simulated building. As expected, a logarithmic decay with distance is noted for all propagation models. Additionally, the COST-231 Multi-Wall model, the Log-Distance Path Loss model and the ITU-R P.1238 model, are noted to yield similar values for both RSSI and SNR, whereas the 3GPP Indoor Hotspot model is noted to yield much lower values. In Chapter 5, these simulated link quality metrics will be compared to the LoRa metrics gathered from the deployed LoRa WSN and utilised to evaluate which propagation model better captures the simulated environment.

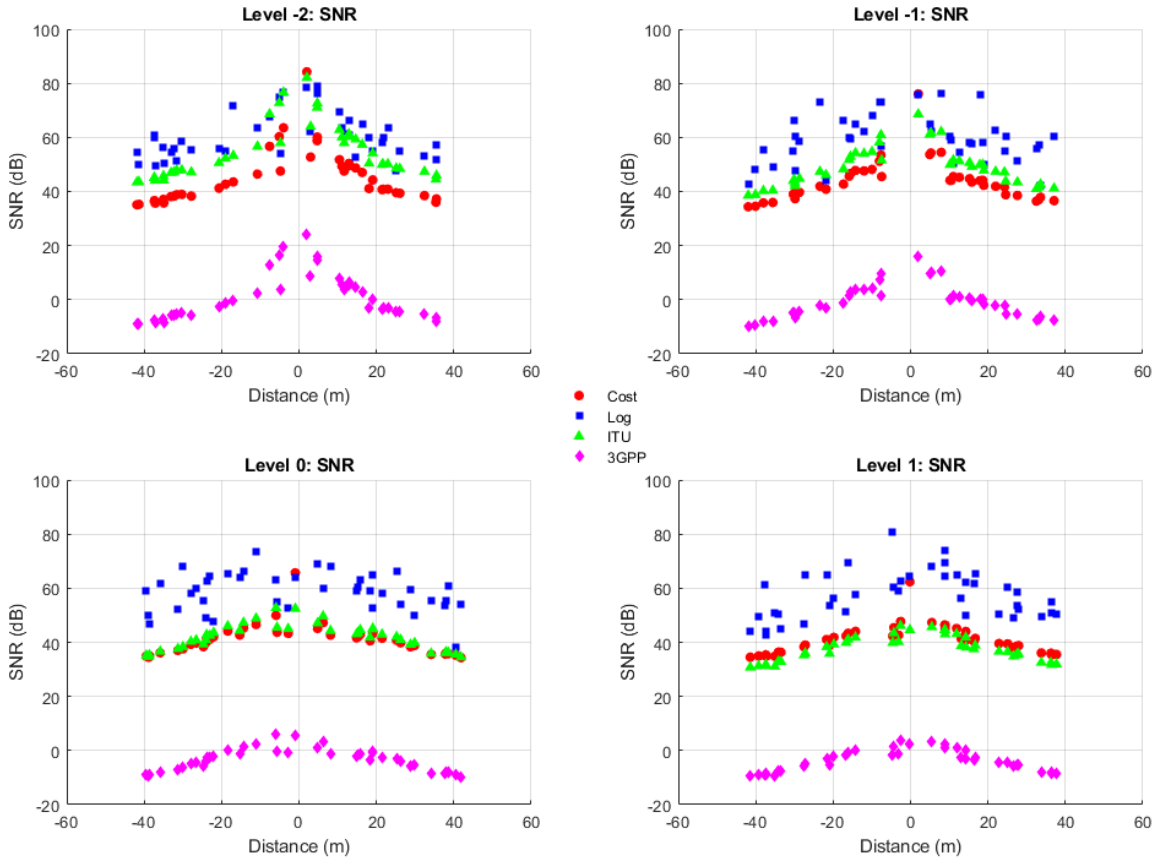

Figure 4.13 – SNR vs distance for the simulated sensor nodes

4.3.4 – Scalability and Duty Cycle Limitations

In this section, equations that highlight the trade-offs between network density, throughput, and regulatory limits are presented. LoRa networks in Europe are subject to duty cycle restrictions when operating in the 868 MHz ISM band. This duty cycle δ is typically around 1%. This regulation limits the active transmission time T_{tx} for each node over a total observation period T_{total} as shown in Equation (15). For example, a sensor node is allowed transmit for a maximum of 36 seconds during a 1-hour period. Furthermore, the maximum transmission power is generally capped at 14 dBm [136, 137].

$$T_{\text{tx}} \leq \delta \, T_{\text{total}} \qquad (15)$$

Scalability is further challenged by the increased probability of packet collision as the number of nodes grows. LoRa employs a pure ALOHA-based medium access scheme. Using this access method, the normalised throughput S is given by Equation (16). In this Equation, G represents the offered traffic, which is the average number of packet transmissions per packet time. This is given by equation (17), where N_{nodes} is the number of identical sensor nodes each sending one packet every T_{interval} seconds [138].

$$S = G \, e^{-2G} \qquad (16)$$

$$G = \frac{N_{nodes} T_{\text{packet}}}{T_{\text{interval}}} \qquad (17)$$

Figure 4.14 shows the graph obtained when evaluating the throughput through Equation (16). The plot shows the throughput S peaking at approximately 0.18, at which point G is approximately 0.5. Beyond this point an increase in ordered traffic G results in a decline in throughput. As a result, an optimised LoRa network should ideally operate with G being in the range of 0.4 to 0.6 to maximise throughput.

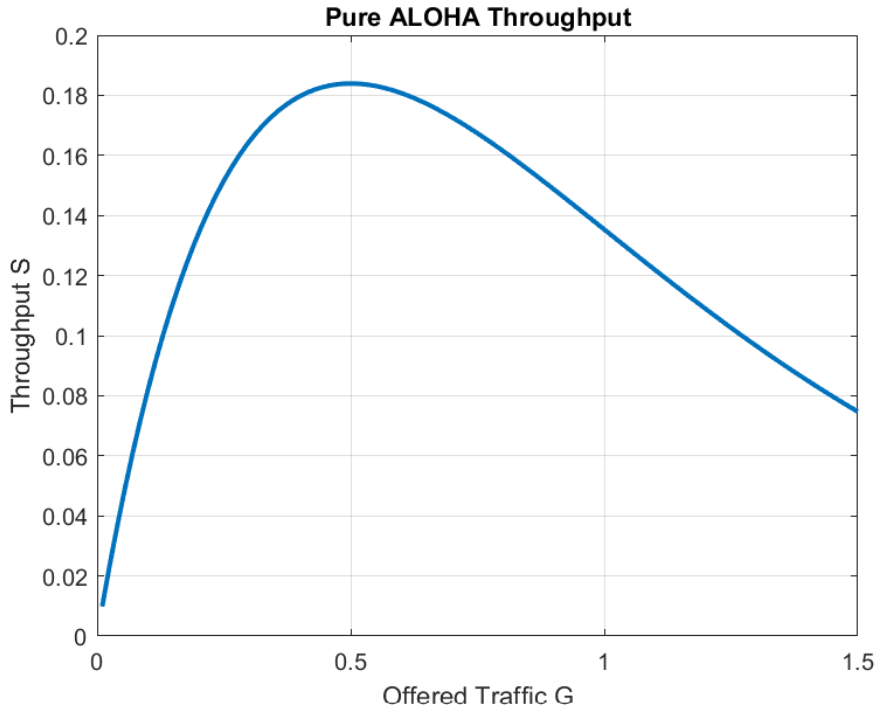

Figure 4.14 – Simulated LoRa pure ALOHA throughput

Furthermore, in order to determine the maximum number of sensor nodes N_{max} that can be supported, Equation (17) can be modified and G set to 0.5 to ensure the maximum theoretical throughput. N_{max} is therefore determined by the ratio of the interval between packet transmissions T_{interval} to the time-on-air of a single packet T_{packet} as shown in Equation (18). Therefore, if larger payloads or higher spreading factors or smaller packet intervals are utilised fewer sensor nodes can be supported [136, 137].

$$N_{max} = \frac{0.5 \times T_{\text{interval}}}{T_{\text{packet}}} \qquad (18)$$

$$T_{\text{packet}} = T_{\text{preamble}} + T_{\text{payload}} \qquad (19)$$

$$T_{\text{preamble}} = (N_{\text{preamble}} + 4.25)T_{\text{sym}} \qquad (20)$$

$$T_{\text{payload}} = N_{\text{payload}} \times T_{\text{sym}} \qquad (21)$$

$$T_{\text{sym}} = \frac{2^{SF}}{BW} \qquad (22)$$

$$N_{\text{payload}} = 8 + max\left(ceil\left[\frac{8PL - 4SF + 28 + 16CRC - 20IH}{4(SF - 2DE)}\right](CR + 4), 0\right) \qquad (23)$$

Additionally, for LoRa transmissions, T_{packet} can be evaluated through equation (19) where T_{preamble} and T_{payload} are given by equations (20) and (21) respectively. T_{sym}in both equations is given by equation (22) where SF is the SF and BW is the bandwidth. Also, N_{preamble} is pre-programmed preamble length whereas N_{payload} is given by equation (23). In this equation, PL is the payload size in bits, whereas the other terms are set according to the options defined by Table 4.4 [139].

Table 4.4 – N_{preamble} equation term options

Equation Term	Value	Option Description
CRC	0	Cyclic redundancy check disabled
	1	Cyclic redundancy check enabled
IH	0	Explicit header mode
	1	Implicit header mode
DE	0	High data rates
	1	Low data rates
CR	1	4/5 coding rate
	2	4/6 coding rate
	3	4/7 coding rate
	4	4/8 coding rate

In order to evaluate N_{max}, the SF is set to 7 and the coding rate is set to 4/5, the lowest possible LoRa setting, such that the highest possible data rates are achieved to minimise battery usage given the low power requirements. Furthermore, given the air quality data to be transmitted, a single LoRa packet is assumed to carry a 42-byte payload resulting in a T_{packet} time of 87ms. Additionally, it is also assumed that each sensor node transmits a single packet every hour. Using these values and assumptions N_{max} is evaluated to be equivalent to 20,690. This is the theoretical maximum number of nodes supported by

this network when operating with optimally maximised throughput. In this WSN a maximum of 100 sensor nodes will be deployed and hence the maximum throughput will not be reached. The WSN will therefore be operating with G being less than 0.5.

4.3.5 – Packet Loss Rates

As defined previously in Chapter 2, another important measure to define the performance of a LoRa WSN is the PLR. In this section, the PLR of the proposed LoRa WSN is simulated by taking into account both collisions from the MAC layer as well as noise from the physical layer. The PLR, P_{LOSS}, is therefore given as a function of $P_{\text{successMAC}}$ and $P_{\text{successPHY}}$ as shown in equation (24). In this equation, the probability of successful transmission $P_{\text{successMAC}}$ is given by Equation (25), where G represents the offered traffic defined previously in Equation (17) whereas $P_{\text{successPHY}}$ is given by Equation (26). [140, 141].

$$P_{\text{LOSS}} = 1 - (P_{\text{successMAC}} \times P_{\text{successPHY}}) \qquad (24)$$

$$P_{\text{successMAC}} = e^{-2G} \qquad (25)$$

$$P_{\text{successPHY}} = \left(P_{cw,ok}\right)^{N_{cw}} \qquad (26)$$

N_{cw}in Equation (26) represents the number of code words in the frame as shown in Equation (27) where N_{bits} is the total number of bits encoded per LoRa frame and k is the number of information bit per code word. Additionally, in Equation (26), $P_{cw,ok}$ represents the probability that a code word is decoded correctly as shown in Equation (28). In this equation, LoRa employs a simple block-type FEC with code word length $n = 4 + CR$ bits and $k = 4$ information bits. For $CR = 1\ or\ 2$ the code only performs error detection and $t = 0$. On the other hand for $CR = 3\ or\ 4$ the code can correct one bit error per code word and $t = 1$ [142].

$$N_{CW} = \frac{N_{bits}}{k} \qquad (27)$$

$$P_{cw,ok} = \sum_{i=0}^{t} \binom{n}{i} p_b^i (1 - p_b)^{n-i} \qquad (28)$$

Additionally, in Equation (28) p_b represents the bit error portability and is given as a function of the symbol error rate SER as shown in equation (29). When analysing the non-coherent orthogonal modulation of the LoRa protocol under additive white Gaussian noise conditions, SER can be approximated as shown in Equation (30). In Equation (30) $G(t)$ is the cumulative distribution function of a central chi-squared distribution with two degrees of freedom and $g\lambda(t)$ is the probability density function of a non-central chi-squared distribution with non-centrality parameter λ given by Equation (31) [143, 144].

$$p_b = \frac{M}{2M - 2} \times SER, \quad M = 2^{SF} \qquad (29)$$

$$SER = 1 - \int_0^{\infty} [G(t)]^{M-1} g\lambda(t) dt \qquad (30)$$

$$\lambda = 2b\left(\frac{E_b}{N_0}\right), \quad b = SF \qquad (31)$$

In Equation (30), $\frac{E_b}{N_0}$ is defined as the SNR ratio per bit and is given by equation (28), where SNR_{linear} is the linear scale SNR, BW is the bandwidth and R_b is the bit rate given by Equation (29). In this equation, SF is the SF, BW is the bandwidth and CR is a coding rate parameter set as shown previously in Table 4.4 [140, 141].

$$\frac{E_b}{N_0} = \frac{SNR_{linear} \times BW}{R_b} \qquad (32)$$

$$R_b = SF \times \frac{BW}{2^{SF}} \times \frac{4}{4 + CR} \qquad (33)$$

Consequently, these equations were used to calculate the PLR due to the MAC and physical layers for the four different propagation models defined previously. The SNR_{linear}

value used in Equation (28) was hence derived by working out the mean SNR values of the simulated sensor nodes resulting from the four propagation models. Additionally, for this simulation, the SF is set to 7, the coding rate is set to 4/5, the payload length is 42 bytes and each node transmits data once every hour.

Figure 4.15 shows the resultant PLR as the number of simulated sensor nodes increase up to N_{max}. For the COST-231 Multi-Wall model, the Log-Distance Path Loss model and the ITU-R P.1238 model, the PLR is very similar and it grows linearly from 0% at 0 nodes to approximately 7.7% at 412 nodes. This suggests that $P_{\text{successPHY}}$ is high enough that collision losses due to the MAC layer dominate the PLR. In contrast, the PLR of the 3GPP Indoor Hotspot model, while still growing linearly, is higher by approximately 4.5%. This suggests that the effect $P_{\text{successPHY}}$ on the PLR for this propagation model, which is more pessimistic due to the lower mean SNR, is not negligible.

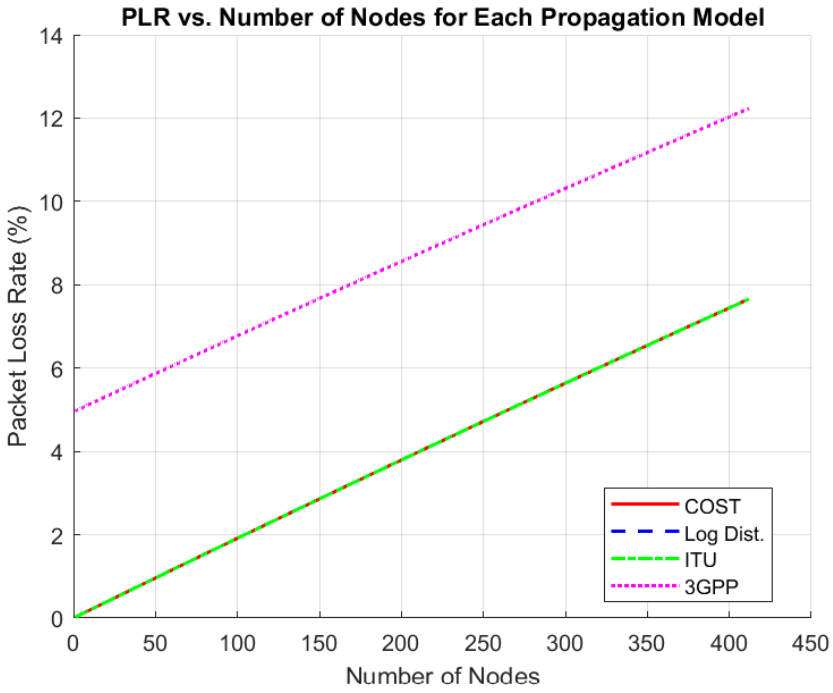

Figure 4.15 – Simulated packet loss rate

4.4 – IoT Messaging and Data Forwarding Server

Following the definition of the LoRa network architecture and the theoretical simulation models, the IoT messaging and data forwarding server was designed. To transfer IoT data between the LoRaWAN servers and different data storage and analysis tools a lightweight messaging protocol is required. The most widely adopted data messaging protocols in IoT applications include Message Queuing Telemetry Transport (MQTT), Constrained Application Protocol (CoAP), Advanced Message Queuing Protocol (AMQP), and Hypertext Transfer Protocol (HTTP). A summary of their key specifications is presented in Table 4.5. MQTT stands out for offering the smallest header size and the broadest range of QoS choices [145, 146].

Table 4.5 – Specifications of IoT messaging protocols

Criteria	**MQTT**	**CoAP**	**AMQP**	**HTTP**
Architecture	Client/Broker	Client/Server Client/Broker	Client/Server Client/Broker	Client/Server
Header Size	2 Byte	4 Byte	8 Byte	Undefined
QoS Reliability	At most once At least once Exactly once	At most once At least once	At most once At least once	Limited
Transport Protocol	TCP	UDP, SCTP	TCP, SCTP	TCP
Security	TLS/SSL	DTLS, IPSec	TLS/SSL, IPSec, SASL	TLS/SSL
Default Port	1883/8883	5683/5684	5671/5672	80/443
Licensing	Open source	Open source	Open source	Free

An MQTT-based data forwarding system employs the lightweight publish-subscribe protocol to transfer the decoded sensor data from the LoRaWAN server to the central database. Such system excels in bi-directional communication with minimal traffic overhead. Scalability remains a key factor for the large-scale deployment of this WSN. While MQTT is widely supported for large-scale deployments by major cloud platforms and can support millions of devices, a potential drawback is that a single MQTT broker represents a

single point of failure and can become a bottleneck when traffic grows. This challenge can be mitigated through advanced techniques like horizontal clustering or broker federation to distribute the load and increase redundancy [145, 146].

For latency, MQTT is generally preferred over HTTP for real-time use cases due to its low overhead. However, issues can still arise, such as gateway connectivity problems, where the gateway needs a stable backhaul connection, or if multicast is not used, which would increase the traffic load and latency. Additionally, security for the sensitive IAQ data is paramount. MQTT supports security through methods like TLS/SSL for encryption, username and password authentication as well as digital certificates. Despite these mechanisms, MQTT deployments face vulnerabilities such as denial of service attacks, man in the middle attacks, and data manipulation. Therefore, for a resilient system, the MQTT-based forwarding must be combined with robust authentication and authorisation controls to restrict device access and actions [145, 146].

Table 4.6 – Cayenne LPP frame structure

1 Byte	1 Byte	N Bytes	1 Byte	1 Byte	M Bytes	…
Data1 Ch.	Data1 Type	Data1	Data2 Ch.	Data2 Type	Data2	…

Table 4.7 – Cayenne LPP data types being used

Data Type	**IPSO**	**Size**	**Resolution**	**Polarity**
Temperature	3303	2 bytes	0.1°C	Signed
Humidity	3304	1 byte	0.5 %	Unsigned
Barometer	3315	2 bytes	0.1 hPa	Unsigned
Illuminance	3301	2 bytes	1	Unsigned
Analog Input	3203	2 bytes	0.01	Signed

As mentioned in the previous section, the Cayenne LPP protocol is used to format the data from the IoT nodes before being sent over LoRa. This protocol is crucial for maximising energy efficiency and throughput due to the compact encoding scheme it possesses. Table 4.6 shows the Cayenne LPP frame structure. This structure allows a data channel field to be set such that each sensor in the IoT device is uniquely identified across

the frame. Moreover, the data type field within the Cayenne LPP frame identifies the data type being used by each channel. Additionally, Table 4.7 below shows the data types which are being used in this work. For each data type the IPSO, size, resolution and polarity are defined.

The Cayenne LPP is compliant with payload size restrictions, including those as low as 11 bytes, and allows multiple sensor readings in a single unique transmission. However, a challenge arises in integration, as some gateway or network server implementations of LPP decoding can be limited and may not support all data types. This requires a manual work-around by re-interpreting data types or performing the decoding outside of the gateway, which adds complexity to the data forwarding process. Figure 4.16 shows the IoT sensor node frame being formatted using Cayenne LPP before being transmitted over LoRa.

```
lpp.addTemperature(1, temperature); // Temperature °C (Size: 2 bytes, Resolution: 0.1 °C Signed)
lpp.addRelativeHumidity(2, humidity); // Humidity %RH    (Size: 1 byte,  Resolution: 0.5% Unsigned)
lpp.addBarometricPressure(3, pressure); // Pressure hPa    (Size: 2 bytes, Resolution: 0.1 hPa Unsigned)
lpp.addAnalogInput(3, vbat_actual); // Battery voltage V (Size: 2 bytes, Resolution: 0.01 Signed)
lpp.addLuminosity(4, tvoc); // TVOC ppb (Size: 2 bytes, Resolution: 1 Unsigned)
lpp.addLuminosity(5, eco2); // eCO2 ppm (Size: 2 bytes, Resolution: 1 Unsigned)
lpp.addLuminosity(6, co2); // CO2 ppm (Size: 2 bytes, Resolution: 1 Unsigned)
lpp.addAnalogInput(7, measurement.mc_1p0); // PM1.0 Mass Concentration µg/m³ (Size: 2 bytes, Resolution: 0.01 Signed)
lpp.addAnalogInput(8, measurement.mc_2p5); // PM2.5 Mass Concentration µg/m³ (Size: 2 bytes, Resolution: 0.01 Signed)
lpp.addAnalogInput(9, measurement.mc_4p0); // PM4.0 Mass Concentration µg/m³ (Size: 2 bytes, Resolution: 0.01 Signed)
lpp.addAnalogInput(10, measurement.mc_10p0); // PM10.0 Mass Concentration µg/m³ (Size: 2 bytes, Resolution: 0.01 Signed)
lpp.addAnalogInput(11, measurement.tps); // Typical Particle Size µm (Size: 2 bytes, Resolution: 0.01 Signed)
```

Figure 4.16 – IoT sensor node frame formatted using the Cayenne LPP

The Cayenne LPP frames are then transmitted via LoRa and captured by the LoRaWAN server. The LoRaWAN server has an integrated MQTT bridge which is utilised to publish the received IoT sensor node IAQ data via MQTT. In order to view the MQTT messages being published, an MQTT broker is required. Based on the configuration settings of the MQTT bridge, a username and password are required for authentication. Once authenticated the MQTT broker is able to subscribe to specific topics according to the messages being published by the MQTT bridge. Figure 4.17 shows a LoRa packet which is being captured using the MQTTBox MQTT broker. Using this MQTT broker we can see the

raw LoRa payload as well as the decoded Cayenne LPP frame and decoded metadata pertaining to that LoRa packet.

Figure 4.17 – LoRa packet captured using MQTTBox

Table 4.8 – Database collections fields

Metadata Collection	**Air Quality Collection**	**Location Collection**
_id (Index)	_id (Index)	_id (Index)
Application ID	Device ID	Device ID
Device ID	Floor	Air Quality Index
Hardware Serial Number	Block	Thermal Comfort Index
Port	Room	Main Pollutant
Frame Counter	Temperature	X Position
Raw Payload	Relative Humidity	Y Position
Battery Voltage	Pressure	Block
Frequency	Volatile Organic Compounds	Level
Modulation	Carbon Dioxide	Date and Time
Data Rate	Particulate Matter PM1.0	
Coding Rate	Particulate Matter PM2.5	
RSSI	Particulate Matter PM4.0	
SNR	Particulate Matter PM10	
Air Time	Typical Particle Size	
Channel	Air Quality Index	
Gateway ID	Thermal Comfort Index	
Date and Time	Main Pollutant	
	Date and Time	

After confirming the proper functioning of the MQTT bridge, a node.js data forwarding server was developed to receive the transmitted MQTT messages and store them in a database, following the database collection fields outlined in Table 4.8. To cater for the two different solutions being developed two variants of this server were created. One of them is hosted on a local node.js server whereas the other one is hosted on a cloud-based node.js hosting service. Once again, a similar authentication process to the one used for the MQTT broker is used for authentication by the MQTT bridge.

Once connected to the MQTT bridge, the node.js server listens for MQTT messages on a particular topic. When an MQTT message is received the node.js server connects to a database to store the received IoT data. Before storing the IoT data in JavaScript Object Notation (JSON) format, the data is processed to generate an AQI and a TCI. In addition to these indices, the primary pollutant responsible for the calculated AQI is also recorded. The implemented AQI and TCI, described in Table 4.9 and Table 4.10 respectively, are based on the methodology outlined in [147].

Table 4.9 – AQI for indoor air quality monitoring

Pollutant	Good (1)	Moderate (2)	Unhealthy (3)	Hazardous (4)	Out of Range
PM10 ($\mu g/m^3$)	0-20	21-150	151-180	181-600	> 600
PM2.5 ($\mu g/m^3$)	0-15	16-40	41-65	66-500	> 500
CO_2 (ppm)	340-600	601-1000	1001-1500	1501-5000	> 5000, < 340
TVOC (ppb)	0-87	88-261	262-430	431-3000	> 3000

Table 4.10 – TCI for indoor air quality monitoring

Comfort	Good (1)	Moderate (2)	Unhealthy (3)	Hazardous (4)	Out of Range
Temperature (^0C)	20-26	17-19.9 26.1-29	7-16.9 29.1-39	0-6.9 39.1-45	> 45 < 0
Relative Humidity (%)	40-70	70.1-80	80.1-90	90.1-100	< 40

Every time a sensor node transfers IAQ data, the generated AQI and TCI indices in the location collection are updated. This results in the generation of location-based AQI and TCI information. The location collection is utilised to store the generated location-based information. A coordinate system mapping the entire building was developed. Moreover, the position of the IoT sensor nodes inside the building is also pre-recorded in the database. Therefore, only an update command is required to update the location collection when receiving an MQTT message.

4.5 – Big Data Storage and Analysis Tools

Big data is usually stored in databases, which are commonly either relational or document-oriented. Relational databases organise data into tables and require normalisation to achieve optimal performance. This normalisation involves additional tables, joins, keys, and indexes, making relational databases difficult to scale in web and cloud-based big data applications. On the other hand, document-oriented databases avoid using structured query language (SQL) and tables, instead storing data as structured JSON-like documents. This approach allows for distributed, horizontally scalable databases that enable quicker and simpler data access through APIs [148].

One of the predominantly used document-oriented databases is MongoDB which is a cross-platform NoSQL database specifically built for modern applications allowing API integrations for data analysis. Once again to meet the requirements of the two different solutions being developed. MongoDB can be deployed either on a local server or else on the cloud using the MongoDB Atlas service. The MongoDB Atlas service enables the deployment of databases on shared cloud clusters. It offers a free tier supporting up to 512 MB of data, with easy scalability to dedicated cloud clusters as needed. MongoDB Atlas also includes a web-based GUI that provides access to real-time performance metrics, as well as data management and security tools. [145, 148].

The selection of MongoDB over a specialised time-series database like InfluxDB, was a choice driven by the project architecture and data heterogeneity. The IoT system not only collects time-series air quality readings but also needs to manage diverse related information, including LoRa metadata and processed indices like AQI and TCI. MongoDB has a flexible and schema-less document model is excellently suited for efficiently storing these varied, complex, and potentially evolving data structures in a single platform. Additionally, it offers ease of adaptation where a purely time-series database might be less flexible [145, 148].


```
_id: ObjectId("5f9c1877a18e20168e0dd823")
dev_id: "fict0a04"
floor: 0
block: "a"
room: 4
temperature_C: 22.5
relative_humidity_RH: 52.5
barometric_pressure_hPa: 1019.8
t_voc_ppb: 9
e_co2_ppm: 412
co2_ppm: 589
pm_1_0_µg_m3: 0.96
pm_2_5_µg_m3: 2.47
pm_4_0_µg_m3: 3.64
pm_10_0_µg_m3: 3.88
typical_particle_size_µm: 0.85
air_quality_index: 1
thermal_comfort_index: 1
main_pollutant: "CO2"
datetime: 2020-10-30T15:43:19.080+00:00
```


Figure 4.18 – Air quality record in the air quality MongoDB database collection

The MongoDB database was set up using a three-replica set configuration to enhance system reliability and support distributed read operations, improving both redundancy and scalability. The database is organised into three distinct collections as outlined earlier in Table 4.8. Figure 4.18 displays an example of an air quality data entry stored in the air quality collection, captured after the database was successfully deployed and the data forwarding server was configured. In addition, Figure 4.19 presents performance metrics for the database. These metrics provide insight into various aspects

such as network throughput, database size growth, and the number of active connections. Notably, red markers on the performance graphs indicate instances when the database server was restarted.

Figure 4.19 – MongoDB database performance metrics

After confirming the database was functioning correctly, data analysis of the IoT-generated information was conducted using a range of tools and services. One such tool is MongoDB Charts, which is used to create visualisations of periodic averages or raw air quality measurements. These charts can be customised with filters to display specific data ranges, highlight individual sensor nodes, or focus on defined time intervals such as daily, weekly, monthly, yearly, or custom durations.

In addition to MongoDB Charts, myDevices is also utilised for data analysis and visualisation. This platform enables the development of simplified, user-friendly dashboards. It also offers a mobile app, improving accessibility and user engagement with air quality data. A key feature of myDevices is its alert system, which allows users to receive email or smartphone notifications when certain gas levels exceed predefined thresholds. These alerts can also be configured to automatically trigger actions, such as activating ventilation systems or increasing airflow, thereby enhancing the system's responsiveness and overall utility.

Chapter 5 – Achieved Results and Novelty

5.1 – Introduction

This section will present the results achieved and compare them to SOA solutions. The novelty achieved compared to these existing solutions is also highlighted. First the battery powered air quality IoT wireless sensor nodes are presented. These are followed by the LoRa-based big data capture and analysis solution.

5.2 – Battery Powered Air Quality IoT Wireless Sensor Node

The fabricated prototypes along with their power consumption results are presented in this section. Additionally, these results are compared to the theoretical results along with a comparison to SOA devices highlighting the novelty achieved.

5.2.1 – 1st Prototype Sensor Node

The designed sensor interfacing and power management board was manufactured on a 50 x 50 mm two-layer printed circuit board (PCB) and assembled as shown in Figure 5.1. Once assembled, the prototype was connected to the Mini Ultra Pro V3 microcontroller board, the SCD30 and SPS30 sensors and a 3 dBi 868 MHz antenna. A C++ program was consequently written and uploaded to the fabricated device serially via the micro-USB connector.

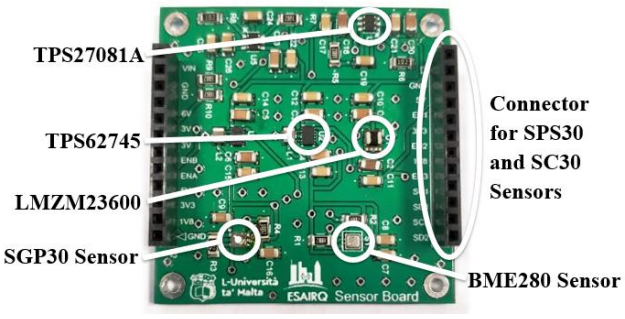

Figure 5.1 – Prototype sensor interfacing and power management board

A Low Power Labs Current Ranger with an accuracy ±0.1% was utilised to measure the power consumption characteristics of the proposed device. The results are gathered in Table 5.1 and compared to the theoretical power consumption calculations in Section 3.3. The sensor node exhibited a sleep mode current of 20 µA which is slightly higher than the estimated 16.8 µA. Additionally, a plot of the active current drawn, shown in Figure 5.2, was used to evaluate an average current demand of 148 mA over a single 31 second read and transmit cycle. Once again, this value is noted to be higher than theoretical value of 112.9 mA calculated previously. This difference is attributed to the light emitting diode (LED) present on the Mini Ultra Pro V3 board and not accounted for in the theoretical calculations. Furthermore, assuming a 6000 mAh battery is used, the average power consumption was calculated to be 1.3 mAh per hour. This results in an estimated battery life of approximately 6 months after taking into account 10% battery discharge safety.

Table 5.1 – Power consumption results of the 1st prototype sensor node

Description	Active Time	Average Active Current	Sleep Current	Electric Charge (1 read transmit cycle/hour)
Theoretical	30 s	112.9 mA	16.8 µA	958 µAh
Actual	31 s	148 mA	20 µA	1.3 mAh

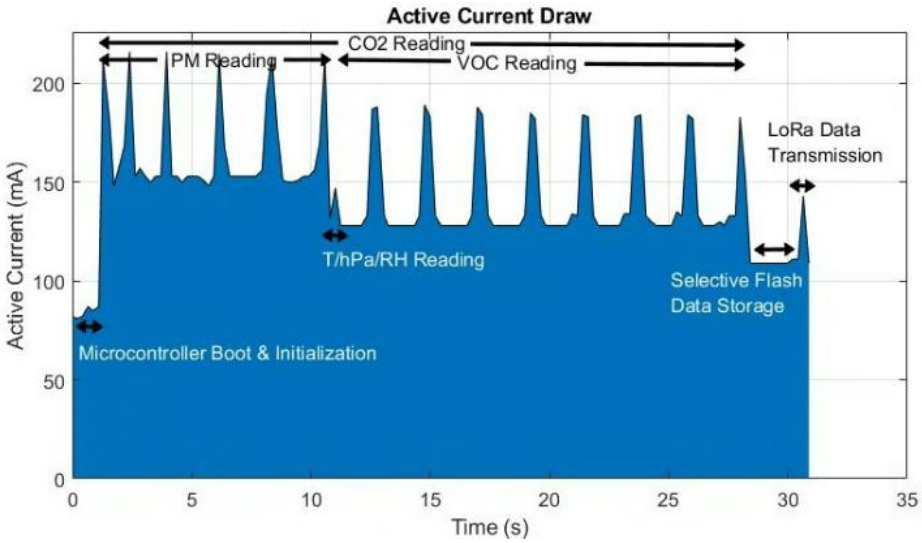

Figure 5.2 – 1st prototype sensor node active current draw

5.2.2 – 2nd Prototype Sensor Node

The prototype sensor node was manufactured on a 100 x 100 mm, two-layer PCB and assembled as illustrated in Figure 5.3. Additionally, a 3 dBi 868 MHz antenna was connected to the on-board LoRa transceiver. For testing purposes, a bootloader was initially programmed into the device using an ATMEL ICE programmer. This step enabled code uploads via the USB COM interface.

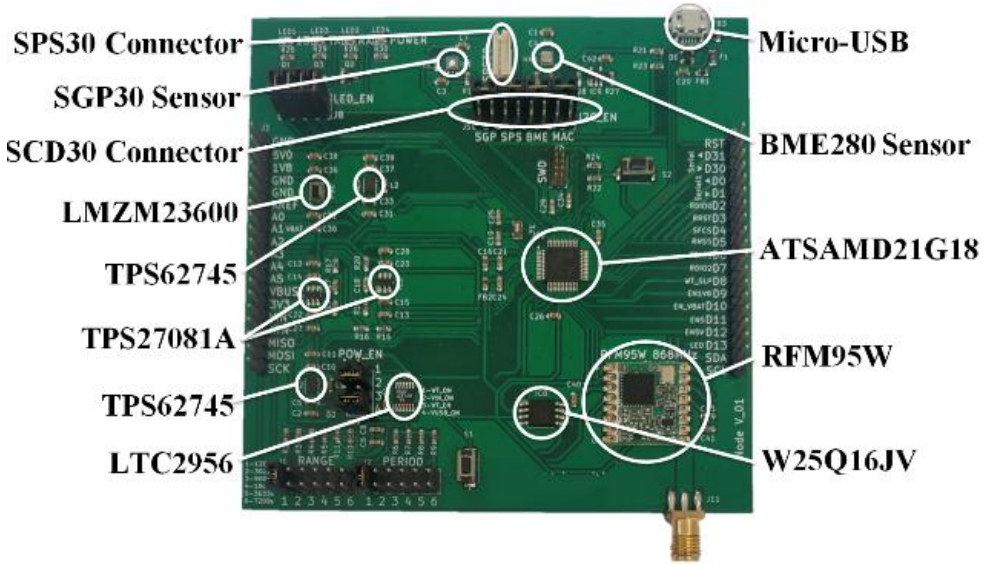

Figure 5.3 – 2nd prototype sensor node

The Low Power Labs Current Ranger was once again used to measure the power characteristics of the proposed prototype. The results, presented in Table 5.2, are compared to the theoretical power calculations outlined in Section 3.4. The resultant sleep mode current was equivalent to 3.2 µA. This is significantly higher that the estimated 960 nA and is attributable to the LTC2956 wake-up timer. The power consumption exhibited by this timer in sleep mode is higher than what is presented as typical in the datasheet. Figure 5.4, which shows the active current waveform, was utilised to evaluate an average active current of 62 mA over one 31-second transmission cycle. This value is in line with was theoretically calculated. Furthermore, with one read and transmit cycle each hour, the

average power consumption is approximately 537 µAh per hour, leading to an approximate 14-month battery life when utilising a 6,000 mAh battery and assuming a 10% battery discharge safety margin. This value is again aligned closely with what was calculated theoretically.

Table 5.2 – Power consumption results of the 2nd prototype sensor node

Description	Active Time	Average Active Current	Sleep Current	Electric Charge (1 read transmit cycle/hour)
Theoretical	30 s	63.2 mA	960 nA	528 µAh
Actual	31 s	62 mA	3.2 µA	537 µAh

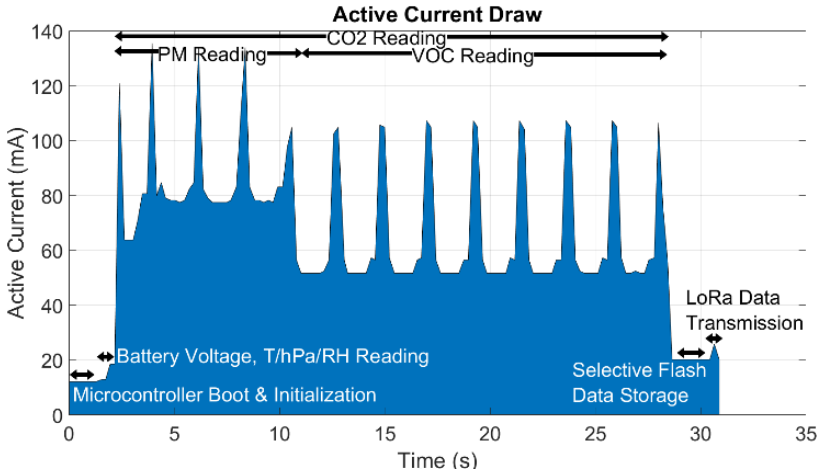

Figure 5.4 – 2nd prototype sensor node active current draw

5.2.3 – 3rd Prototype Sensor Node

The 3rd prototype sensor node was designed with the aim to fit inside a ventilated plastic enclosure. A 117 x 70 mm two-layer PCB was used to fabricate this sensor node which can be seen in its assembled form in Figure 5.5 and Figure 5.6. Once again, a 3 dBi 868 MHz antenna was connected to the on-board LoRa transceiver. Similar to the 2nd prototype node, a bootloader was programmed into the device to enable code uploads via the USB COM interface.

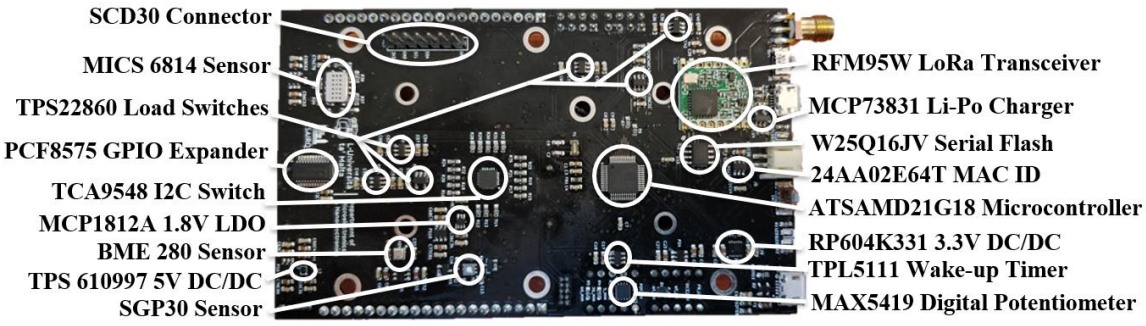

Figure 5.5 – 3rd prototype sensor node frontal view

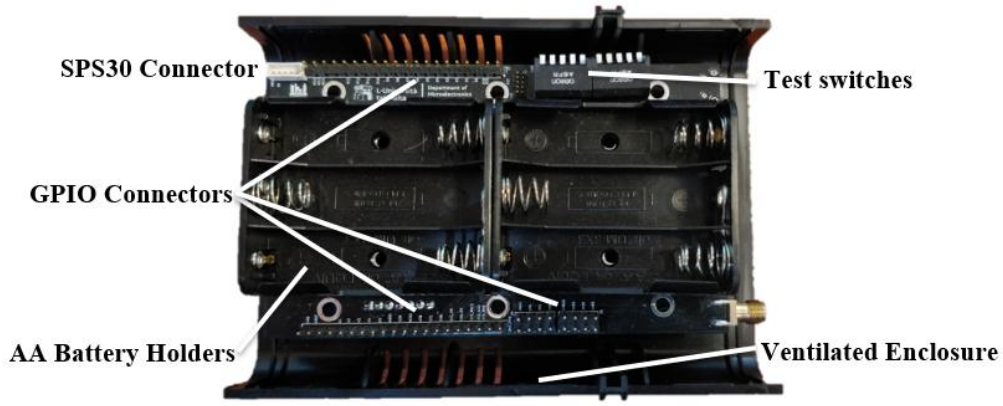

Figure 5.6 – 3rd prototype sensor node backside view

Table 5.3 – Power consumption results of the 3rd prototype sensor node

Description	Active Time	Average Active Current	Sleep Current	Electric Charge (1 read transmit cycle/hour)
Theoretical	30 s	36.5 mA	567 nA	305 µAh
Actual	31 s	44 mA	570 nA	379 µAh

A Low Power Labs Current Ranger was utilised to measure the power consumption of the proposed device. The measured results, shown in Table 5.3, were compared to the theoretical values calculated in Section 3.5. In sleep mode, the device draws 570 nA, which closely matches the theoretical estimate of 567 nA. Figure 5.7, which illustrates the active current waveform, was used to calculate an average active current of 44 mA. This value is slightly above the predicted 36.5 mA, for a full 31-second read and transmit cycle. With one

such cycle occurring per hour, the average power consumption of the prototype is approximately 379 µAh per hour. This value is also marginally higher than the theoretically calculated value of 305 µAh. The estimated battery life for this 3rd prototype is of roughly 20 months using a 6,000 mAh battery, after factoring in a 10% discharge safety margin.

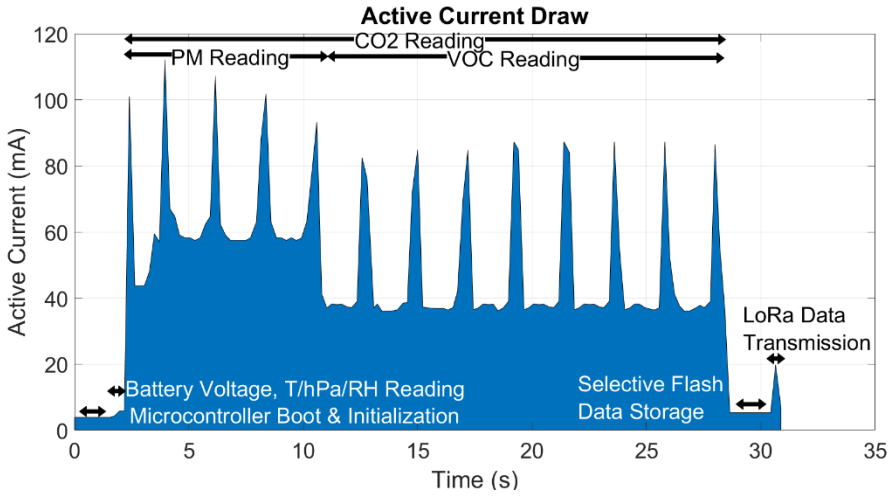

Figure 5.7 – 3rd prototype sensor node active current draw

5.2.4 – 4th Prototype Sensor Node

Figure 5.8 and Figure 5.9 show the power management and microcontroller board of the 4th prototype sensor node. This prototype was fabricated and assembled on a 70 x 75 mm four-layer PCB.

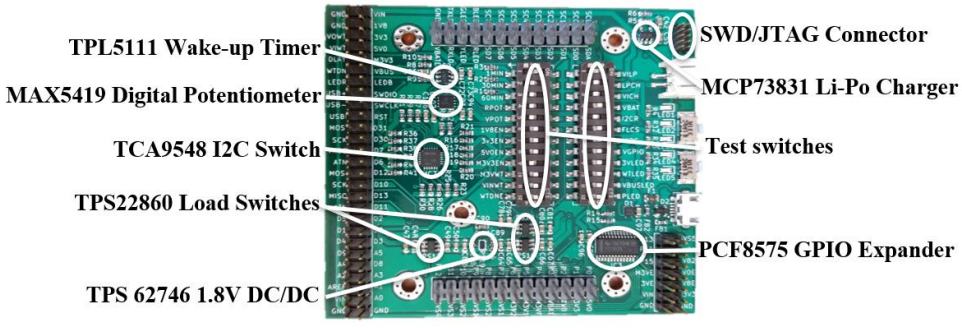

Figure 5.8 – 4th prototype DPM board front view

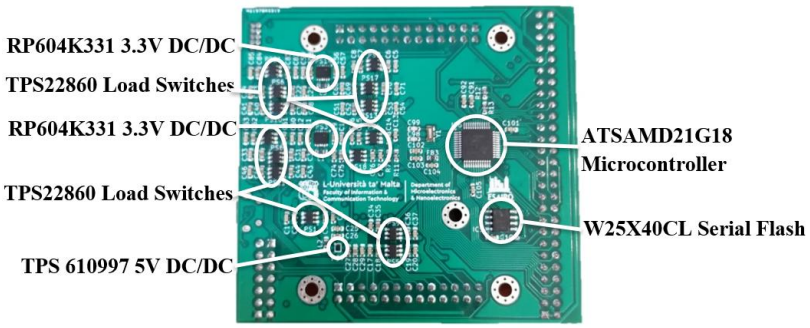

Figure 5.9 – 4th prototype DPM board back view

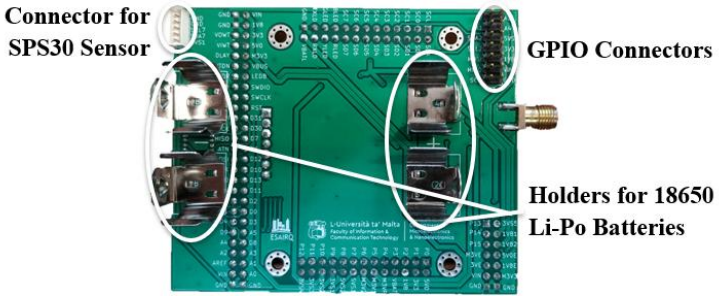

Figure 5.10 – 4th prototype node sensor shield front view

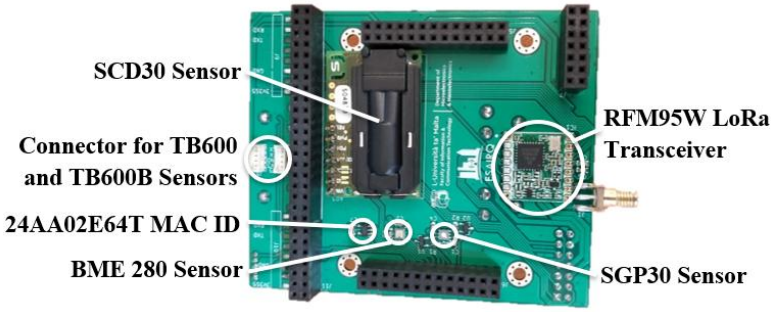

Figure 5.11 – 4th prototype node sensor shield back view

Like the 2nd and 3rd prototype nodes, a bootloader was uploaded to the microcontroller on this board to enable code uploading via the USB COM interface. Given that the prototype node was developed using a modular design approach, a dedicated air quality sensor and radio transceiver shield was also created. This shield, illustrated in Figure 5.10 and Figure 5.11, was fabricated on a 70 x 85 mm two-layer PCB and connects to

the power management and microcontroller board through four mating connectors. The shield is also connected to a 3 dBi 868 MHz antenna.

A second improved sensor shield was also fabricated on a larger 70 x 115 mm two-layer PCB. This improved shield, shown in Figure 5.12 and Figure 5.13, allows more features to be added to the prototype sensor node. Four additional connectors were incorporated into the design to support the integration of further sensors, such as the SPEC digital gas sensor modules or the TB600B formaldehyde sensor. Additionally, the PCB includes two reserved footprints for upcoming gas sensors. These footprints will allow the new sensors to be easily soldered onto the board and seamlessly integrated into the working prototype once they become commercially available.

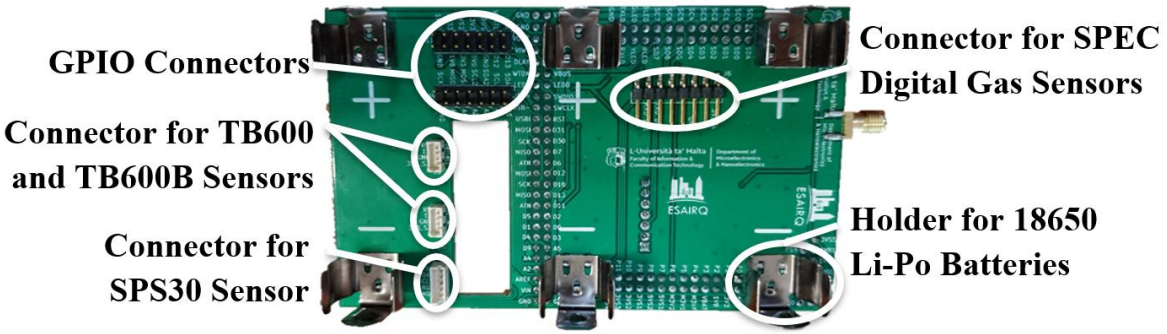

Figure 5.12 – 4th prototype node improved sensor shield front view

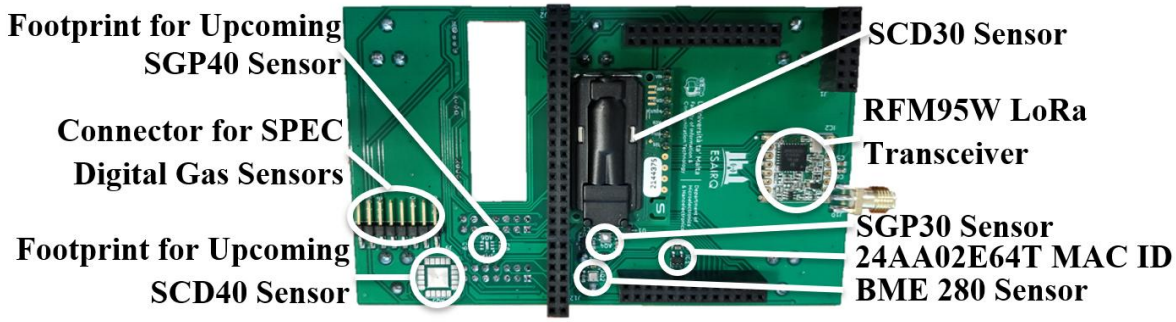

Figure 5.13 – 4th prototype node improved sensor shield back view

An important feature of the redesigned and enhanced shield was to improve the overall ergonomics of the device. As shown in Figure 5.14, the fully assembled 4th prototype sensor node is housed within a ventilated plastic enclosure. To ensure more accurate environmental measurements, the sensors on the shield were strategically positioned as close as possible to the ventilation openings. Additionally, the PCB includes a dedicated cut-out for the SPS30 particulate matter sensor, allowing its air inlet and outlet to remain isolated by the PCB itself, further enhancing measurement accuracy. The shield also includes an additional 18650 Li-Po battery connector, enabling the device to support up to 10,500 mAh of battery capacity when using three 3,500 mAh 18650 Li-Ion cells.

Figure 5.14 – 4th prototype sensor node fully assembled

The Low Power Labs Current Ranger was utilised to measure the power consumption characteristics of the 4th prototype sensor node, with the results shown in Table 5.4 and compared to the theoretical calculations from Section 3.6. In sleep mode, the device draws 270 nA, which is significantly higher than the theoretically calculated value of 83 nA. This difference is attributed to the higher than typically advertised shutdown current of the four load switches. Figure 5.15, which illustrates the active current waveform, was utilised to calculate a value of 38 mA average active current over a 31-second read and

transmit cycle. This slightly exceeds the theoretically calculated value of 36.5 mA. Additionally, with a single transmission cycle per hour, the average power draw is approximately 327 µAh per hour, marginally higher than the theoretical 304 µAh. Consequently, the estimated battery life for this third prototype is roughly 40 months using a 10,500 mAh battery, after accounting for a 10% discharge safety margin.

Table 5.4 – Power consumption results of the 4th prototype sensor node

Description	Active Time	Average Active Current	Sleep Current	Electric Charge (1 read transmit cycle/hour)
Theoretical	30 s	36.5 mA	83 nA	304 µAh
Actual	31 s	38 mA	270 nA	327 µAh

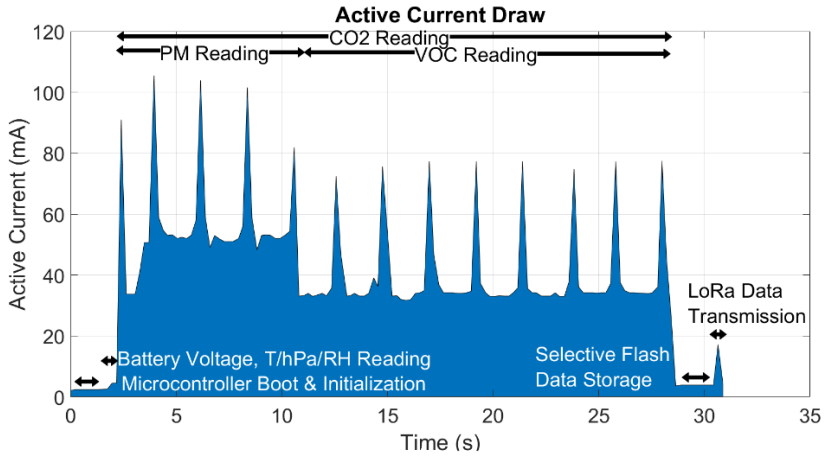

Figure 5.15 – 4th prototype sensor node active current draw

A detailed breakdown cost of this 4th prototype node is also presented in Table 5.5 below. The table shows the individual cost of the different components such as the sensors, batteries and PCBs making up this prototype. Additionally, the costs were calculated when buying 50 pieces of each component. This is considered to be a very low volume and a significant drop in price would be achieved if the quantities were to be increased to a few hundreds. However, despite the low volumes the proposed prototype is still below the 175 Euro mark.

Table 5.5 – Cost breakdown of the 4th prototype sensor node

Item	Description	Unit Price (Qty: 50)
MCU PCB	Fabrication, components and soldering	€ 50
Shield PCB	Fabrication, components and soldering	€ 40
SCD30 [101]	Carbon dioxide sensor	€ 38
SPS30 [102]	Particulate matter sensor	€ 29
Cable	Particulate matter cable	€ 2
INR18650-35E [149]	3x 18650 3500 mAh batteries	€ 9
TX868-JKD-20 [150]	3 dBi 868 MHz antenna	€ 2
Enclosure	135 x 95 x 45 mm enclosure	€2.60
9900	4x Philips screws	€0.40
	Total	**€173**

5.2.5 – Novelty and Innovation

To quantify the progress achieved the specifications of proposed prototype sensor nodes are first compared to the target specifications which were set initially. The novelty achieved by these results is then highlighted by comparing them to the SOA nodes found in literature as well commercially available SOA nodes.

Table 5.6 compares the target specifications to the specifications achieved by the four iterations of the proposed sensor nodes. The active read time per read cycle is mostly dependant on the response time of the sensors. The 31 second result achieved is very close to the target specification and to reduce this, sensors with a faster response time are required. The average active current achieved by the 2nd, 3rd and 4th prototype nodes is respectively, 17.3%, 41.3% and 49.3% less than the target specification. Similarly, the sleep mode current achieved by the 2nd, 3rd and 4th prototype nodes is respectively, 36%, 88.6% and 94.6% less than the target specification. These power consumption results enable the device to exceed the target battery lifetime specification with a maximum projected 40-month battery life attained by the 4th prototype sensor node.

Table 5.6 – Target vs actual prototype nodes power consumption specifications

Specification		Target	1st Prototype	2nd Prototype	3rd Prototype	4th Prototype
Active time per read cycle (seconds)		30	31	31	31	31
Average Active current per read cycle (mA)	Theoretical	59	112.9	63.2	36.5	36.5
	Actual		**148**	**62**	**44**	**38**
Sleep mode current (µA)	Theoretical	10	16.8	0.96	0.567	0.083
	Actual		**20**	**3.2**	**0.57**	**0.27**
Hourly average power consumption (µAh)	Theoretical	499	958	528	305	304
	Actual		**1300**	**537**	**379**	**327**
Input supply voltage range (V)		4 – 6	4 – 8	4 – 8	2.7 – 5.25	2.7 – 5.25
Battery capacity (mAh)		6,387	6,000	6,000	6,000	10,500
Battery life (~ months)		16	6	14	20	40

Additionally, Table 5.6 also shows a comparison of the theoretical and actual power consumption results of the prototype nodes. The theoretical estimates generally matched the measured power consumption values with the exception of a few metrics. In the 1st prototype the actual power consumption metrics were higher than the theoretical estimates and this is partially attributed to the on-board LED which was not accounted for in the theoretical calculations. In the 2nd prototype the sleep current was higher than estimated due to the higher wake-up timer quiescent current. The 3rd prototype closely matched the estimated results with only the average current being slightly higher. The 4th prototype had higher sleep current than the theoretically estimated value this is attributed to the higher than advertised shutdown current of the load switches.

As discussed earlier, most SOA air quality sensor nodes presented in the literature, such as those referenced in [4], are either powered by mains electricity or exhibit very limited battery life. Nevertheless, a comparison was made between the proposed low-power air quality sensor node and battery-operated SOA nodes reported in prior studies, as outlined in Table 5.7. The sensor node presented in this work offers a more comprehensive set of air quality measurements than most comparable SOA battery powered systems. Unlike the works in [75], [76], [77], and [78], this system is the only one to include a full suite of sensors. Specifically, it is the only system to feature volatile organic compound sensing and provides the most granular particulate matter measurements. As a

result, this significantly expands its sensing capability beyond systems like [77] and [78] which lack both volatile organic compound and particulate matter sensors, or [75] and [76] which additionally lack a carbon dioxide sensor.

Table 5.7 – Comparison with SOA works found in literature

Specification	[75]	[76]	[77]	[78]	This Work			
Temperature	Yes	Yes	Yes	Yes	Yes			
Humidity	Yes	Yes	Yes	Yes	Yes			
Pressure	Yes	Yes	Yes	No	Yes			
Carbon Dioxide	No	No	Yes (±3%)	Yes (±3%)	Yes (±3%)			
Volatile Organic Compounds	No	No	No	No	Yes (±15%)			
Particulate Matter	No	Yes	No	No	PM1.0,2.5 (±10%) PM4.0,10 (±25%)			
Additional Sensors	CO, NO2	No	Light	No	UART, I2C, SPI, Analogue			
Wireless Interface	Bluetooth	LoRa	Wi-Fi	BLE	LoRa			
Active time per read cycle	16 seconds	50 seconds	28 seconds	N/A	31 seconds			
Duty Cycle	0.44 %	1.39 %	0.78 %	N/A	0.86 %			
Average active current per read cycle	15.8 mA	70 mA	19.89 mA	130 µA	262 mA	62 mA	44 mA	38 mA
Sleep mode current	500 µA	1 mA	10 µA	10 µA	20 µA	3.2 µA	570 nA	270 nA
Average power consumption per hour (1 read/transmit cycle per hour)	568 µAh	2 mAh	165 µAh	N/A	2.3 mAh	537 µAh	379 µAh	327 µAh
Battery capacity (mAh)	600	5,200	1,500	7,500	6,000	6,000	6,000	10,000
Battery life (10% discharge safety)	~40 days	~3 months	~11 months	~7 months	~3 months	~14 months	~20 months	~40 months

Furthermore, the best performing 4th prototype node has the lowest sleep mode current out of all the reviewed devices. The proposed node achieves a sleep mode current value of 270 nA which is significantly lower than the SOA value of 10 µA achieved by [77] and [78]. Furthermore, the proposed device achieves the longest battery life when compared to the SOA works due to the low average power consumption and the largest battery capacity. The 40-month battery longevity achieved is significantly higher than the best SOA battery life of 11 months. However, despite achieving the longest battery life, some of the SOA work report a lower average power consumption than the proposed nodes.

Specifically, [77] reports better average power performance, however it does not include volatile organic compound or particulate matter sensors. For comparison, in the

2nd prototype, these two sensors alone contribute approximately 71% of the total active current. If they were excluded, the resulting average power consumption would be around 158 µAh. This represents a 4.24% reduction compared to [77], despite still offering a broader sensing capability. Moreover, the work in [78] despite not mentioning the duty cycle time claims a significantly lower active current then the proposed sensor node. However, the work in [78] only claims a battery life of 7 months when utilising a 7,500 mAh battery. Using the same battery capacity of 7,500 mAh, the proposed 4th prototype node would have a battery life of 30 months which would still significantly higher than the work in [78].

Table 5.8 – Comparison of the 4th prototype with commercially available SOA nodes

Specification	IQAir Visual Pro [80]	Kaiterra Laser Egg [81]	Honeywell Air Quality Monitor [82]	PocketLab Air [83]	Airthings Wave Plus [84]	This Work 4th Prototype
Temperature	Yes	Yes	Yes	Yes	Yes	Yes
Humidity	Yes	Yes	Yes	Yes	Yes	Yes
Pressure	No	No	No	Yes	Yes	Yes
CO2	Yes (N/A)	Yes (±3%)	Yes (N/A)	Yes (±3%)	Yes (±3%)	Yes (±3%)
VOC	No	No	Yes (N/A)	No	Yes (N/A)	Yes (±15%)
PM	PM2.5 (N/A)	PM2.5 (±10%)	PM2.5 (N/A)	PM1.0, 2.5,10 (±10%)	No	PM1.0, 2.5 (±10%) PM4.0,10 (±25%)
Additional Sensors	No	No	HCHO (N/A)	Ozone (±15%)	Radon (±20%)	UART, I2C, SPI, Analogue
Data Analysis	App + Cloud	App	App	App	App + Cloud	App + Cloud
Wireless Interface	Wi-Fi, BLE	Wi-Fi	Wi-Fi	BLE	BLE, 868MHz	LoRa
Battery	Li-Po (1900mAh)	Li-Po (2200mAh)	Li-Po (2600mAh)	Li-Po (3500mAh)	2xAA (6000mAh)	Li-Ion (10,500mAh)
Battery Life	4 hrs	8 hrs	24 hours	~3 days	~16 months	~40 months

Table 5.8 provides a comparison between the proposed prototype sensor node and commercially available SOA air quality monitoring devices. The battery life of the proposed node surpasses all commercial counterparts. For an equitable comparison, assuming the 4th prototype is equipped with a 6000 mAh battery, it would offer an estimated battery life

of 23 months, exceeding that of the Airthings Wave Plus by approximately 44%. However, it is not clear how often the Airthings Wave Plus transmits air quality data as it only specifies a sensor sampling rate of 5 minutes. This suggests the Airthings Wave Plus is not switched off as is the case in this work but instead of DPM it uses a different approach by keeping the sensors powered on in a low power mode. In fact, the data sheet of the Airthings Wave plus states that the integrated air quality sensors have a settling time of 7 days.

In addition to longer battery life, the prototype leverages low-cost, SOA gas sensing technologies to deliver broader measurement capabilities than those found in commercial devices. For instance, unlike many commercial units that only support PM2.5 detections, the prototype includes a particulate matter sensor capable of measuring PM1.0, PM4.0, and PM10 levels as well. This design also includes both digital and analogue interfaces, making the system adaptable and easily expandable with new sensors. Despite being a prototype and produced in limited quantities, the proposed sensor node remains the most cost-effective solution among those compared.

5.3 – LoRa-Based Big Data Capture and Analysis System

The results generated from the deployed LoRa-based big data capture and analysis system are presented in this section. In particular, the simulated results are compared with the LoRa meta data collected from the deployed network. Furthermore, the collected air quality data gathered is also analysed whilst highlighting the novelty achieved by the LoRa-based big data capture and analysis system.

5.3.1 – LoRa Meta Data Analysis

LoRa meta data analysis on the deployed WSN is presented in this section. Specifically, an in-depth analysis using the measured RSSI, SNR and PLR values is carried out and compared with the theoretical model presented previously in Chapter 4.

After confirming the proper functioning of the LoRa network architecture, ten prototype IAQ IoT sensor nodes were deployed within a fully enclosed office building, alongside a LoRa gateway. This deployment was carefully planned to ensure optimal signal coverage throughout the complex internal structure of the building. The building, previously described in Chapter 4, is managed by a BMS that automatically regulates internal environmental conditions such as temperature, humidity, and ventilation. To improve energy efficiency, the ventilation system recirculates indoor air while blending it with fresh outdoor air. Maintaining the correct balance between fresh and recycled air is essential for sustaining good indoor air quality. This setup makes the building an ideal test environment for the developed IAQ big data capture and analysis system. By continuously monitoring air quality, the deployed sensor network can supply the BMS with critical metrics, enhancing its ability to maintain a healthy and efficient indoor environment.

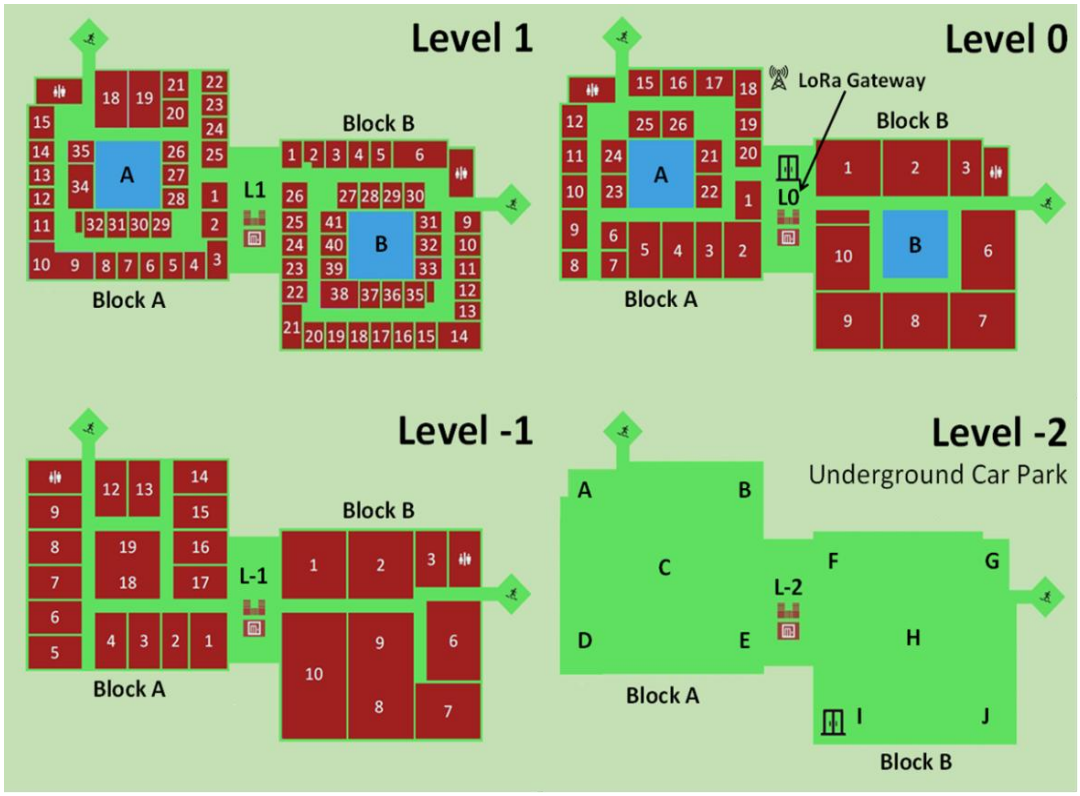

Figure 5.16 – Faculty of ICT building floor plan with gateway installed at level 0

A single LoRa gateway with a high sensitivity of -142 dBm was strategically installed at a central point within the building on Level 0, as illustrated in Figure 5.16. To evaluate network performance, the IoT wireless sensor nodes were placed in various rooms and floors throughout the building. At each location, multiple data packets were transmitted, and key transmission metadata, including the distance from the gateway, the RSSI, and the SNR, was recorded. To maintain consistency and control throughout the testing process, the LoRa transceiver parameters were fixed according to the configuration detailed in Table 5.9. The SF was deliberately set to 7, which is the lowest possible setting. This results in the highest data rates but the shortest communication range, thereby representing the most challenging or worst-case scenario for signal coverage. Additionally, these test parameters were aligned with those used in the theoretical simulations, allowing for a meaningful comparison between practical results and predicted performance.

Table 5.9 – LoRa parameters used for testing

Spreading Factor	Bandwidth	Coding Rate	Tx Power	Minimum SNR	Minimum RSSI
7	125 kHz	4/5	14 dBm	-7.5 dB	-142.5 dBm

Figure 5.17 and Figure 5.18 present the recorded RSSI and SNR values measured at various locations throughout the building using the specified LoRa configuration. These results are also compared with the outputs of the four theoretical propagation models to validate and benchmark real-world performance against simulated expectations. Despite operating with the LoRa configuration that provides the shortest communication range, a single centrally positioned gateway was sufficient to achieve strong coverage across the majority of the building. Packet loss due to SNR falling below the minimum threshold occurred only at the extremities of the basement level This indicates that, while the current setup delivers near-complete coverage, the deployment of a second gateway would be necessary to ensure reliable communication throughout the entire building.

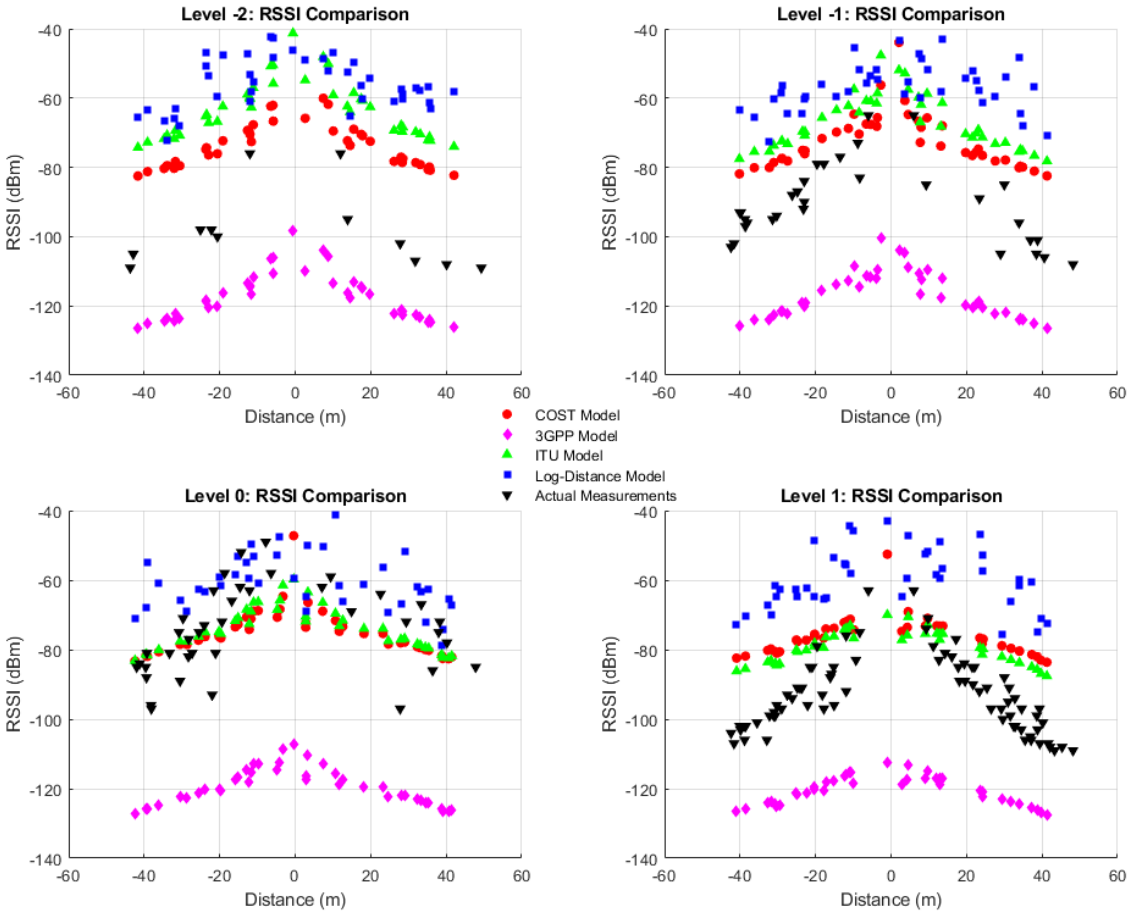

Figure 5.17 – Measured RSSI comparison to simulated propagation models

Furthermore, comparing these measured RSSI results to the theoretical simulated model results, it can be observed that at distances close to 15m the performance of the WSN inside the building can be closely modelled using either of the COST-231 Multi-wall model or the ITU-R P.1238 model, all of which have similar performance. However, at further distances, greater than 15m, RSSI values are noted to be lower than what simulated by these models, and tend to approach more the values simulated by the 3GPP Indoor hotspot model. In contrast, measured SNR values are observed to be very closely modelled by 3GPP Indoor hotspot model at all distances. Hence, the measured SNR values are only marginally higher than the simulated SNR values obtained from the 3GPP indoor hotspot model.

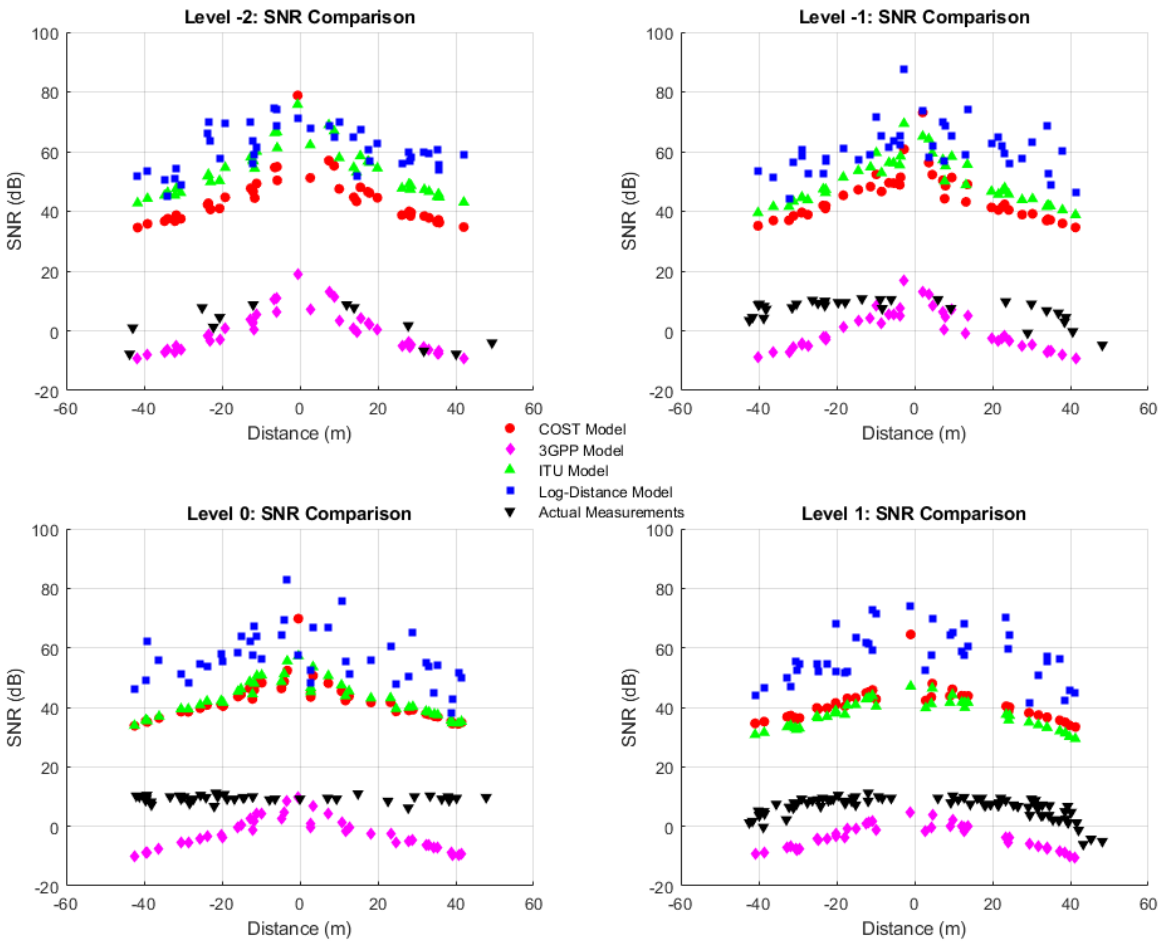

Figure 5.18 – Measured SNR comparison to simulated propagation models

Further analysis of this result shows that at close range measured RSSI matched the COST-231 Multi-Wall and ITU-R P.1238 models because these models are explicitly designed to account for losses due to a limited number of specific obstacles like internal walls and floors. At close range, the signal path is relatively straightforward, and these deterministic models accurately quantify the primary attenuation caused by the first few obstructions between the node and the gateway. However, the rapid drop in RSSI observed beyond 15 m aligns more closely with the pessimistic 3GPP Indoor Hotspot model. Suggesting that at greater distances, the signal path accumulates significantly more degradation due to unaccounted for obstructions and multi-path effects. Furthermore, in a dense and complex indoor environment, longer links encounter a higher density of features such as equipment

and furniture which introduce increased shadowing and fading not fully factored into the simpler wall floor loss models.

Thus since the 3GPP model is inherently more pessimistic, it is a better fit for this complex and high-loss scenario. Additionally, the fact that the measured SNR values consistently track the results of the 3GPP Indoor Hotspot model at all distances suggests that this model accurately captures the overall noise floor and interference levels that dominate the signal quality in the deployed environment. SNR is also a better indicator of link quality than RSSI as it incorporates the noise. In this real world indoor network, background RF noise and interference may be high and consistent throughout the building, a factor the 3GPP model seems to model effectively, thus making it the best predictor of the overall link quality regardless of distance.

Once optimal coverage by the gateway across the building was ensured, 32 prototype nodes were installed within the Faculty of ICT building alongside the single LoRa gateway. Table 5.10 shows a list of these deployed devices together with their respective measured QoS metrics. The deployed sensor nodes are uniquely identified by their device ID and were deployed in key rooms such as offices, lecture rooms, laboratories and the kitchen. Furthermore, the table also shows the distance between each deployed sensor node and the gateway. The sensor nodes in the table are sorted by distance to the gateway which ranges from 5 m for the closest node to 47.8 m for the furthest node.

Additionally, along with the numerical values shown in Table 5.10, Figure 5.19 shows a depiction of the mean values for RSSI, SNR and PLR per deployed sensor node. These mean values were computed by evaluating the mean over a prolonged period of time for each QoS metric. Observing the mean RSSI it is noted that this decrease exponentially as the distance increase from -35.5 dBm for the closest node to -109.3 dBm for the second farthest node. Furthermore, in some cases despite sensor nodes being closer than others to the gateway, these have a lower RSSI value. This is probably due to additional partitions which are present between the sensor node and the gateway. Similarly, SNR values are noted to

decrease with distance from 12.7 dB for the closest nodes to -4.2 dB for the furthest sensor nodes. Finally, the PLR is noted to fluctuate between 1.3% to 12.3% and is greatly dependant on the physical link quality metrics as shown in the simulated model.

Table 5.10 – ICT building measured LoRa QoS metrics per deployed device

Device ID	Room Type	Distance to Gateway (m)	Mean RSSI (dBm)	Mean SNR (dB)	Mean PLR (%)
IAQ-10063	Lobby	5	-35.5	12.7	2.2
IAQ-10061	Lecture	7.2	-42.8	12.7	4.2
IAQ-10003	Corridor	8.1	-55.8	8.8	1.3
IAQ-10060	Lecture	8.4	-44.2	12.7	3.2
IAQ-10021	Office	8.7	-56.6	9.1	2.2
IAQ-10016	Lecture	9.3	-57.4	9.1	2.3
IAQ-10062	Lecture	9.7	-54.1	12.7	3.7
IAQ-10020	Laboratory	10.2	-58.7	9.1	2.5
IAQ-10007	Office	10.2	-53.3	8.9	2.1
IAQ-10015	Corridor	17.5	-59	9.1	2.1
IAQ-10013	Office	19.6	-60.4	9	1.8
IAQ-10008	Corridor	21.3	-60.2	9.2	2
IAQ-10019	Laboratory	25.8	-60.7	9.2	2.6
IAQ-10009	Lecture	26.2	-61.4	8.6	2.5
IAQ-10058	Lecture	28.5	-75.2	12.4	3.6
IAQ-10010	Lecture	29.4	-87.3	6.9	2.4
IAQ-10017	Office	29.7	-61.9	9.3	2.4
IAQ-10014	Laboratory	29.9	-81.8	8.4	2.1
IAQ-10055	Lecture	30.3	-97.7	5.8	4
IAQ-10018	Office	30.5	-68.2	7.1	4.2
IAQ-10006	Laboratory	30.8	-73.6	9.5	2.5
IAQ-10004	Kitchen	31	-103.8	-2.1	4.8
IAQ-10012	Office	32.3	-82.6	8.8	1.3
IAQ-10005	Office	34.5	-101.3	-4.2	12.3
IAQ-10011	Office	34.9	-85.9	7	2.3
IAQ-10054	Lecture	36.4	-104.4	0.6	6.2
IAQ-10002	Kitchen	40.1	-95	0.1	6.7
IAQ-10059	Lecture	40.2	-105.6	-0.4	6.6
IAQ-10052	Lecture	41	-104.8	-3.7	7.2
IAQ-10056	Lecture	43.7	-106	0.7	8.8
IAQ-10057	Lecture	46.2	-109.3	-3.6	10.3
IAQ-10053	Lecture	47.8	-108.9	-4.2	6.6

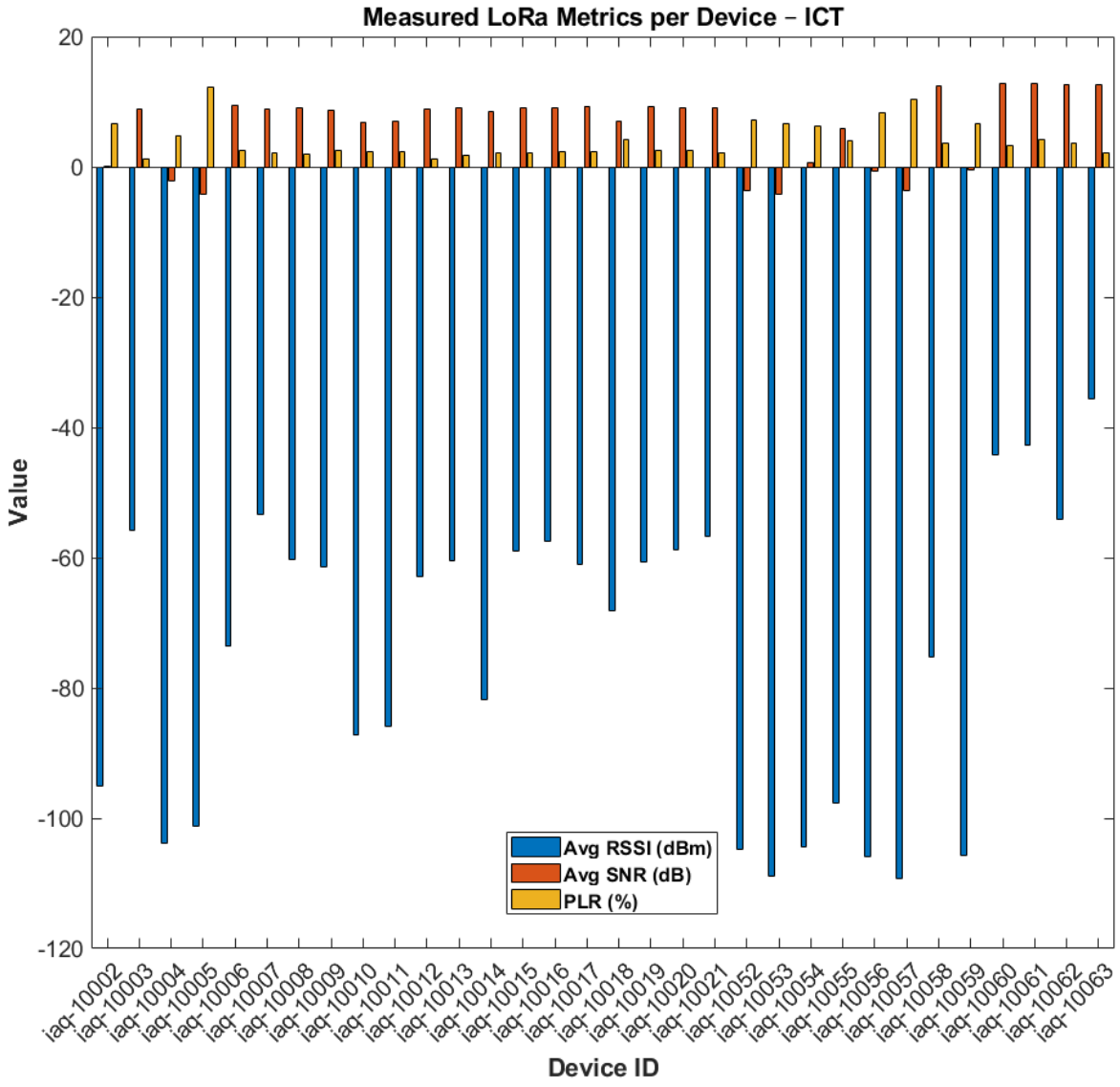

Figure 5.19 – ICT building measured LoRa QoS metrics per deployed device

Additionally, Table 5.11 shows the mean distance to gateway, mean RSSI, mean SNR and mean PLR values obtained from the measured data across a prolonged period of time as well as the four simulated propagation models. Analysing this data, it is observed that both the deployed WSN as well as the simulated WSN have similar mean sensor node distances to the gateway, with these being 25.8 m and 26.4 m respectively, and hence further validating these results.

Table 5.11 – Theoretical average RSSI and SNR comparison to actual measurements

Mean Value	COST-231	3GPP Indoor Hotspot	ITU-R P.1238	Log-Distance	Actual Measurement
Distance to Gateway (m)	26.4				25.8
RSSI (dBm)	-75	-119	-72	-59	-75.4
SNR (dB)	42	-2	45	58	6.2
PLR (%)	0.6%	5.5%	0.6%	0.6%	4%

Furthermore, it is observed that the mean measured RSSI of -75.4 dBm is very close to both the COST-231 multiwall model and the ITU-R P.1238 model, each having a mean simulated RSSI value of -75 dBm and -72 dBm respectively. On the other hand, comparing the mean measured SNR value of 6 dB to the simulated average values, it is observed that the 3GPP Indoor Hotspot model is closest with a mean SNR value of -2 dB. Additionally, the measured mean PLR of 4% is also noted to be closest to the 5.5% simulated PLR of the 3GPP Indoor Hotspot model. The PLR is hence greatly affected by noise on the physical layer and the slightly better PLR achieved by the deployed WSN is attributed to the higher mean RSSI and mean SNR values achieved compared to the 3GPP Indoor Hotspot model.

The observed pattern indicates that while the COST-231 multiwall and ITU-R P.1238 models provide a reasonable estimate of the gross signal power RSSI, they drastically fail to account for ambient noise and fast fading effects that degrade the signal quality. In contrast, the 3GPP Indoor Hotspot model is more accurate for SNR and PLR because its predictions implicitly incorporate greater signal degradation from effects such as multipath interference or clutter and a generally higher and more conservative estimate of the noise floor. This inherent pessimism better mirrors the challenging communication environment were the performance of the network is limited by the physical link quality, where low SNR leads to higher PLR. The slight improvement in the measured PLR compared to the simulated 3GPP model is logically attributed to the measured SNR and RSSI values being marginally better than the model's most pessimistic predictions, meaning collisions were

slightly less dominant than predicted. This confirms that network quality is determined by overcoming physical layer noise and not simply achieving a target RSSI.

Following validation of the simulated WSN model within the ICT building, the deployed WSN was extended to a larger scale across the whole University of Malta campus. In total, 100 sensor nodes alongside 10 gateways were deployed across 10 buildings within the campus. Figure 5.20 shows a map of the sensor node deployment locations across several buildings within the University campus.

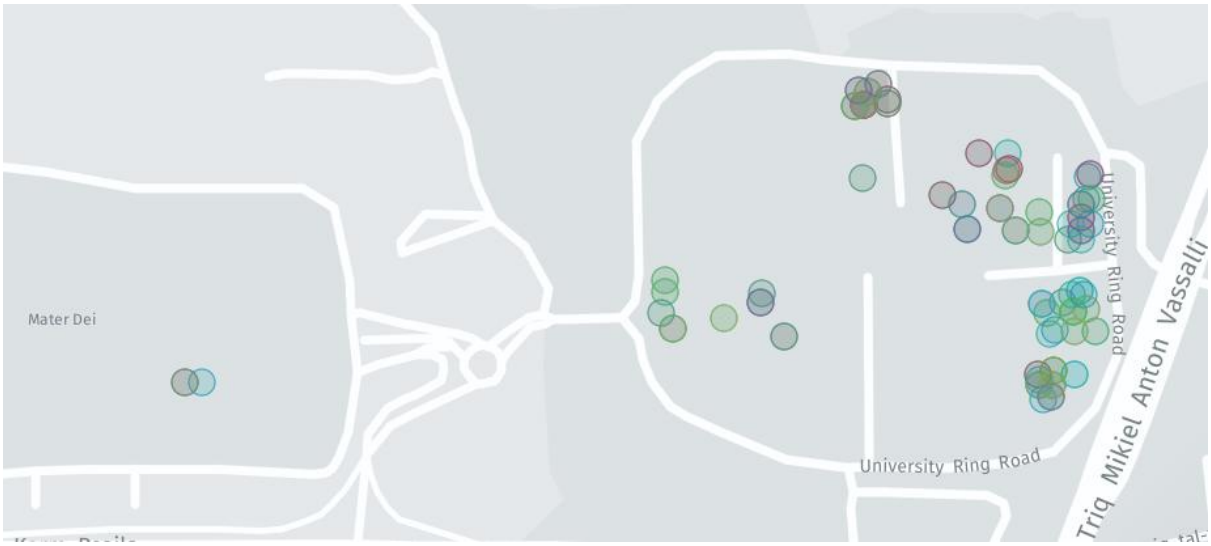

Figure 5.20 – Air quality sensor node deployment locations within the University of Malta campus

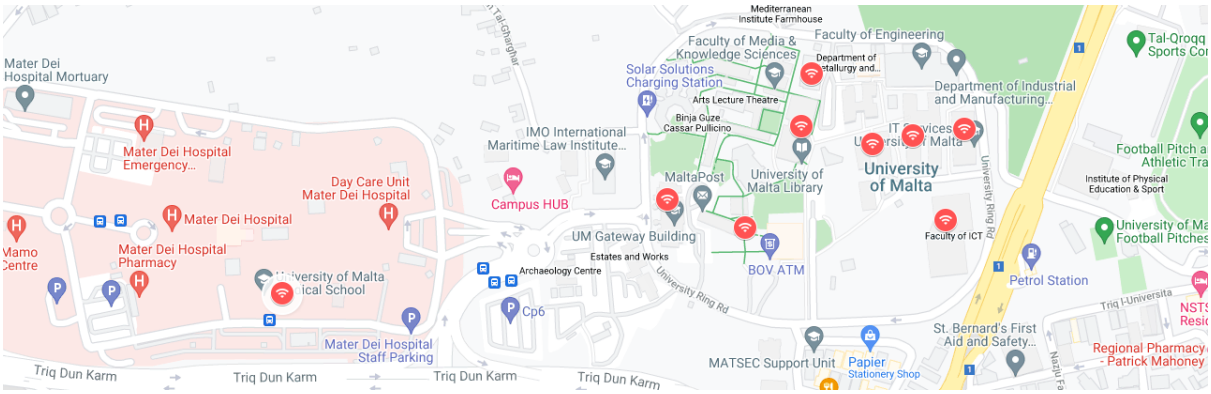

Figure 5.21 – LoRa gateway deployment locations

Similarly, Figure 5.21 shows the locations of 10 LoRa gateways deployed within the same campus. A series of comprehensive tests were conducted to optimise LoRa coverage across the campus, aiming to minimise packet loss and ensure reliable data transmission. Sensor nodes were strategically deployed in a variety of indoor environments to capture a broad and diverse air quality dataset. These include lecture rooms, staff offices, laboratories, study areas, kitchens, and corridors to ensure the usefulness of the data for comprehensive air quality analysis across different functional areas of the campus. Figure 5.22 shows examples of actual sensor nodes which were deployed in some of the rooms within the University campus.

Figure 5.22 – Examples of deployed sensor nodes within the University campus

Once the full large-scale network was deployed, LoRa metadata was collected over an extended period of time. The mean RSSI, mean SNR and mean PLR values collected from the deployed sensor nodes are presented numerically in Table 5.12 and depicted in Figure 5.23. Furthermore, the mean RSSI, mean SNR and mean PLR values across the whole

deployed WSN were calculated to be equivalent to -74 dBm, 5.6 dB and 3.4% respectively. This result shows that the large-scale deployment of the final WSN successfully mitigates the robustness weakness of the pure star topology by strategically deploying the multiple ensuring redundancy and maintaining a low mean PLR across the entire University campus.

Table 5.12 – University of Malta campus WSN measured mean RSSI, mean SNR and mean PLR

Building	Abbreviation	Mean RSSI (dBm)	Mean SNR (dB)	Mean PLR (%)
Administration	ADMB	-96.9	1.9	2.1
Biology	BSB	-93.8	2.3	6
Chemistry	CHM	-89.7	2.4	2
Gateway	GW	-77.3	6.7	3.5
ICT	ICT	-75.4	6.2	4
IT Services	IT	-83.7	5.3	2.1
Library	LBR	-71.6	5.6	2.2
Lecture Centre	LC	-67.6	8.4	3.4
Lecture Centre Theatre	LCT	-22.5	8.9	5.6
Mater Dei Dental	MDHDental	-61.6	8.7	3.3
Mean Values		**-74**	**5.6**	**3.4**

The best mean RSSI and mean SNR values are noted to be achieved in the LCT building. However, despite the favourable mean RSSI and mean SNR values, the mean PLR of the LCT building is the worst. This result seems to be somewhat odd and contradictory. Upon further investigation, the high mean PLR is attributed to a couple of sensor nodes at the edge of the building which were experiencing a significant number of packet losses. On the other hand, the high mean RSSI and mean SNR values are attributed to the architecture of the building. The building has a central corridor, lecture rooms on both sides and minimal obstructions between the deployed sensor nodes and the gateway leading to these optimal link quality metrics.

In contrast, the worst mean RSSI and mean SNR values are observed in the ADMB building. Despite these low link quality metric values, the measured mean PLR in the ADMB

building was equivalent to one of the lowest. This result is the complete opposite to the result achieved in the case of the LCT building. In the ADMB building the worst mean link quality metrics can be attributed to the fact that the ADMB building is sparse and L-shaped leading to multiple obstacles being in between the sensor nodes and the gateway. Nonetheless, despite the architecture of the building, all the sensor nodes were still in optimal range of the gateway leading to the low mean PLR.

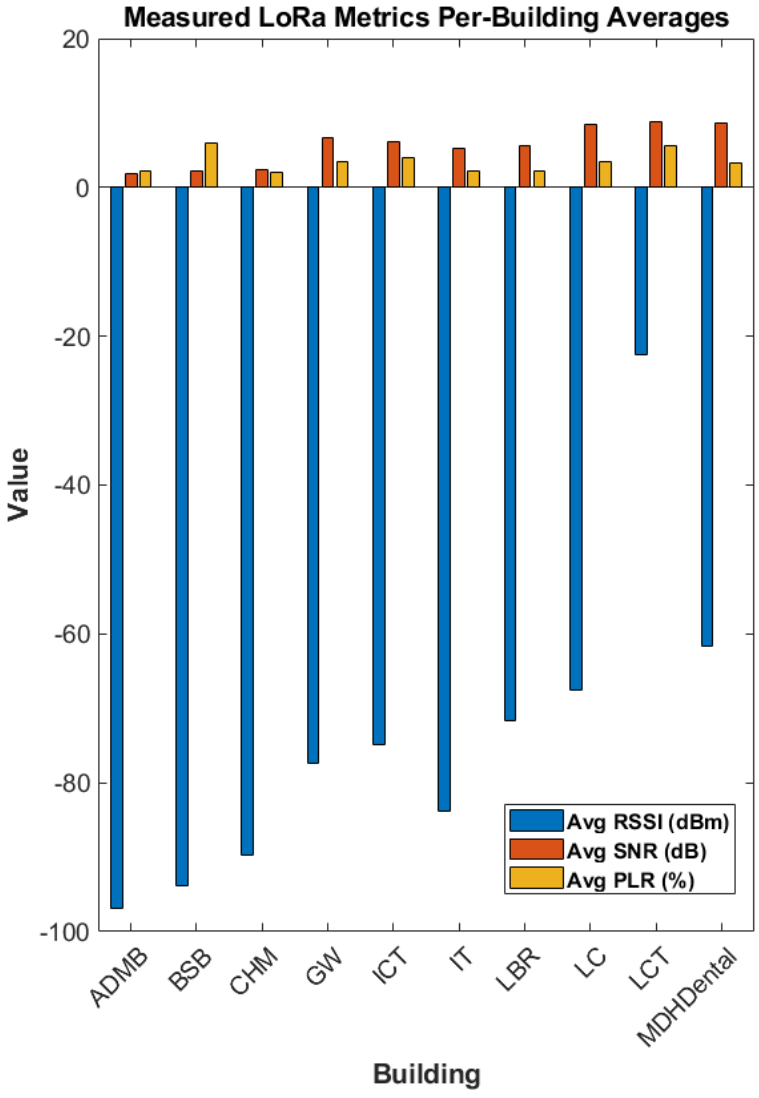

Figure 5.23 – University of Malta campus measured LoRa QoS metrics per building

Hence based on these two result, it may not sufficient to just observe the mean link quality metrics and mean PLR globally. A more optimal approach would be to analyse these results on a node by node basis and make adjustments accordingly. One of these proposed adjustments could be an adaptive data rate mechanism. In such a mechanism, the sensor nodes initially default to the lowest spreading factor of 7 and then adjusts this to a higher value if the number of packets lost is high. This will ensure that initially low power consumption is prioritised yet a low PLR is maintained. Another optimisation for PLR could be to enhance the error correcting mechanism by changing the CR and increasing the number of redundant bits. This will of course lead larger power consumption as the air time increases significantly. For example, going from a CR of 4/5 to a CR of 4/8 will double the airtime for the same payload length. Therefore, a delicate balance between power consumption and PLR needs to be ensured when employing such mechanisms.

Additionally, the proposed system is capable of generating metadata-driven analytical graphs and charts. One such example is the mean LoRa frequency usage per device, illustrated in Figure 5.24. Ideally, frequency usage should be evenly distributed among all sensor nodes to minimise channel congestion. However, the graph reveals a noticeable bias, with most nodes predominantly using the 868.1 MHz frequency band. This imbalance indicates that future optimisation is needed to ensure more uniform frequency distribution. This consideration is especially important when scaling the LoRa network to support a larger number of devices.

Additionally, the likely cause of this bias is the absence of specific code to override or randomise the channel selection process immediately after a sensor node wakes up. The LoRaWAN stack LMIC library defaults to the first mandatory channel, which is often 868.1 MHz and follows a predetermined static channel sequence. This repeated, non-randomised initialisation sequence on every device wake-up would result in the observed bias, as the device is forced to start its transmission attempt on the same preferred channel repeatedly.

The solution would involve modifying adding a new function to instruct the LMIC stack to select a channel randomly from the allowed frequency set before initiating transmission.

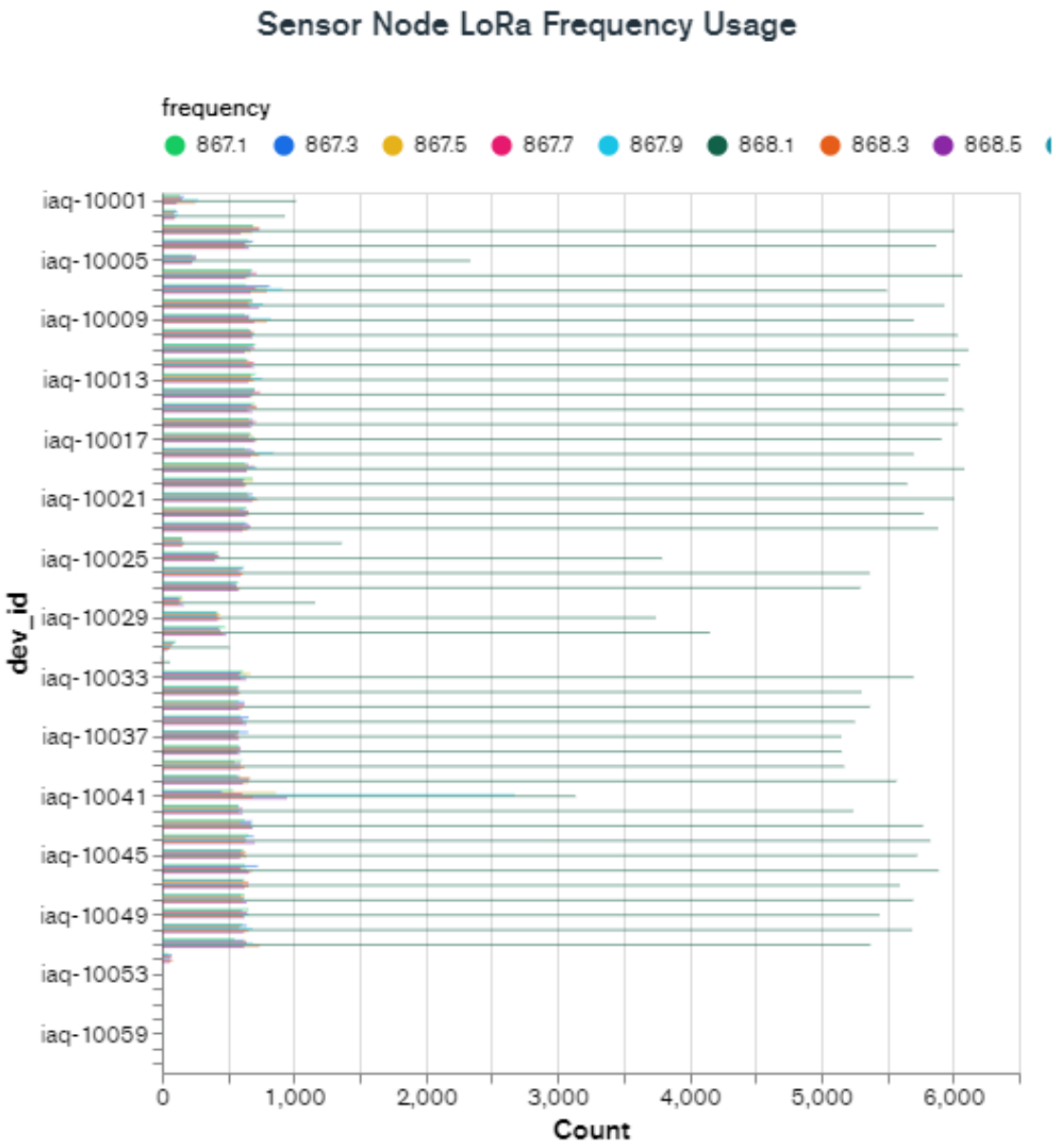

Figure 5.24 – Mean LoRa frequency usage per device graph

Additional device specific insights can also be derived through MongoDB Charts. A notable example is the monthly average battery voltage per device, as depicted in

Figure 5.25. This graph illustrates the gradual decline in battery voltage over time, enabling estimation of the battery lifespan for each device. It also serves as a diagnostic tool to trigger alerts if a device's battery voltage drops below the defined minimum discharge threshold. Moreover, steep voltage increases observed in the graph indicate instances where specific devices were recharged using the on-board charger from around 2.4V to a maximum of 4.2V.

In order to determine the battery life of the device an accelerated testing method was used. During this accelerated test the transmission interval was set to 15 minutes instead of 60 minutes such that the estimated battery life value is around four times more than the value measured during testing. A fully charged sensor node starts from around 4.2 V and drops linearly to 3.2 V over a 9-month period. The battery depletion rate then decreases logarithmically after that point to 2.4 V over a further 1-month period. Therefore, during the accelerated test, the battery life was measured to be equivalent to 10 months. This is equivalent to an estimated 40-month battery life when the interval is set to 60 minutes as intended. Additionally, this value matches the theoretically derived battery life value in Chapter 3.

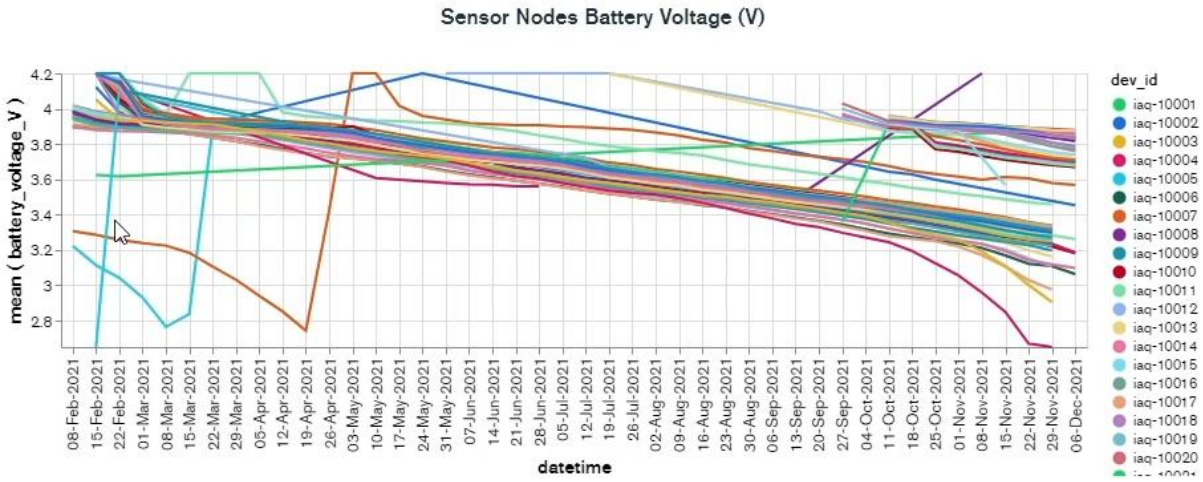

Figure 5.25 – Monthly mean battery voltage per device graph

5.3.2 – Air Quality Data Analysis

After confirming that the database was functioning correctly, various tools and services were employed to analyse the IoT data. One of the primary tools used for this purpose is MongoDB Charts. This service enables the creation of visualisations that display either raw or periodic average values of IAQ data. It also supports the application of filters to narrow down the data by specific time ranges or individual sensor nodes. As a result, charts can be generated to reflect daily, weekly, monthly, yearly, or custom time intervals, providing flexible and detailed insights into the captured data.

Figure 5.26 shows daily mean total volatile organic compounds data being collected by one of the nodes while Figure 5.27 shows weekly mean particulate matter data. The particulate matter peak shown in Figure 5.27 correlates to a blood rain occurrence which happened during that day. This graph is important as it gives a crucial insight into the functionality of the air filtration system of the building. This enables preventive action to be taken when such a weather phenomenon is expected. Such actions include the maintenance and replacement of the filters as well as ensuring that the filtration system is switched on effectively when required.

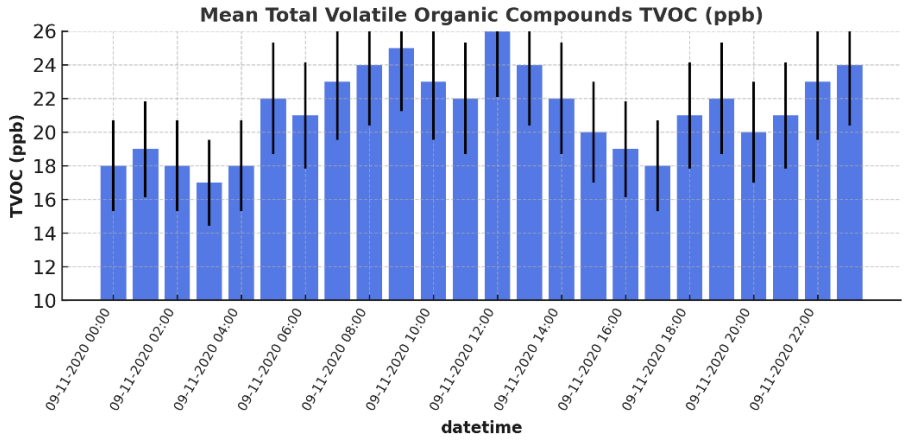

Figure 5.26 – Daily mean total volatile organic compounds graph

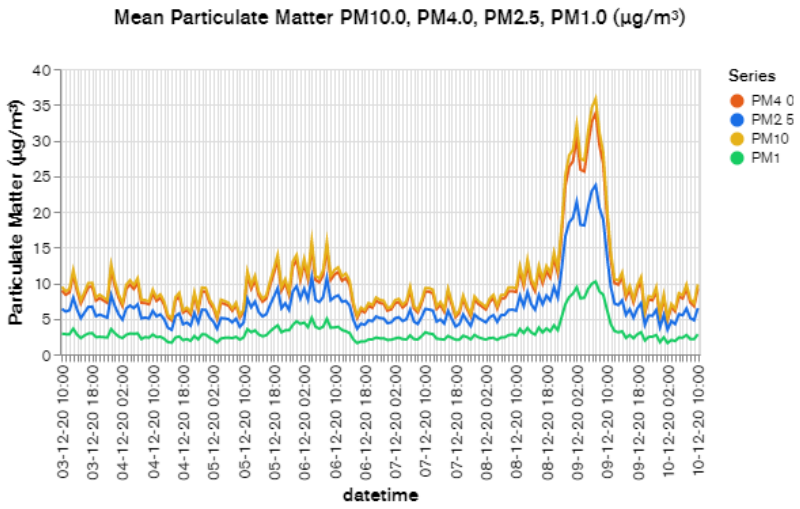

Figure 5.27 – Weekly mean particulate matter graph during blood rain event

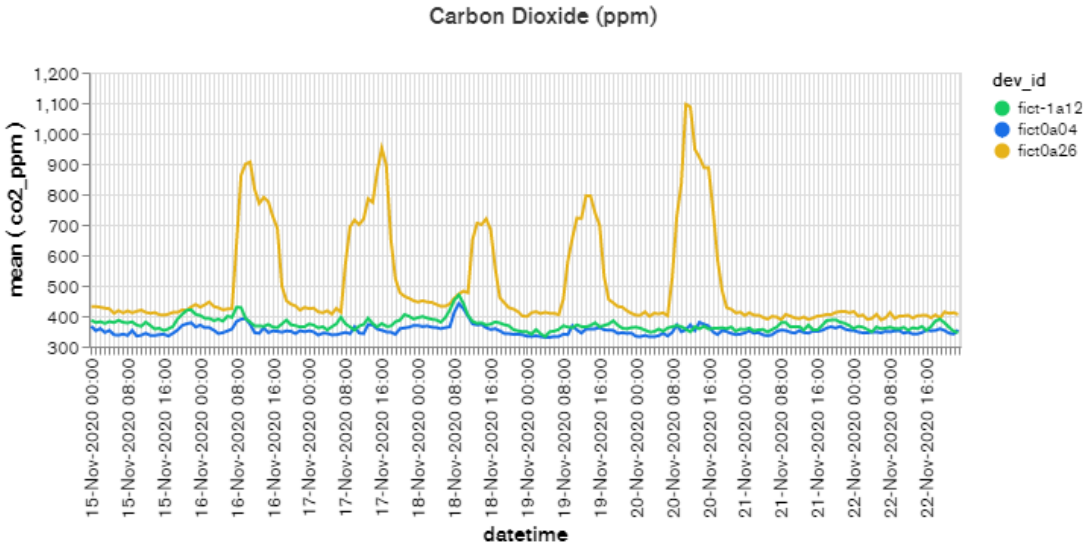

Figure 5.28 – Weekly mean carbon dioxide graph

In addition to displaying IAQ data from individual IoT nodes, the system can be configured to visualise data from multiple nodes simultaneously. Filters can be applied to include specific sensor nodes or group data by location, such as a particular floor level. For example, Figure 5.28 illustrates a weekly carbon dioxide trend for three distinct nodes, enabling the identification of room occupancy patterns throughout the week. The yellow signal indicates that the corresponding room is used consistently during office hours,

whereas the green and blue signals suggest minimal occupancy in those rooms during the same period. Notably, the 3rd and 4th peaks in the yellow signal are lower than the others, suggesting that fewer people were present in that room on those particular days. The 5th peak in particular shows that the carbon dioxide levels exceed the 1000 ppm mark leading to poor air quality. This is unhealthy over prolonged periods of time and can lead to symptoms like drowsiness and stuffiness suggesting the need of increased ventilation to improve air quality.

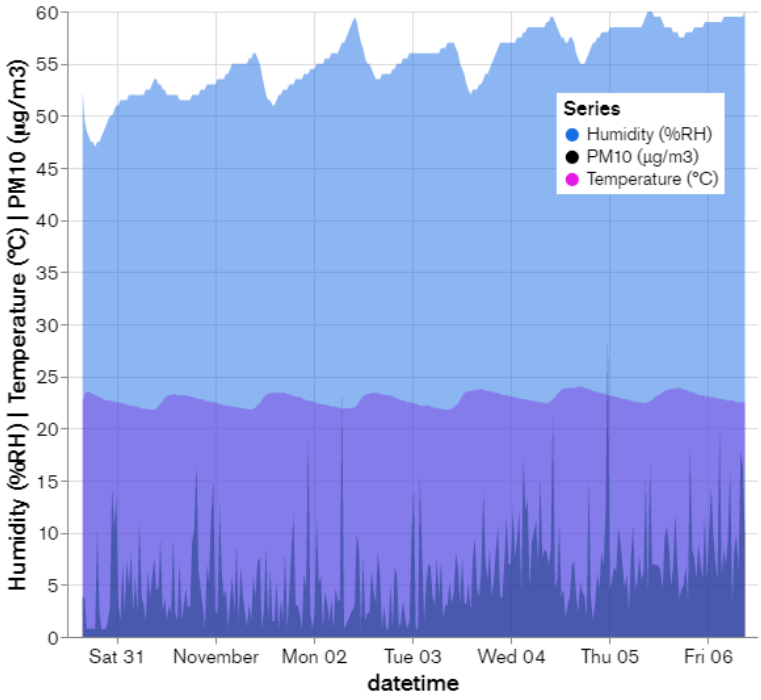

Figure 5.29 – Weekly mean PM10 in relation to temperature and humidity graph

Apart from visualising individual gases on a single graph, the proposed big data capture and analysis system supports the display of multiple gases and atmospheric parameters within one consolidated chart. This enables a more comprehensive analysis of how different gases interact with each other, as well as how they correlate with environmental conditions such as temperature and humidity. For instance, Figure 5.29 presents the mean weekly interaction of PM10 levels with fluctuations in temperature and humidity caused by the air conditioning and ventilation systems. Analysing such graphs

provides valuable insights into the effectiveness of air filtration and climate control systems in maintaining optimal indoor air quality. Particularly, this graph shows the temperature and humidity values in the room gradually falling to a minimum during the office hours when the cooling system is switched on. However, these values then increase at a faster pace during the night when the cooling system is switch off. Thus this graph is crucial to ensure both optimal air quality as well as ensuring energy costs for heating and cooling are kept to a minimum.

Another example graph, shown in Figure 5.30, presents the monthly mean gas concentrations recorded simultaneously by different gas sensors. This enables the analysis of cross-correlations between various gas measurements. For example, by examining the peak values recorded by the TB600B formaldehyde sensor alongside those from the CCS811 total volatile organic compound sensor, a clear correlation can be observed. Such correlations can help validate sensor readings, identify common sources of pollutants, and improve overall data reliability. Additionally, this result shows that these type of electro chemical sensors are highly susceptible to cross-correlation between different gases. Therefore, these types of sensors cannot be used to accurately monitor a particular gas. They can however be used as a general indication for the presence of a particular gas.

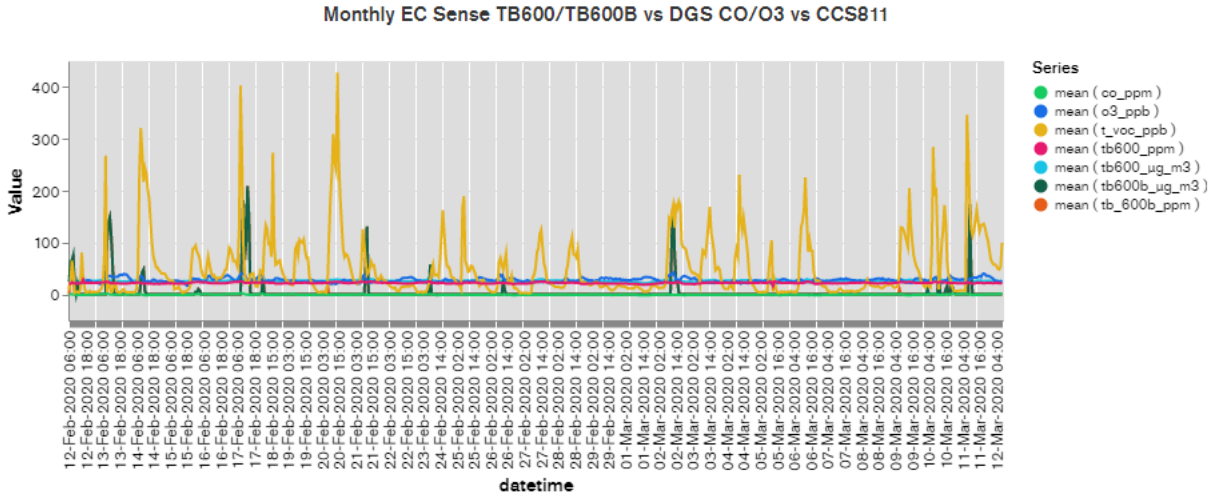

Figure 5.30 – Monthly mean multiple sensor comparison graph

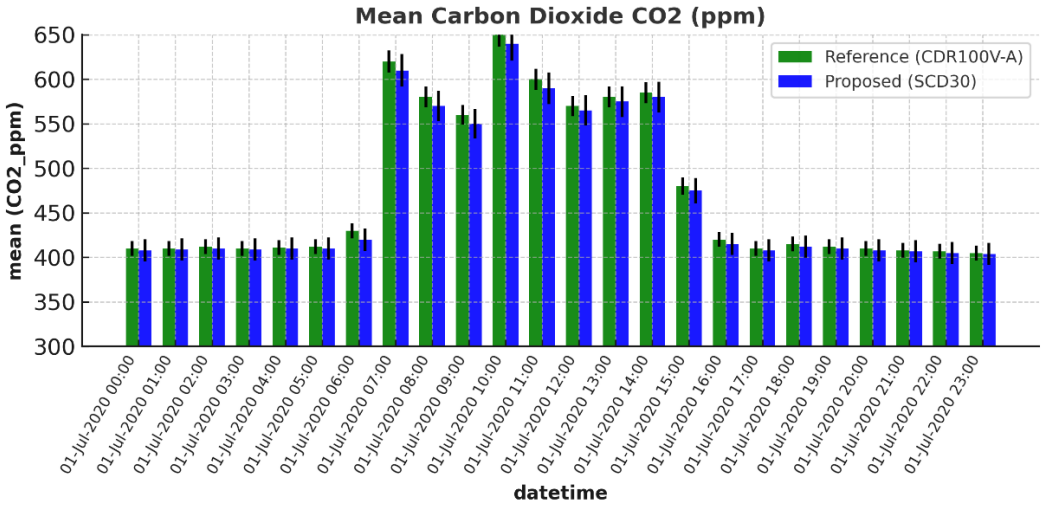

Figure 5.31 – Mean daily carbon dioxide data from SCD30 and CDR100VA

Furthermore, the proposed system facilitates the comparison of air quality data from the IoT wireless sensor nodes with that of higher precision reference instruments. For example, Figure 5.31 illustrates a comparison of mean daily carbon dioxide levels measured concurrently by the SCD30 sensor integrated in the proposed node and a higher accuracy, ±2%, CDR100VA reference sensor. Both sensors were placed in the same office environment to monitor ambient air under identical conditions. The data shows strong correlation between the two sensors, indicating that the proposed system achieves a high level of accuracy despite using low-cost sensing components. Additionally, apart from comparing the carbon dioxide sensors, efforts were made in order to compare, calibrate and validate the other air quality sensors with more accurate reference sensors. However due to the elevated cost of more accurate sensors and limited calibration equipment availability, these efforts proved to be unfruitful.

Moreover, this was not the main aim of this research which rather involved the design of innovative ultra-low-power, modular, and scalable IoT sensor node for widespread deployment. Hence this design inherently used low-cost sensors that are highly

effective for relative air quality monitoring but typically exhibit greater unit-to-unit variability and long-term drift compared to expensive, high-accuracy reference instruments. Consequently, the dissertation focused on validating the core functionality of the sensor node in terms of low-power performance and the ability to collect comprehensive, correlative data across a large-scale network rather than on absolute calibration. Therefore, comprehensive long-term calibration was intentionally reserved as a critical next step and absolute and relative calibration strategies are discussed in the future work section.

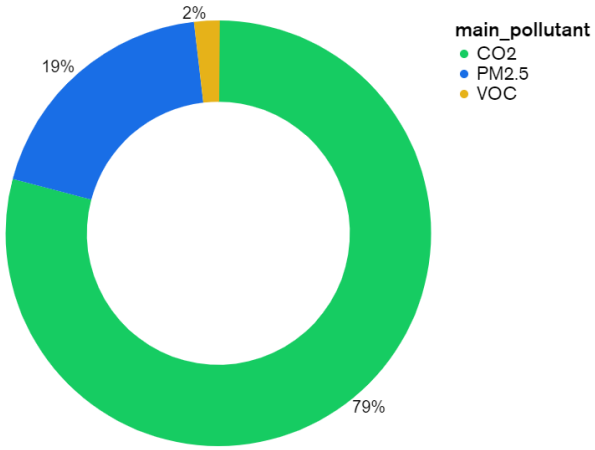

Figure 5.32 – Weekly period main pollutant chart

Another useful time based data analysis chart generated by the system is the main pollutant chart, illustrated in Figure 5.32. This chart highlights the dominant pollutant detected in a particular room throughout a given week. By identifying which pollutants are most prevalent over time, this analysis supports the implementation of targeted preventative actions. For instance, it can help pinpoint specific sections of the ventilation system where particulate filters may require replacement, thus contributing to more effective maintenance and improved indoor air quality management. In this case the graph shows us that carbon dioxide, which originates from occupant within the building, is the most prevailing pollutant. This therefore highlights the need of increased ventilation within the building to ensure carbon dioxide levels are managed to be within the healthy value ranges define previously.

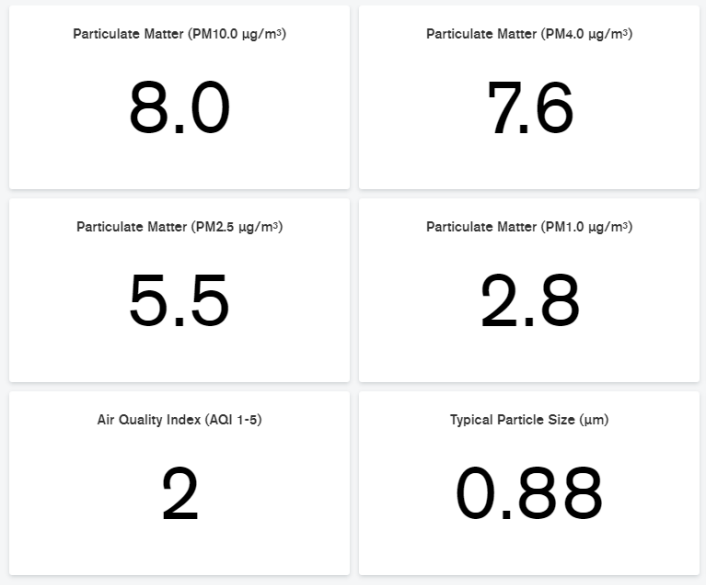

Figure 5.33 – Air quality values chart

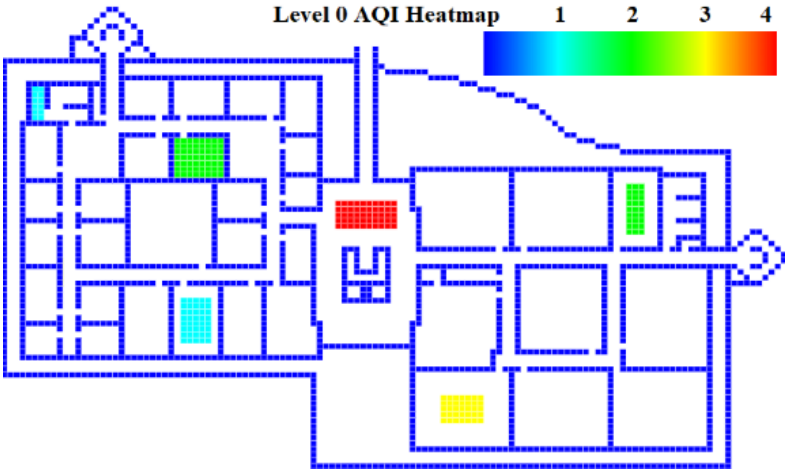

Figure 5.34 – Level 0 live air quality index heatmap

In addition to generating time-based air quality charts, the proposed system also supports real-time IAQ data visualisation. One example of this is the live air quality value chart shown in Figure 5.33, which displays the most recent IAQ readings from a specific IoT sensor node. Another valuable real-time visualisation is the AQI heatmap depicted in Figure 5.34. This heatmap provides spatially contextualised AQI data by mapping air quality levels to the physical locations of sensor nodes within the building. These live charts not

only enhance immediate situational awareness but also enable seamless data extraction for training deep learning models aimed at autonomously managing the ventilation system based on real-time AQI levels. The chart also shows that worst air quality levels are noted to be in the lobby of the building. This location coincides with the entry way of the building and thus this result highlights the need of a better ventilation system such the installation of an air curtain to prevent outside pollutants from entering through the doors.

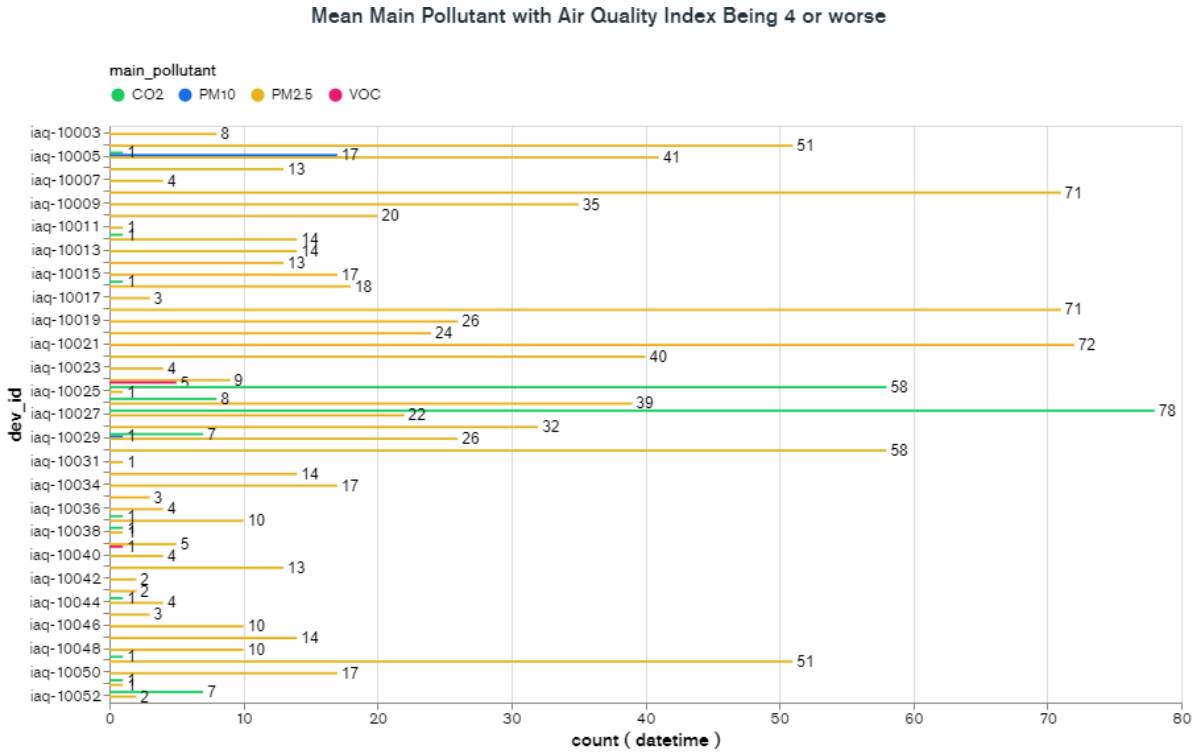

Figure 5.35 – Poor mean air quality index counter chart

In addition to these visualisations, the AQI can also be used to create more analytical and insightful charts. One such example is shown in Figure 5.35, which displays a poor mean air counter for each IoT sensor node indicating how many times the AQI has reached a level of 4 or higher. Each instance is colour coded based on the specific pollutant responsible for the elevated AQI value. This visualisation helps pinpoint recurring air quality issues in specific areas and identifies which pollutants are most problematic, thereby supporting targeted mitigation strategies.

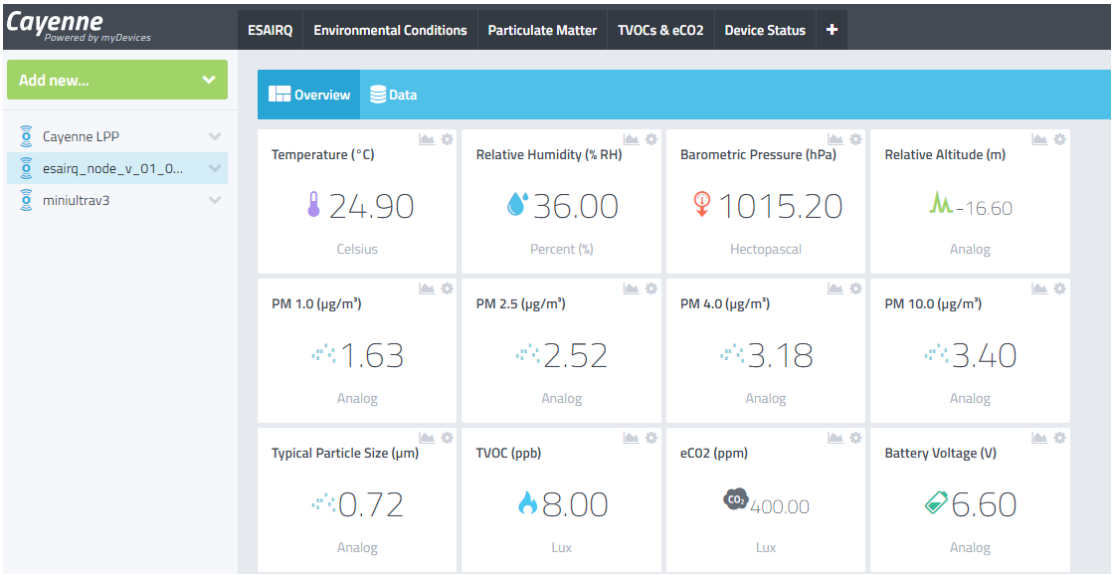

Figure 5.36 – Live data visualisation on the myDevices web platform

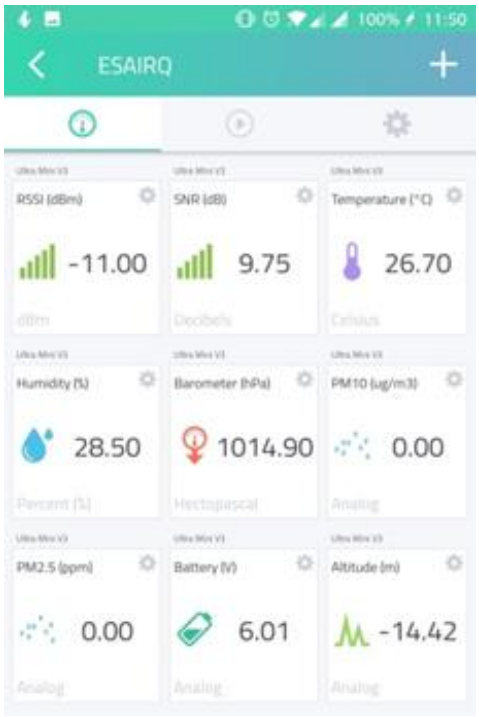

Figure 5.37 – Live data visualisation in myDevices mobile application

Another data analysis platform used in conjunction with MongoDB Charts is myDevices. This tool enables the development of simplified and user-friendly data

dashboards, as illustrated in Figure 5.36. By incorporating distinct icons and well-formatted data displays, the dashboards make interpreting air quality data more intuitive for users. In addition to its web-based interface, myDevices also supports the creation of a smartphone application, shown in Figure 5.37. This mobile app increases accessibility to real-time air quality data, thereby improving overall usability and facilitating on-the-go monitoring.

Figure 5.38 – Alert trigger for high total volatile organic compounds level

An additional key feature offered by the myDevices platform is the ability to configure alert triggers. These triggers can be set to notify users via email or smartphone notifications when specific gas concentration thresholds or air quality limits are exceeded. Beyond just alerts, these triggers can also be integrated into automated systems to initiate actions, such as activating ventilation systems or increasing airflow rates and hence enabling responsive and intelligent environmental control based on real-time sensor data. Figure 5.38 for example shows a trigger which was set to alert the user of high total volatile organic compound gas values.

Furthermore, Figure 5.39 shows three alarms which were received via email when the carbon dioxide reading exceeded the set thresholds in one of the lecture rooms at the Lecture Centre building. In addition to providing information about the carbon dioxide concentration that triggered the alert, the alarm system also identifies the specific device responsible for the notification, along with its location, room number, and room type. This contextual information enhances traceability and facilitates targeted interventions. Furthermore, the timestamp included in the email alerts helps pinpoint problematic time periods enabling more effective scheduling of ventilation or occupancy adjustments.

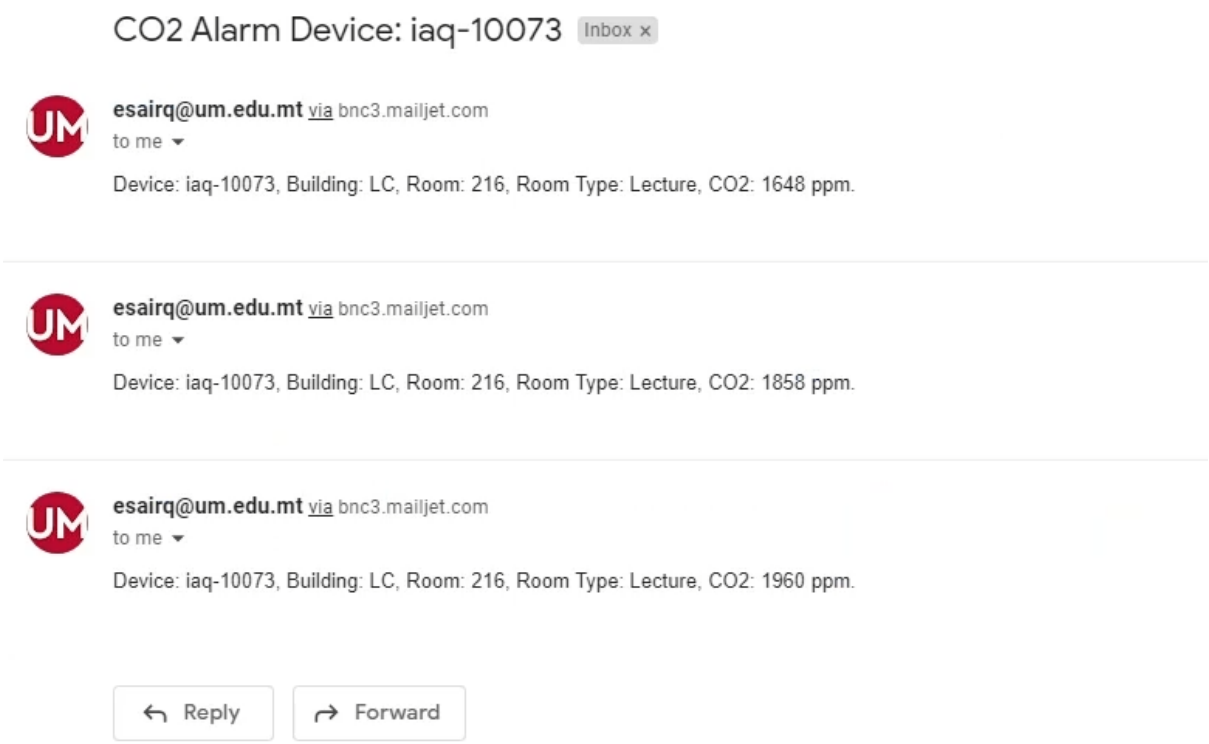

Figure 5.39 – Alarm received when exceeding the carbon dioxide threshold in one of the lecture rooms

5.3.3 – Novelty and Innovation

A distinctive feature of the proposed big data capture and analysis system is its affordability. This is made possible through the development of inexpensive sensor nodes and the integration of free, open-source software components. The cost-efficiency of the system supports scalability, allowing for broad, large-scale deployment. Such extensive deployment facilitates the generation of rich, location-based data which is often difficult to accomplish, as most SOA-related projects typically limit themselves to deploying only a few nodes for proof-of-concept purposes.

Another noteworthy innovation is the validation of the large-scale deployed network using a custom developed theoretical simulation model. In particular, the LoRa

metadata collected from the large-scale WSN deployment was compared with simulated data generated specifically for the indoor LoRa application. The alignment between the simulated and measured data not only confirmed the accuracy of the theoretical model but also offered valuable insights into which propagation models are more effective for representing indoor LoRa network behaviour.

One more innovative aspect of this work is the creation of a data forwarding server that bridges the LoRaWAN server and the MongoDB database. This server retrieves air quality data from the LoRaWAN server through MQTT, processes and formats the data, and then stores it in a document-oriented database. Prior to storage, it enriches the data by calculating an air quality index, identifying the primary pollutant contributing to that index, and determining a thermal comfort index.

A final innovation of this work is the comprehensive set of data analysis graphs and visualisations created using MongoDB Charts. A standout example is the air quality index heatmap, which delivers location specific air quality insights. This heatmap was produced by applying a coordinate system to map the entire building, enabling spatial visualisation of air quality data across different areas.

Chapter 6 – Conclusion and Future Work

6.1 – Introduction

This section presents a summary of the research work carried out whilst highlighting the novelty achieved. Future work related to the development of the wireless sensor node and big data capture and analysis system is also presented.

6.2 – Future Work

The future work section can be split into two fundamental tasks: enhancements to the low power and low-cost battery powered air quality IoT wireless sensor node and advancements for the low-cost LoRa-based big data capture and analysis system.

6.2.1 - Battery Powered Air Quality IoT Wireless Sensor Node

While this research successfully developed an ultra-low-power sensor node, comprehensive and long-term calibration was intentionally reserved as a critical next step. The primary focus of this dissertation was on innovating the core functionality of the sensor node in terms of ultra-low-power performance, modularity, and the ability to collect comprehensive data across a large-scale network, rather than on absolute metrological accuracy. This design inherently used low-cost sensors that are highly effective for relative IAQ monitoring but are known to exhibit greater variability and long-term drift compared to expensive reference instruments. The elevated cost and limited availability of high-accuracy reference sensors and calibration equipment made extensive validation impractical within the scope of this work. Future work will directly address this by focusing on data integrity and sensor reliability. The planned enhancements include the following six points:

- Implement comprehensive calibration by conducting comparative studies through co-location of the sensor nodes with high-accuracy reference

instruments to validate performance and quantify potential error sources. The empirical data collected will be used to develop robust correction models that compensate for sensor inaccuracies, aging, and drift over time.

- Develop a detailed error budget to formally quantify and allocate all potential error sources and then leverage the high density of the WSN to develop algorithms for network-based calibration. This approach will involve using data from multiple neighbouring nodes to statistically identify and correct for drift in a single sensor, creating a self-calibrating and more resilient network.

- Enhance on-device intelligence by exploring the implementation of sensor multiplicity to support self-diagnostics, provide redundancy, enable cross-sensor event correlation, and facilitate on-device calibration, thereby improving system reliability and data quality.

- Further optimise power management through the investigation and the integration of additional power-saving techniques. These could potentially include techniques such as dynamic voltage scaling and dynamic frequency scaling, to work alongside the existing DPM circuitry to further minimise overall power consumption.

- Integrate next-generation sensing technology by incorporating newly released, more energy-efficient air quality sensors to enhance the sensing capabilities of the node. This aims to improve measurement accuracy while simultaneously reducing power consumption.

- Reduce device form factor by redesigning the PCB and enclosure to significantly reduce the overall physical size of the fabricated device, making it less obtrusive and easier to deploy in a wider range of indoor environments.

6.2.2 - LoRa-Based Big Data Capture and Analysis System

Future work for the big data system will focus on leveraging the collected data and expanding the smart capabilities of the system. The following five objectives were identified:

- Expand the data collection and network analysis by continuing the gathering and analysing large volumes of air quality big data, LoRa metadata, and network performance metrics from the deployed WSN to build a more robust dataset.

- Optimise the performance of the network by fine tuning LoRa parameters such as SF, bandwidth settings, and transmission power to further improve network performance, balancing reliability with energy consumption. Investigate advanced techniques like adaptive data rates and alternative channel access methods to enhance efficiency and security.

- Utilise the collected big data to train, validate, and deploy machine learning models. This will enhance system intelligence for applications such predictive environmental control to intelligently and proactively manage the BMS, anomaly detection to identify unusual pollution events or potential sensor malfunctions and predictive maintenance to forecast sensor failure or calibration needs based on performance degradation over time.

- Integrate additional smart platform APIs such as If This Then That (IFTTT), to extend the smart capabilities and improve overall usability of the WSN. This also enables more flexible and automated interactions with a wide range of third-party services and platforms.

- Leverage the modular and scalable design of the sensor node and network architecture to extend its application beyond IAQ. The system can serve as a flexible platform for other smart building functions, such as energy consumption monitoring, occupancy sensing, and lighting control, creating an integrated environmental monitoring ecosystem.

6.3 – Conclusion

This research successfully addressed critical gaps in IAQ monitoring by designing, developing, and validating an innovative, low-cost, and ultra-low-power monitoring system capable of large-scale deployment and comprehensive data analysis. Through an iterative design process culminating in four distinct prototypes, this work systematically achieved the core aims and objectives outlined in Chapter 1, establishing a new benchmark for IAQ monitoring technology.

The project met all ten of its specific objectives. For the sensor node, an innovative, low-cost wireless device was implemented that exceeded the performance of SOA alternatives. It incorporated a comprehensive suite of sensors for temperature, humidity, pressure, carbon dioxide, volatile organic compounds, and particulate matter. A sophisticated DPM strategy was engineered and optimised across four prototypes, dramatically reducing power consumption and achieving a projected operational lifespan of 40 months, far exceeding the initial 16-month target. The final prototype has a modular architecture, featuring adaptable digital and analogue interfaces, ensuring the device is future-proof and expandable for new sensing applications.

For the big data system, a cost-effective LoRa-based architecture capable of supporting widespread deployment was developed. A key achievement was the creation and validation of a theoretical simulation framework to predict LoRa link quality and scalability in a dense indoor setting, which was subsequently validated against empirical data from a large-scale WSN deployment. Furthermore, a robust data forwarding server was implemented to process incoming data, calculate the AQI and TCI, and store the enriched information efficiently. Finally, a comprehensive suite of data visualisations, including a novel location-specific AQI heatmap, was developed to provide intuitive, real-time IAQ insights to end-users.

The primary innovation of this dissertation is the establishment of a new SOA benchmark for ultra-low-power IAQ technology. The final prototype achieves a sleep mode current of just 270 nA and an average hourly energy consumption of 327 µAh, resulting in a projected 40-month battery life on a 10,500 mAh battery. This represents a significant advancement in energy efficiency. The energy efficiency gains relative to existing devices are substantial. Compared to leading academic research, the sleep current of this prototype is over 37 times lower than the 10 µA achieved in comparable SOA devices. This ultra-low-power performance translates to a battery life that is over 3.6 times longer than the best-performing academic node. Moreover, the proposed system offers a more comprehensive range of sensing capabilities, including both volatile organic compounds and multi-size particulate matter detection, which are often absent in other systems. Against commercial devices, the gains are equally impressive. The projected 40-month lifespan is 2.5 times longer than that of the market-leading Airthings Wave Plus.

A second major contribution is the development and validation of a scalable, cost-effective LoRa-based big data solution tailored for high-density IAQ monitoring. This work is among the first to deploy and analyse such a large-scale network in a campus environment, providing valuable empirical data that validates a custom theoretical propagation model for indoor LoRa performance. The novel data forwarding server, which

computes AQI and TCI calculations, and includes advanced spatial visualisations like the AQI heatmap, provide a complete framework that transforms raw sensor readings into actionable intelligence for smarter building management.

In summary, this research delivers a holistic and validated solution that pushes the boundaries of low-power IoT design and large-scale environmental sensing. It provides not only a new generation of hardware but also a complete data architecture, accelerating the adoption of high-density sensor networks for creating healthier and more energy efficient indoor environments.

.

Bibliography

[1] S. Bhattacharya, S. Sridevi and R. Pitchiah, "Indoor air quality monitoring using wireless sensor network," in *2012 Sixth International Conference on Sensing Technology (ICST)*, Kolkata, 2012, pp. 422-427.

[2] P. Breitegger and A. Bergmann, "Air quality and health effects - How can wireless sensor networks contribute? A critical review," in *2016 International Conference on Broadband Communications for Next Generation Networks and Multimedia Applications (CoBCom)*, Graz, 2016, pp. 1-8.

[3] D. M. G. Preethichandra, "Design of a smart indoor air quality monitoring wireless sensor network for assisted living," in *2013 IEEE International Instrumentation and Measurement Technology Conference (I2MTC)*, Minneapolis, MN, 2013, pp. 1306-1310.

[4] H. Chojer, P. Branco, F. Martins, M. Alvim-Ferraz and S. Sousa, “Development of low-cost indoor air quality monitoring devices: Recent advancements,” *Science of The Total Environment*, vol. 727, pp.138385, 2020.

[5] H. Jafari, Xiangfang Li, L. Qian and Y. Chen, "Community based sensing: A test bed for environment air quality monitoring using smartphone paired sensors," in *2015 36th IEEE Sarnoff Symposium*, Newark, NJ, 2015, pp. 12-17.

[6] D. K. Gupta, "A review on wireless sensor networks," *Network and Complex Systems*, vol. 3, no. 1, 2013, pp. 18–23.

[7] I. F. Akyildiz, Weilian Su, Y. Sankarasubramaniam and E. Cayirci, "A survey on sensor networks," in *IEEE Communications Magazine*, vol. 40, no. 8, pp. 102-114, Aug. 2002.

[8] I. F. Akyildiz and Xudong Wang, "A survey on wireless mesh networks," *IEEE Communications Magazine*, vol. 43, no. 9, pp. S23-S30, Sept. 2005.

[9] D. Gupta, "Wireless Sensor Networks ‘Future trends and Latest Research Challenges’," *IOSR Journal of Electronics and Communication Engineering (IOSR-JECE)*, vol. 10, no. 2, 2015, pp. 41-46.

[10] S. Sharma, R. K. Bansal and S. Bansal, "Issues and Challenges in Wireless Sensor Networks," in *2013 International Conference on Machine Intelligence and Research Advancement*, Katra, 2013, pp. 58-62.

[11] C. S. Kingsly and J. G. C. Chandran, "Critical Study on Constraints in Wireless Sensor Network Applications," *International Journal of Engineering and Research Technology (IJERT)*, vol. 2, no. 7, 2013, pp.1311-1216.

[12] K. Romer and F. Mattern, "The design space of wireless sensor networks," *IEEE Wireless Communications*, vol. 11, no. 6, pp. 54-61, Dec. 2004.

[13] S. Zhang and H. Zhang, "A review of wireless sensor networks and its applications," in *2012 IEEE International Conference on Automation and Logistics*, Zhengzhou, 2012, pp. 386-389.

[14] G. Simon, A. Ledezczi, and M. Maroti, “Sensor Network-Based Countersniper System,” in *Proc. SenSys*, Baltimore, MD, Nov. 2004.

[15] K. Pister, "The 29 palms experiment - tracking vehicles with a UAV-delivered sensor network," [Online]. Available: http://robotics.eecs.berkeley.edu/~pister/29Palms0103. [Accessed 10 10 2020].

[16] W. M. Merrill, F. Newberg, K. Sohrabi, W. Kaiser and G. Pottie, "Collaborative networking requirements for unattended ground sensor systems," in *2003 IEEE Aerospace Conference Proceedings (Cat. No.03TH8652)*, Big Sky, MT, USA, 2003, pp. 5_2153-5_2165.

[17] Yun-Liang He, Shu-Qin Geng, Xiao-Hong Peng, Li-Gang Hou, Xiang-Kai Gao and Jin-Hui Wang, "Design of outdoor air quality monitoring system based on ZigBee wireless sensor network," in *2016 13th IEEE International Conference on Solid-State and Integrated Circuit Technology (ICSICT)*, Hangzhou, 2016, pp. 368-370.

[18] G. Zhou, L. Huang, Z. Zhu, W. Li and G. Shen, "A Zoning Strategy for Uniform Deployed Chain-Type Wireless Sensor Network in Underground Coal Mine Tunnel," in *2013 IEEE 10th International Conference on High Performance Computing and Communications & 2013 IEEE International Conference on Embedded and Ubiquitous Computing*, Zhangjiajie, 2013, pp. 1135-1138.

[19] Y. Liu, Y. Gu, G. Chen, Y. Ji and J. Li, "A Novel Accurate Forest Fire Detection System Using Wireless Sensor Networks," in *2011 Seventh International Conference on Mobile Ad-hoc and Sensor Networks*, Beijing, 2011, pp. 52-59.

[20] Argo, "Global Ocean Sensor Network," [Online]. Available: http://www.argo.ucsd.edu. [Accessed 10 10 2020].

[21] K. Martinez, R. Ong, J. K. Hart and J. Stefanov, "GLACSWEB: A Sensor Web for Glaciers," in *Proc. of European Workshop on Wireless Sensor Networks*, Berlin, Germany, pp. 46–49, 2004.

[22] P. Juang, H. Oki, Y. Wang, M. Martonosi, L.S. Peh, and D. Rubenstein, "Energy efficient computing for wildlife tracking: Design tradeoffs and early experiences with ZebraNet,'' *Architectural Support for Programming Languages and Operating Systems (ASPLOS)*, pp. 96–107, 2002.

[23] H. Baldus, K. Klabunde, and G. Müsch, "Reliable set-up of medical body-sensor networks," in *Wireless Sensor Networks*, Berlin/Heidelberg, Germany: Springer-Verlag, 2004, vol.2920, pp. 353–363.

[24] L. Mo, S. Liu, R. X. Gao, D. John, J. W. Staudenmayer and P. S. Freedson, "Wireless Design of a Multisensor System for Physical Activity Monitoring," *IEEE Transactions on Biomedical Engineering*, vol. 59, no. 11, pp. 3230-3237, Nov. 2012.

[25] R. Fensli, E. Gunnarson, and O. Hejlesen, "A wireless ECG system for continuous event recording and communication to a clinical alarm station," in *International Conference of IEEE Engineering in Medicine and Biology Society (IEMBS)*, vol. 1, 2004, pp. 2208-2211.

[26] A. Gaddam, S. C. Mukhopadhyay and G. S. Gupta, "Elder Care Based on Cognitive Sensor Network," *IEEE Sensors Journal*, vol. 11, no. 3, pp. 574-581, March 2011.

[27] F. Michahelles, P. Matter, A. Schmidt and B. Schiele, "Applying Wearable Sensors to Avalanche Rescue: First Experiences with a Novel Avalanche Beacon," *Computers & Graphics*, vol. 27, no. 6, 2003, pp. 839-847.

[28] Z. Butler, P. Corke, R. Peterson and D. Rus, "Virtual fences for controlling cows," in *IEEE International Conference on Robotics and Automation, 2004. Proceedings ICRA '04*, 2004, New Orleans, LA, USA, vol. 5, 2004, pp. 4429-4436.

[29] D.Moshou, C.Bravo and R.Oberti, "Plant disease detection based on data fusion of hyper-spectral and multi spectral fluorescence imaging using Kohonen maps", *Real time Imaging, Elsevier*, vol. 11, no. 2, 2005, pp. 75-83.

[30] R. Hussain, J. L. Sahgal, P.Mishra and B. Sharma, "Application of WSN in Rural Development, Agriculture Water Management," *International Journal of Soft Computing and Engineering (IJSCE)*, vol. 2, no. 5, 2012, pp. 68-72.

[31] R. Beckwith, D. Teibel, and P. Bowen, “Pervasive computing and proactive agriculture,” in *Proc. of the 2nd International Conference of Pervasive Computing*, Vienna, Austria, April 2004.

[32] R. Riem-Vis, "Cold Chain Management using an Ultra Low Power Wireless Sensor Network," in *Proc. of the 2nd international conference on Embedded networked sensor systems*, WAMES ’04, 2004.

[33] C. Kappler and G. Riegel, “A Real-World, Simple Wireless Sensor Network for Monitoring Electrical Energy Consumption,” in *Proc. of Wireless Sensor Networks, First European Workshop EWSN 2004*, Berlin, Germany, pp.339-352, Jan. 2004.

[34] A. Tiwari, F. L. Lewis and S. S. Ge, "Wireless sensor network for machine condition based maintenance," in *ICARCV 2004 8th Control, Automation, Robotics and Vision Conference*, Kunming, China, vol.1, 2004, pp. 461-467.

[35] N. K. Suryadevara, S. C. Mukhopadhyay, S. D. T. Kelly and S. P. S. Gill, "WSN-Based Smart Sensors and Actuator for Power Management in Intelligent Buildings," *IEEE/ASME Transactions on Mechatronics*, vol. 20, no. 2, pp. 564-571, April 2015.

[36] S. M. A. El-Kader, B. M. M. El-Basioni and M. A. Fakhreldin, "Smart home design using wireless sensor network and biometric technologies," *International Journal of Application or Innovation in Engineering & Management (IJAIEM)*, vol. 2, no. 3, 2013, pp. 413-429.

[37] S. Idwan, J. A. Zubairi and I. Mahmood, "Smart Solutions for Smart Cities: Using Wireless Sensor Network for Smart Dumpster Management," in *2016 International Conference on Collaboration Technologies and Systems (CTS)*, Orlando, FL, 2016, pp. 493-497.

[38] A. Ayadi, O. Ghorbel, A. Obeid, M. S. Bensaleh and M. Abid, "Leak detection in water pipeline by means of pressure measurements for WSN," in *2017 International Conference on Advanced Technologies for Signal and Image Processing (ATSIP)*, Fez, 2017, pp. 1-6.

[39] J. Chinrungrueng, U. Sununtachaikul and S. Triamlumlerd, "A Vehicular Monitoring System with Power-Efficient Wireless Sensor Networks," in *2006 6th International Conference on ITS Telecommunications*, Chengdu, 2006, pp. 951-954.

[40] S. R. J. Ramson and D. J. Moni, "Applications of wireless sensor networks — A survey," in *2017 International Conference on Innovations in Electrical, Electronics, Instrumentation and Media Technology (ICEEIMT)*, Coimbatore, 2017, pp. 325-329.

[41] W. R. Heinzelman, A. Chandrakasan, and H. Balakrishnan, "Energy-Efficient Communication Protocol for Wireless Microsensor Networks," in *Proc. 33rd Annu. Hawaii International Conference on System Sciences*, Jan. 2000, pp. 10.

[42] M. Jacob and R. Krishnamurthy, "Infrared Communication for Wireless Sensor Networks," *IEEE Sensors Journal*, vol. 8, no. 10, pp. 1423–1429, Oct. 2008.

[43] Z. Ghassemlooy, W. Popoola, and S. Rajbhandari, *Optical Wireless Communications: System and Channel Modelling with MATLAB®*, 2nd ed. CRC Press, 2019.

[44] M. Stojanovic, "Underwater Acoustic Communications: Design Considerations on the Physical Layer," in *Proc. 5th Annu. Conference on Wireless on Demand Network Systems and Services*, Jan. 2008, pp. 1–10.

[45] A. Kurs, A. Karalis, R. Moffatt, J. D. Joannopoulos, P. Fisher, and M. Soljačić, "Wireless Power Transfer via Strongly Coupled Magnetic Resonances," *Science*, vol. 317, no. 5834, pp. 83–86, July 2007.

[46] P. F. Jose Cecilio, “Wireless Sensor Network: Conepts and Components,” in *Wireless Sensors in Heterogeneous Networked Systems*, Coimbra, Springer International Publishing, 2014.

[47] W. R. Heinzelman, A. Chandrakasan, and H. Balakrishnan, "Energy-Efficient Communication Protocol for Wireless Microsensor Networks," in *Proc. 33rd Annu. Hawaii International Conference on System Sciences*, Jan. 2000, pp. 10.

[48] S. Lindsey and C. S. Raghavendra, "PEGASIS: Power-Efficient Gathering in Sensor Information Systems," in *Proc. IEEE Aerospace Conference*, vol. 3, 2002, pp. 1125–1130.

[49] J. N. Al-Karaki and A. E. Kamal, "Routing Techniques in Wireless Sensor Networks: A Survey," *IEEE Wireless Communications*, vol. 11, no. 6, pp. 6–28, Dec. 2004.

[50] I. F. Akyildiz, W. Su, Y. Sankarasubramaniam, and E. Cayirci, "Wireless sensor networks: a survey," *Computer Networks*, vol. 38, no. 4, pp. 393–422, 2002.

[51] P. Chhimwal, D. S. Rai, and D. Rawat, "Comparison between different wireless sensor simulation tools," *IOSR Journal of Electronics and Communication Engineering (IOSR- JECE)*, vol. 5, no. 2, 2013, pp. 54-60.

[52] K. J. Singh and D. S. Kapoor, "Create Your Own Internet of Things: A survey of IoT platforms.," *IEEE Consumer Electronics Magazine*, vol. 6, no. 2, pp. 57-68, April 2017.

[53] H. Hejazi, H. Rajab, T. Cinkler and L. Lengyel, "Survey of platforms for massive IoT," in *2018 IEEE International Conference on Future IoT Technologies (Future IoT)*, Eger, 2018, pp. 1-8.

[54] U. Noreen, A. Bounceur and L. Clavier, "A study of LoRa low power and wide area network technology," in *2017 International Conference on Advanced Technologies for Signal and Image Processing (ATSIP)*, Fez, 2017, pp. 1-6.

[55] U. Raza, P. Kulkarni and M. Sooriyabandara, "Low Power Wide Area Networks: An Overview," *IEEE Communications Surveys & Tutorials*, vol. 19, no. 2, pp. 855-873, 2017.

[56] M. Collotta, G. Pau, T. Talty and O. K. Tonguz, "Bluetooth 5: A Concrete Step Forward toward the IoT," *IEEE Communications Magazine*, vol. 56, no. 7, pp. 125-131, July 2018.

[57] I. Unwala, Z. Taqvi and J. Lu, "Thread: An IoT Protocol," in *2018 IEEE Green Technologies Conference (GreenTech)*, Austin, TX, 2018, pp. 161-167.

[58] J. Finnegan and S. Brown, "A Comparative Survey of LPWA Networking," arXiv:1802.04222, 2018.

[59] S. S. I. Samuel, "A review of connectivity challenges in IoT-smart home," in *2016 3rd MEC International Conference on Big Data and Smart City (ICBDSC)*, Muscat, 2016, pp. 1-4.

[60] S. Khssibi, H. Idoudi, A. V. Bossche, T. Val and L. A. Saidane, "Presentation and analysis of a new technology for low-power wireless sensor network," *International Journal of Digital Information and Wireless Communications (IJDIWC) 3.1 (2013)*, pp. 75-86.

[61] J. Lozano et al., "Personal electronic systems for citizen measurements of air quality," in *2019 5th Experiment International Conference (exp.at'19)*, Funchal (Madeira Island), Portugal, 2019, pp. 315-319.

[62] Sujuan Liu, Chuyu Xia and Zhenzhen Zhao, "A low-power real-time air quality monitoring system using LPWAN based on LoRa," in *2016 13th IEEE International Conference on Solid-State and Integrated Circuit Technology (ICSICT)*, Hangzhou, 2016, pp. 379-381.

[63] M. R. Hera, A. Rahman, A. Afrin, M. Y. S. Uddin and N. Venkatasubramanian, "AQBox: An air quality measuring box from COTS gas sensors," in *2017 International Conference on Networking, Systems and Security (NSysS)*, Dhaka, 2017, pp. 191-194.

[64] R, Y., S. S, T. M, K. A, R. V, and M. P, "NB-AirStream: Advancing Air Quality Monitoring with LoRa and NB-IoT Integration," in *2024 IEEE International Conference on Electronics, Computing and Communication Technologies (CONECCT)*, 2024, pp. 1–6.

[65] A. Abdaoui, S. H. M. Ahmad, H. Tariq, F. Touati, A. B. Mnaouer and M. Al-Hitmi, "Energy Efficient Real time Outdoor Air Quality Monitoring System," in *2020 International Wireless Communications and Mobile Computing (IWCMC)*, Limassol, Cyprus, 2020, pp. 2170-2176.

[66] Y. Lai, C. Lin, C. Wang, L. Tsai and J. Wang, "A Design of Portable Solar-Powered Air-Quality Monitor with Cloud-enabled Safety Watch Smartphone APP," in *2019 IEEE International Conference on Consumer Electronics - Taiwan (ICCE-TW)*, YILAN, Taiwan, 2019, pp. 1-2.

[67] Hou, Y., Z. Cai, Y. Zhang, Y. Cheng, J. Yang, F. Chen, and J. Zhang, "A Solar Powered General Purpose IoT Node for Smart Grid Applications," in *2024 6th International Conference on Circuits and Systems (ICCS)*, 2024, pp. 306–309.

[68] N. Dam, A. Ricketts, B. Catlett and J. Henriques, "Wearable sensors for analyzing personal exposure to air pollution," in *2017 Systems and Information Engineering Design Symposium (SIEDS)*, Charlottesville, VA, 2017, pp. 1-4.[69] S. Esfahani, P. Rollins, J. P. Specht, M. Cole and J. W. Gardner, "*Smart City Battery Operated IoT Based Indoor Air Quality Monitoring System*," in 2020 IEEE Sensors, Rotterdam, Netherlands, 2020, pp. 1-4.

[70] Jouda, M. and M. Wadi, "IoT with LoRa Architecture for Indoor Air Quality Monitoring System," in 2024 8th International Artificial Intelligence and Data Processing Symposium (IDAP), 2024, pp. 1–5.

[71] Pires, L. M., V. Fialho, T. Pécurto, and A. Madeira, "Towards Smart Wildfire Prevention: Development of a LoRa-Based IoT Node for Environmental Hazard Detection," *Designs*, vol. 9, no. 91, pp. 1–36, 2025.

[72] Shukla, P., A. Goel, V. Kumar, H. Kaur, V. K. Malav, and B. Rawat, "A Portable and Power-Efficient Flue Gas Monitoring System for Real-Time Air Quality Measurement," *IEEE Sensors Journal*, vol. 25, no. 14, pp. 27404–27413, 2025.

[73] Raina, R., K. J. Singh, and S. Kumar, "Air Sense: Internet of Things-enabled Novel Power Efficient Indoor Air Quality Monitoring System," in *2025 International Conference on Microwave, Optical, and Communication Engineering (ICMOCE)*, 2025, pp. 1–5.

[74] T. Glass, S. Ali, B. Parr, J. Potgieter and F. Alam, "IoT Enabled Low Cost Air Quality Sensor," in *2020 IEEE Sensors Applications Symposium (SAS)*, Kuala Lumpur, Malaysia, 2020, pp. 1-6.

[75] D. Oletic and V. Bilas, "Design of sensor node for air quality crowdsensing," in *2015 IEEE Sensors Applications Symposium (SAS)*, Zadar, 2015, pp. 1-5.

[76] Muhammed, N. A. and B. I. Saeed, "Design and Implementation of a Scalable LoRaWAN-Based Air Quality Monitoring Infrastructure for the Kurdistan Region of Iraq," *Future Internet*, vol. 17, no. 388, pp. 1–34, 2025.

[77] S. C. Folea and G. Mois, "A Low-Power Wireless Sensor for Online Ambient Monitoring," *IEEE Sensors Journal*, vol. 15, no. 2, pp. 742-749, Feb. 2015.

[78] Díaz, L., J. Azziz, J. P. Oliver, and F. Veirano, "Low-Power Wireless Sensor Network for Real-Time Indoor Air Quality Monitoring with CO2 Sensors," in *2024 IEEE 15th Latin America Symposium on Circuits and Systems (LASCAS)*, 2024, pp. 1–5.

[79] Sá, J. P., H. Chojer, P. T. B. S. Branco, A. Forstmaier, M. C. M. Alvim-Ferraz, F. G. Martins, and S. I. V. Sousa, "Selection and evaluation of commercial low-cost devices for indoor air quality monitoring in schools," *Journal of Building Engineering*, vol. 98, 2024.

[80] IQAir, AirVisual Pro Technical Specifications. [Online]. Available: https://www.iqair.com/us/air-quality-monitors/airvisual-pro/tech-specs. [Accessed: Oct. 23, 2025].

[81] Kaiterra, Laser Egg+ Chemical: Tech Specs. [Online]. Available: https://www.kaiterra.com/en/laser-egg-plus-chemical. [Accessed: Oct. 23, 2025].

[82] Honeywell, HPM Series Particle Sensor Datasheet. [Online]. Available: https://prod-edam.honeywell.com/content/dam/honeywell-edam/sps/siot/en-us/products/sensors/particulate-matter-sensors/hpm-series/documents/sps-siot-hpm-series-particle-sensor-datasheet-32322550-e-en.pdf. [Accessed: Oct. 23, 2025].

[83] PocketLab, PocketLab Air Specifications. [Online]. Available: https://www.thepocketlab.com/store/pocketlab-air. [Accessed: Oct. 23, 2025].

[84] Airthings, Airthings Wave Plus Datasheet. [Online]. Available: https://www.airthings.com/hubfs/Website/Data%20Sheets/Airthings_Wave_Plus_Datasheet.pdf. [Accessed: Oct. 23, 2025].

[85] J. E. Shuda, A. J. Rix and M. J. Booysen, "Towards Module-Level Performance and Health Monitoring of Solar PV Plants Using LoRa Wireless Sensor Networks," in *2018 IEEE PES/IAS PowerAfrica*, Cape Town, 2018, pp. 172-177.

[86] W. Xue-fen, Y. Yi and C. Jian, "Wireless Sensor Node with Lightning and Atmospheric Pressure Detection for Severe Convective Weather Warning Networks," in *2018 International Symposium in Sensing and Instrumentation in IoT Era (ISSI)*, Shanghai, 2018, pp. 1-6.

[87] P. Guan, Z. Zhang, L. Wei and Y. Zhao, "A Real-Time Bus Positioning System Based on LoRa Technology," in *2018 2nd International Conference on Smart Grid and Smart Cities (ICSGSC)*, Kuala Lumpur, 2018, pp. 45-48.

[88] A. M. Manoharan and V. Rathinasabapathy, "Smart Water Quality Monitoring and Metering Using Lora for Smart Villages," in *2018 2nd International Conference on Smart Grid and Smart Cities (ICSGSC)*, Kuala Lumpur, 2018, pp. 57-61.

[89] G. Pasolini et al., "Smart City Pilot Project Using LoRa," in *European Wireless 2018; 24th European Wireless Conference*, Catania, Italy, 2018, pp. 1-6.

[90] F. E. Soares e Silva, C. H. Barriquello, L. N. Canha, D. P. Bernardon and W. H. Seizo, "Deployment of LoRA WAN Network for Rural Smart Grid in Brazil," in *2018 IEEE PES Transmission & Distribution Conference and Exhibition - Latin America (T&D-LA)*, 2018, pp 1-5.

[91] Z. qin, Y. shenglong, Z. heng, C. xuesheng, Z. shengmao and D. yang, "Design and Implementation of Marine Temperature Measurement System Based on LoRa," in *2018 International Symposium in Sensing and Instrumentation in IoT Era (ISSI)*, Shanghai, 2018, pp. 1-4.

[92] Mihir, D., Y. A. Aralaguppi, M. Belwal, B. V. D. Pavan, and P. B. Nair, "Environmental Monitoring using LoRa and NodeMCU," in *2025 3rd International Conference on Intelligent Data Communication Technologies and Internet of Things (IDCIoT)*, 2025, pp. 603–609.

[93] P. Sommer, Y. Maret and D. Dzung, "Low-Power Wide-Area Networks for Industrial Sensing Applications," in *2018 IEEE International Conference on Industrial Internet (ICII)*, Seattle, WA, 2018, pp. 23-32.

[94] G. Yang and H. Liang, "A Smart Wireless Paging Sensor Network for Elderly Care Application Using LoRaWAN," *IEEE Sensors Journal*, vol. 18, no. 22, pp. 9441-9448, 15 Nov.15, 2018.

[95] I. Rodriguez, M. Lauridsen, G. Vasluianu, A. N. Poulsen and P. Mogensen, "The Gigantium Smart City Living Lab: A Multi-Arena LoRa-based Testbed," in *2018 15th International Symposium on Wireless Communication Systems (ISWCS)*, Lisbon, 2018, pp. 1-6.

[96] F. Gui, Y. Yin and A. Lu, "Research on Ship Wireless Communication Technology Based on LoRa," in *2018 2nd IEEE Advanced Information Management,Communicates,Electronic and Automation Control Conference (IMCEC)*, Xi'an, 2018, pp. 976-979.

[97] Zhao, L., J. PAN, and L. Xiqiang, "Design of fire water supply pipeline pressure monitoring system based on LoRa," in *2024 IEEE 6th Advanced Information Management, Communicates, Electronic and Automation Control Conference (IMCEC)*, 2024, pp. 401–405.

[98] M. Rahman and A. Saifullah, “LoRaIN: A Constructive Interference-Assisted Reliable and Energy-Efficient LoRa Indoor Network,” *in Proc. of the IEEE/ACM International Conference on Internet of Things Design and Implementation (IoTDI)*, 2025.

[99] F. Wu, J. Redouté and M. R. Yuce, "WE-Safe: A Self-Powered Wearable IoT Sensor Network for Safety Applications Based on LoRa," *IEEE Access*, vol. 6, pp. 40846-40853, 2018.

[100] W. Chen and Z. Lin, "A Prototype Development of the Smart Mousetrap System Equipped with LoRa," in *2018 IEEE International Conference on Consumer Electronics-Taiwan (ICCE-TW)*, Taichung, 2018, pp. 1-5.

[101] Sensirion, SPS30 Particulate Matter Sensor for Air Quality Monitoring and Control Datasheet. [Online]. Available: https://sensirion.com/media/documents/B4434665/627C442D/Datasheet. [Accessed: Oct. 23, 2025].

[102] SCD30 Sensor Module for NDIR CO_2 Detection Datasheet. [Online]. Available: https://sensirion.com/media/documents/95333413/616042DE/Datasheet. [Accessed: Oct. 23, 2025].

[103] Sensirion, SGP30 TVOC and CO_2eq Sensor for Indoor Air Quality Applications Datasheet. [Online]. Available:

https://sensirion.com/media/documents/48D3466A/61662C3A/Datasheet. [Accessed: Oct. 23, 2025].

[104] Bosch Sensortec, BST-BME280-DS002 Datasheet. [Online]. Available: https://www.bosch-sensortec.com/media/boschsensortec/downloads /datasheets/bst-bme280-ds002.pdf. [Accessed: Oct. 23, 2025].

[105] HopeRF, RFM95/96/97/98(W) Datasheet. [Online]. Available: https://www.hoperf.com/data/upload/portal/20190301/RFM95_96_97_98W.pdf. [Accessed: Oct. 23, 2025].

[106] ATSAMD21G18 Microcontroller [14] Microchip Technology Inc., ATSAMD21G18 - SAM D21 Family Datasheet. [Online]. Available: https://ww1.microchip.com/downloads/en/DeviceDoc/SAM-D21-Family-Data-Sheet-DS40001882G.pdf. [Accessed: Oct. 23, 2025].

[107] Rocket Scream Mini Ultra Pro V3 [15] Rocket Scream, Mini Ultra Pro V3 Product Page. [Online]. Available: https://www.rocketscream.com/blog/product/mini-ultra-pro-v3/. [Accessed: Oct. 23, 2025].

[108] Microne, ME6210 Series Datasheet. [Online]. Available: http://www.microne.com.cn/datasheet/ME6210. [Accessed: Oct. 23, 2025].

[109] Winbond Electronics Corporation, W25Q16JV Datasheet. [Online]. Available: https://www.winbond.com/resource-files/w25q16jv%20revf%2005192017.pdf. [Accessed: Oct. 23, 2025].

[110] Microchip Technology Inc., 24AA025E64/24LCS25E64 Datasheet. [Online]. Available: https://ww1.microchip.com/downloads/aemDocuments/documents /OTH/ProductDocuments/DataSheets/20002124G.pdf. [Accessed: Oct. 23, 2025].

[111] Texas Instruments, TPS27081A 8-V, 1-A, 80-mΩ P-Channel High-Side Load Switch Datasheet. [Online]. Available: https://www.ti.com/lit/ds/symlink/tps27081a.pdf. [Accessed: Oct. 23, 2025].

[112] Texas Instruments, TPS62745 360-nA IQ Step-Down Converter Datasheet. [Online]. Available: https://www.ti.com/lit/ds/symlink/tps62745.pdf. [Accessed: Oct. 23, 2025].

[113] Texas Instruments, LMZM23600 36-V, 0.5-A Step-Down DC-DC Power Module Datasheet. [Online]. Available: https://www.ti.com/lit/ds/symlink/lmzm23600.pdf. [Accessed: Oct. 23, 2025].

[114] Analog Devices, Inc., LTC2956 Wake-Up Timer with Pushbutton Control Datasheet. [Online]. Available: https://www.analog.com/media/en/technical-documentation/data-sheets/LTC2956.pdf. [Accessed: Oct. 23, 2025].

[115] Texas Instruments, TPS61099x Low-Iq Synchronous Boost Converter Datasheet. [Online]. Available: https://www.ti.com/lit/ds/symlink/tps61099.pdf. [Accessed: Oct. 23, 2025].

[116] Nisshinbo Micro Devices Inc., RP604 Series Datasheet. [Online]. Available: https://www.nisshinbo-microdevices.co.jp/en/pdf/datasheet/rp604-ea.pdf. [Accessed: Oct. 23, 2025].

[117] Microchip Technology Inc., MCP1811A/12A Low Quiescent Current LDO Regulator Datasheet. [Online]. Available: https://ww1.microchip.com/downloads/en/DeviceDoc/MCP1811A-12A-Low-Quiescent-Current-LDO-Regulator-DS20006385A.pdf. [Accessed: Oct. 23, 2025].

[118] Texas Instruments, TPS22860 18-V, 1-A, 1.2-Ω On-Resistance Load Switch Datasheet. [Online]. Available: https://www.ti.com/lit/ds/symlink/tps22860.pdf. [Accessed: Oct. 23, 2025].

[119] Texas Instruments, TPL5111 Nano-Power System Timer With MOS Driver Datasheet. [Online]. Available: https://www.ti.com/lit/ds/symlink/tpl5111.pdf. [Accessed: Oct. 23, 2025].

[120] Analog Devices, Inc., MAX5417/MAX5418/MAX5419 Datasheet. [Online]. Available: https://www.analog.com/media/en/technical-documentation/data-sheets/MAX5417-MAX5419.pdf. [Accessed: Oct. 23, 2025].

[121] Texas Instruments, TCA9548A Low-Voltage 8-Channel I²C Switch With Reset Datasheet. [Online]. Available: https://www.ti.com/lit/ds/symlink/tca9548a.pdf. [Accessed: Oct. 23, 2025].

[122] NXP Semiconductors, PCF8575 Remote 16-bit I/O expander for I²C-bus with interrupt Datasheet. [Online]. Available: https://www.nxp.com/docs/en/data-sheet/PCF8575.pdf. [Accessed: Oct. 23, 2025].

[123] Microchip Technology Inc., MCP73831/2 Miniature Single-Cell, Fully Integrated Li-Ion / Li-Polymer Charge Management Controllers Datasheet. [Online]. Available: https://ww1.microchip.com/downloads/en/DeviceDoc/20001984g.pdf. [Accessed: Oct. 23, 2025].

[124] SGX Sensortech, MiCS-6814 Datasheet. [Online]. Available: https://www.amphenol-sensors.com/hubfs/Documents/SGX-Sensortech/MiCS-6814-Datasheet.pdf. [Accessed: Oct. 23, 2025].

[125] Texas Instruments, TPS62746 360-nA IQ Step-Down Converter for Low-Power Wireless Applications Datasheet. [Online]. Available: https://www.ti.com/lit/ds/symlink/tps62746.pdf. [Accessed: Oct. 23, 2025].

[126] Petäjäjärvi J, Mikhaylov K, Pettissalo M, Janhunen J, Iinatti J. Performance of a low-power wide-area network based on LoRa technology: Doppler robustness, scalability, and coverage. International Journal of Distributed Sensor Networks. 2017;13(3).doi:10.1177/1550147717699412.

[127] A. Augustin, J. Yi, T. Clausen, and W. M. Townsley, “A study of LoRa: Long range & low power networks for the Internet of Things,” *Sensors*, vol. 16, no. 9, p. 1466, 2016.

[128] S. Hosseinzadeh, H. Larijani, and K. Curtis, "An enhanced modified multi wall propagation model," 2017 Global Internet of Things Summit (GIoTS), 2017, pp. 1-4.

[129] V. Prasad and S. K. Sharma, “Integrating COST 231 Multiwall Propagation Model for Indoor Wireless Communication,” *The Open Journal of Applied Sciences*, vol. 12, no. 4, pp. 94–103, 2014.

[130] COST 231, “Urban Transmission Loss Models for Mobile Radio in the 900 and 1800 MHz Bands,” COST 231 Final Report, 1999.

[131] T. S. Rappaport, Wireless Communications: Principles and Practice, 2nd ed. Prentice Hall, 2002.

[132] ITU-R, “Recommendation P.1238-9: Propagation data and prediction methods for the planning of indoor radiocommunication systems,” 2023.

[133] 3GPP, “Technical Specification 38.901: Study on channel model for frequencies from 0.5 to 100 GHz,” 2020.

[134] A. Goldsmith, *Wireless Communications*. Cambridge, U.K.: Cambridge Univ. Press, 2005.

[135] S. Saunders and A. Aragón-Zavala, *Antennas and Propagation for Wireless Communication Systems*, 2nd ed. New York, NY, USA: Wiley, 2007.

[136] European Telecommunications Standards Institute (ETSI), *Short Range Devices (SRD) operating in the frequency range 25 MHz to 1 000 MHz; Part 1: Technical characteristics and test methods*, EN 300 220-1 V3.2.1, 2018.

[137] LoRa Alliance, *LoRaWAN™ Regional Parameters*, Version 1.0.3, July 2018. [Online]. Available: https://lora-alliance.org/resource_hub/lorawan-regional-parameters-v1-0/

[138] F. Adelantado, X. Vilajosana, P. Tuset, B. Martinez, J. Melia, and T. Watteyne, "Understanding the Limits of LoRaWAN," *IEEE Communications Magazine*, vol. 55, no. 9, pp. 34–40, Sept. 2017.

[139] Semtech Corporation, *AN1200.13 LoRa Modem Designer's Guide*, Revision 2, July 2013. [Online]. Available: https://www.semtech.com/uploads/documents/an1200.13.pdf

[140] G. Ferré and A. Giremus, "LoRa physical layer principle and performance analysis," in *IEEE Int. Conf. Acoust., Speech Signal Process. (ICASSP)*, pp. 6548–6552, 2018.

[141] M. C. Bor et al., "Do LoRa low-power wide-area networks scale?" in *ACM Int. Conf. Modeling, Anal. Simul. Wireless Mobile Syst.*, pp. 59–67, 2016.

[142] J. Marais, L. O. Sabugo, and F. J. López-Martínez, "On the Error Correction Capabilities of LoRa PHY Coding," *IEEE Internet of Things J.*, vol. 9, no. 16, pp. 15009–15019, Aug. 2022.

[143] J. G. Proakis and M. Salehi, *Digital Communications*, 5th ed. New York, NY, USA: McGraw-Hill, 2008.

[144] A. Elshabrawy and J. Robert, "Performance Evaluation of LoRa LPWAN Technology for IoT Applications,"in *Proc. IEEE ICC*, 2018.

[145] C. Rattanapoka, S. Chanthakit, A. Chimchai and A. Sookkeaw, "An MQTT-based IoT Cloud Platform with Flow Design by Node-RED," in *2019 Research, Invention, and Innovation Congress (RI2C)*, Bangkok, Thailand, 2019, pp. 1-6.

[146] N. Naik, "Choice of effective messaging protocols for IoT systems: MQTT, CoAP, AMQP and HTTP," in *2017 IEEE International Systems Engineering Symposium (ISSE)*, Vienna, 2017, pp. 1-7.

[147] S. M. Saad, A. Y. M. Shakaff, A. R. M. Saad, A. M. Yusof, A. M. Andrew, A. Zakaria, and A. H. Adom, "Development of indoor environmental index: Air quality index

and thermal comfort index," in *AIP Conference Proceedings 1808*, 2017, pp. 020043-1–020043-11.

[148] S. Chickerur, A. Goudar and A. Kinnerkar, "Comparison of Relational Database with Document-Oriented Database (MongoDB) for Big Data Applications," in *2015 8th International Conference on Advanced Software Engineering & Its Applications (ASEA)*, Jeju, 2015, pp. 41-47.

[149] Samsung SDI, Specification of Product INR18650-35E. [Online]. Available: https://cdn.batemo.de/products/samsung-inr18650-35e-data-sheet.pdf. [Accessed: Oct. 23, 2025].

[150] Ebyte, TK868-JKD-20 Product Data Sheet [Online]. Available: https://www.cdebyte.com/pdf-down.aspx?id=1056&_gl=1*7p7tij*_up*MQ..*_ga*MjAxODE1NDk1NS4xNzYxMjM0NjYy*_ga_YQYYBFPDGW*czE3NjEyMzQ2NTMkbzEkZzEkdDE3NjEyMzQ2NjEkajUyJGwwJGg4MTA2OTg4NDM.*_ga_87PTK0Y2S4*czE3NjEyMzQ2NjEkbzEkZzAkdDE3NjEyMzQ2NjEkajYwJGwwJGgw. [Accessed: Oct. 23, 2025].

Appendices

Appendix 1: 2nd prototype sensor node circuit schematic

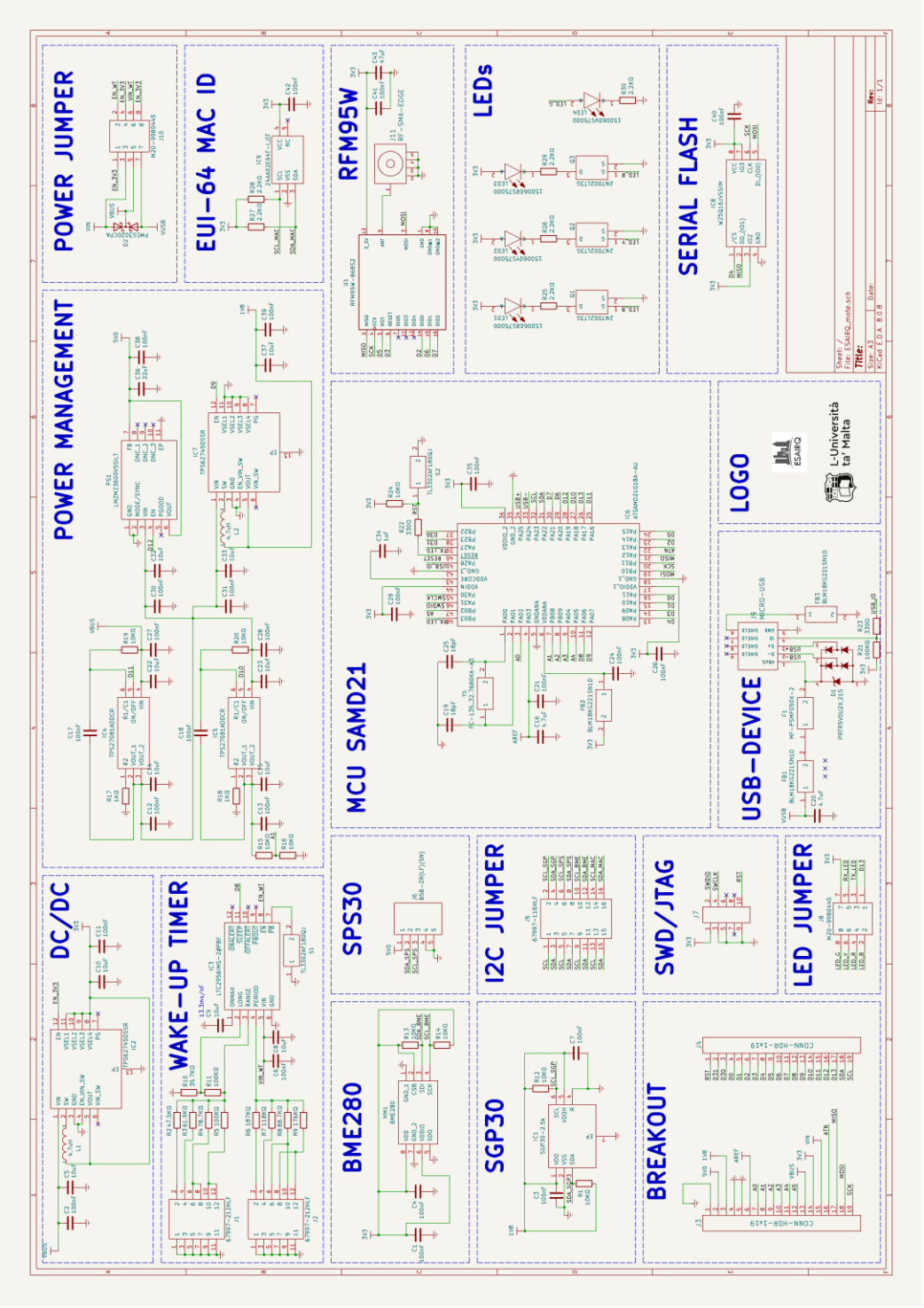

Appendix 2: 3rd prototype sensor node circuit schematic

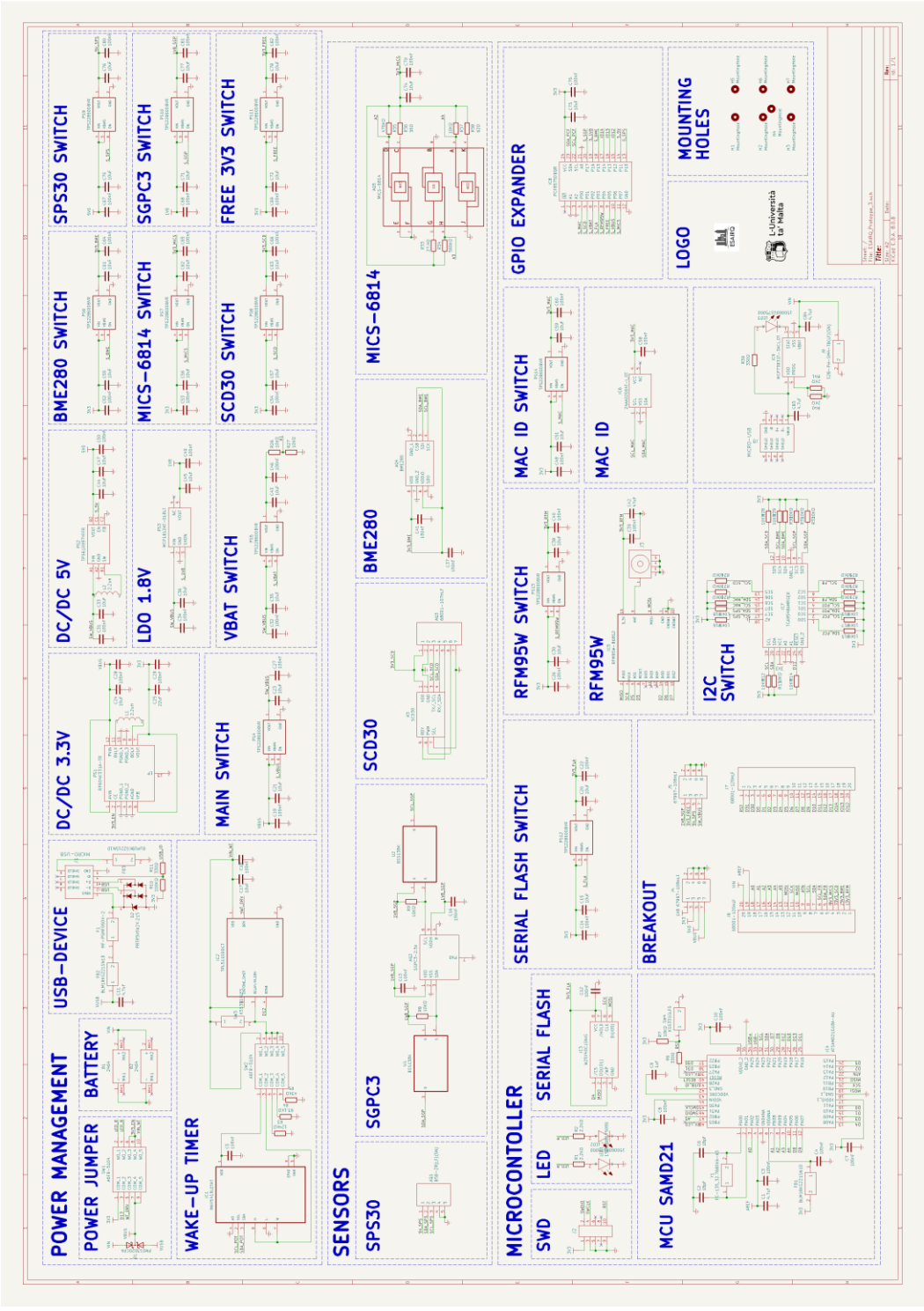

Appendix 3: 4th prototype sensor node power management circuit schematic

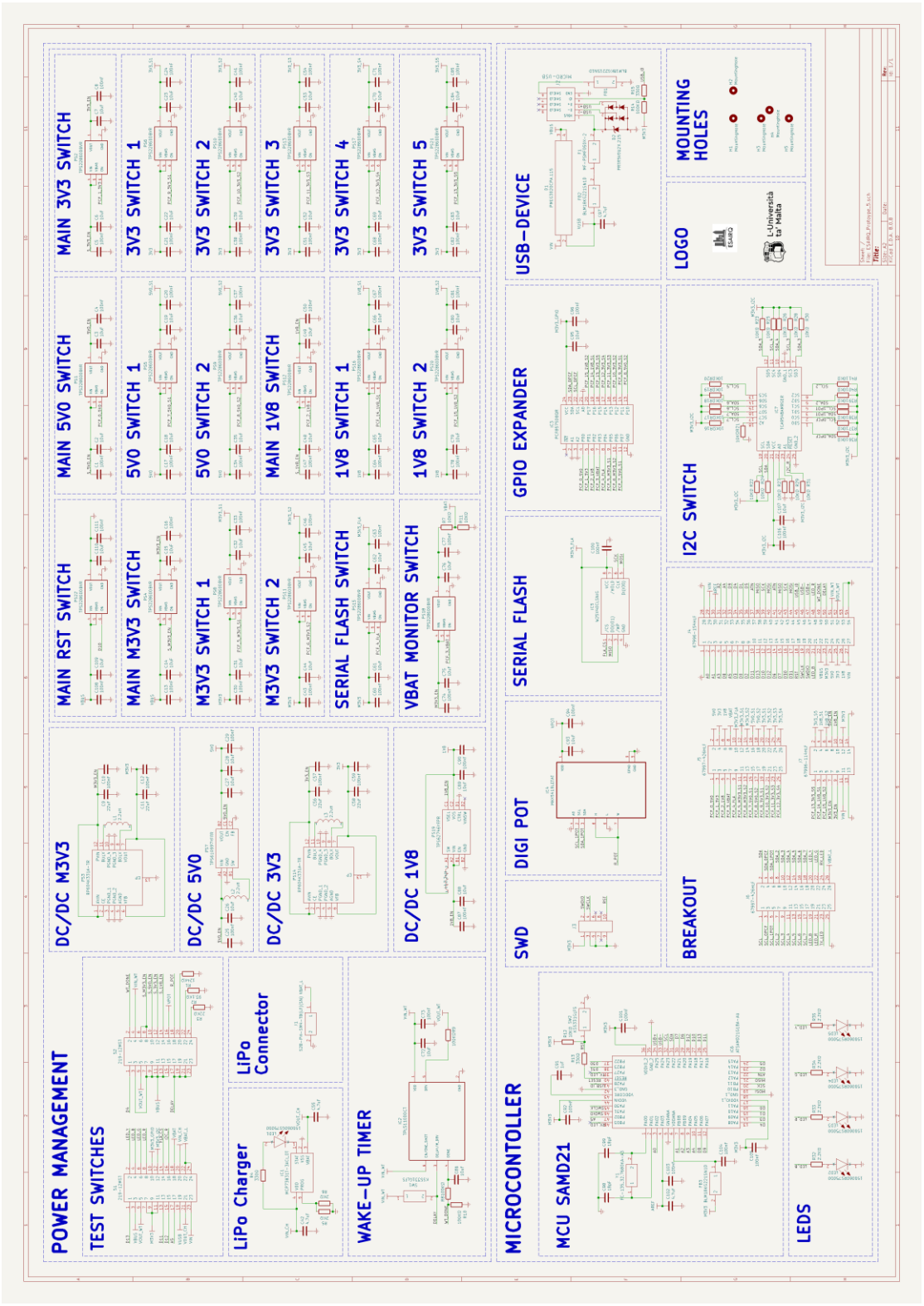

Appendix 4: 4th prototype sensor node air quality sensor shield circuit schematic

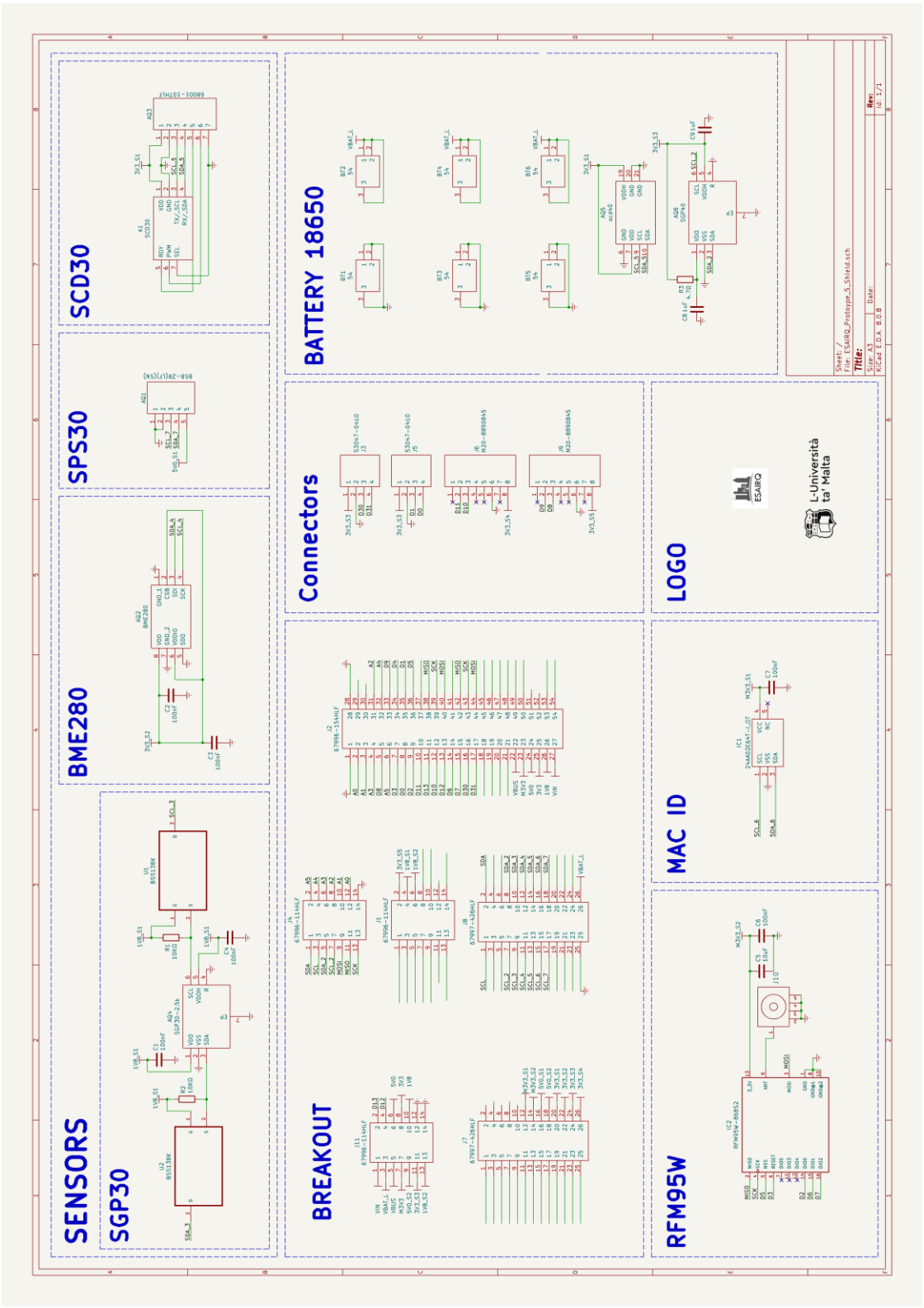

Appendix 5: Code excerpts from the program written for the 4th prototype sensor node

```
void lmic_setup() { // Function to setup RFM95W
  #ifdef VCC_ENABLE
  pinMode(VCC_ENABLE, OUTPUT);
  digitalWrite(VCC_ENABLE, HIGH);
  delay(100);
  #endif
  os_init();          // LMIC init
  LMIC_reset();       // Reset the MAC state.
  do_send(&sendjob); // Start job
}

void pcf_setup() { // Function to setup PCF8575
  pcf8575.pinMode(s_mac,    OUTPUT);
  pcf8575.pinMode(s_scd,    OUTPUT);
  pcf8575.pinMode(s_vbat,   OUTPUT);
  pcf8575.pinMode(s_fla,    OUTPUT);
  pcf8575.pinMode(s_rfm,    OUTPUT);
  pcf8575.pinMode(s_3v3,    OUTPUT);
  pcf8575.pinMode(s_sgp40, OUTPUT);
  pcf8575.pinMode(s_3v3_s4, OUTPUT);
  pcf8575.pinMode(s_sps,    OUTPUT);
  pcf8575.pinMode(s_5v0,    OUTPUT);
  pcf8575.pinMode(s_5v0_s2, OUTPUT);
  pcf8575.pinMode(s_3v3_s5, OUTPUT);
  pcf8575.pinMode(s_1v8_s2, OUTPUT);
  pcf8575.pinMode(s_bme,    OUTPUT);
  pcf8575.pinMode(s_1v8,    OUTPUT);
  pcf8575.pinMode(s_sgp,    OUTPUT);
  Wire.begin();
  tcaselect(i_pcf);
  Wire.beginTransmission(a_pcf);
  pcf8575.digitalWrite(s_mac,    LOW);
  pcf8575.digitalWrite(s_scd,    LOW);
  pcf8575.digitalWrite(s_vbat,   LOW);
  pcf8575.digitalWrite(s_fla,    LOW);
  pcf8575.digitalWrite(s_rfm,    HIGH);
  pcf8575.digitalWrite(s_3v3,    LOW);
  pcf8575.digitalWrite(s_sgp40, LOW);
  pcf8575.digitalWrite(s_3v3_s4, LOW);
  pcf8575.digitalWrite(s_sps,    LOW);
  pcf8575.digitalWrite(s_5v0,    LOW);
  pcf8575.digitalWrite(s_5v0_s2, LOW);
  pcf8575.digitalWrite(s_3v3_s5, LOW);
  pcf8575.digitalWrite(s_1v8_s2, LOW);
  pcf8575.digitalWrite(s_bme,    LOW);
  pcf8575.digitalWrite(s_1v8,    LOW);
  pcf8575.digitalWrite(s_sgp,    LOW);
  Wire.endTransmission();
  serial.println("PCF Setup done!");
}
```

```
void tcaselect(uint8_t i) { // Function to select TCA9548 channel
  if (i > 7) return;
  Wire.beginTransmission(TCAADDR); Wire.write(1 << i);
Wire.endTransmission();
}

void pot_setup(uint8_t i) { // Function to setup MAX5419
  tcaselect(i_pot); Wire.beginTransmission(a_pot);
// Initialising MAX5419 transmission
  digiPot.write(MAX541X_VREG, i); digiPot.writeNonvolatile(i);
// Setting MAX5419 resistance value
  serial.print("Programmed R: "); serial.println(digiPot.getR());
serial.print("Value:"); serial.println(i);
  Wire.endTransmission();
}

void gpio_setup() {           // Function to setup GPIO pins
  //while (!serial);          // Waiting for USB serial port to connect
  serial.begin(115200);       // Starting USB serial port
  pinMode(wt_slp, OUTPUT);    // Wake-up timer done pin
  pinMode(yled, OUTPUT);      // Yellow LED pin
  pinMode(vbat, INPUT);       // Battery monitoring pin
  digitalWrite(wt_slp, LOW); // Setting wake-up timer to not sleep
  digitalWrite(yled, LOW);    // Switching off yellow led
  serial.println("Pin setup done!");
}

void set_lpp() { // Setting up the LPP payload
  measure_sensors();
  lpp.reset();
  lpp.addTemperature(1, temperature);
// Temperature °C (Size: 2 bytes, Resolution: 0.1 °C Signed)
  lpp.addRelativeHumidity(2, humidity);
// Humidity %RH    (Size: 1 byte,  Resolution: 0.5% Unsigned)
  lpp.addBarometricPressure(3, pressure);
// Pressure hPa    (Size: 2 bytes, Resolution: 0.1 hPa Unsigned)
  lpp.addAnalogInput(3, vbat_actual);
// Battery voltage V (Size: 2 bytes, Resolution: 0.01 Signed)
  lpp.addLuminosity(4, tvoc);
// TVOC ppb (Size: 2 bytes, Resolution: 1 Unsigned)
  lpp.addLuminosity(5, eco2);
// eCO2 ppm (Size: 2 bytes, Resolution: 1 Unsigned)
  lpp.addLuminosity(6, co2);
// CO2 ppm (Size: 2 bytes, Resolution: 1 Unsigned)
  lpp.addAnalogInput(7, measurement.mc_1p0);
// PM1.0 µg/m³ (Size: 2 bytes, Resolution: 0.01 Signed)
  lpp.addAnalogInput(8, measurement.mc_2p5);
// PM2.5 µg/m³ (Size: 2 bytes, Resolution: 0.01 Signed)
  lpp.addAnalogInput(9, measurement.mc_4p0);
// PM4.0 µg/m³ (Size: 2 bytes, Resolution: 0.01 Signed)
  lpp.addAnalogInput(10, measurement.mc_10p0);
// PM10.0 µg/m³ (Size: 2 bytes, Resolution: 0.01 Signed)
  lpp.addAnalogInput(11, measurement.typical_particle_size);
// Typical Particle Size µm (Size: 2 bytes, Resolution: 0.01 Signed)
  serial.println("LPP set!");
```

```
}

void measure_sensors() {
  delay(5000);
  serial.println("Measuring Sensors!");
  measure_vbat();     // Measuring battery voltage
  measure_bme280();   // Measuring T/hPa/RH
  measure_scd30();    // Measuring CO2&SPS30+SGP30 during 20s response
time
}

void measure_vbat() { // Function to measure the battery voltage
  tcaselect(i_pcf); Wire.beginTransmission(a_pcf);
// Starting transmission to PCF8575 GPIO expander
  pcf8575.digitalWrite(s_vbat, HIGH);
// Switching on load switch to measure vbat via potential divider
  timer = millis();
  delay(100);
  vbat_actual = (analogRead(vbat));
// Measuring actual battery voltage
  vbat_actual = (vbat_actual / 1023) * 6.6;
  serial.print("VBAT        : "); serial.print(vbat_actual);
serial.println(" V");
  serial.print(millis() - timer); serial.println(" ms");
  pcf8575.digitalWrite(s_vbat, LOW);
// Switching off load switch (potential divider)
  Wire.endTransmission();
}

void measure_bme280() { // Function to measure BME280
  tcaselect(i_pcf); Wire.beginTransmission(a_pcf);
// Starting transmission to PCF8575 GPIO expander
  pcf8575.digitalWrite(s_3v3, HIGH);
// Switching on 3V3 DC/DC convertor
  pcf8575.digitalWrite(s_bme, HIGH);
// Switching on load switch to measure BME280
  Wire.endTransmission();
  tcaselect(i_bme); Wire.beginTransmission(a_bme);
// Starting transmission to BME280
  timer = millis();
  if (! bme.begin()) {
// Initialising BME280 sensor
    serial.println("BME Sensor not found :(");
    while (1);
  }
  temperature = bme.readTemperature();
// Measuring temperature
  pressure = bme.readPressure() / 100.0F;
// Measuring pressure
  altitude = bme.readAltitude(SEALEVELPRESSURE_HPA);
// Measuring altitude
  humidity = bme.readHumidity();
// Measuring humidity
  serial.print("Temperature : "); serial.print(temperature);
  serial.println(" *C");
```

```
  serial.print("Pressure    : "); serial.print(pressure / 100.0F);
  serial.println(" hPa");
  serial.print("Altitude    : "); serial.print(altitude);
  serial.println(" m");
  serial.print("Humidity    : "); serial.print(humidity);
  serial.println(" %");
  serial.print(millis() - timer); serial.println(" ms");
  Wire.endTransmission();
  tcaselect(i_pcf); Wire.beginTransmission(a_pcf);
// Starting transmission to PCF8575 GPIO expander
  pcf8575.digitalWrite(s_bme, LOW);
// Switching off load switch to measure BME280
  pcf8575.digitalWrite(s_3v3, LOW);
// Switching off 3V3 DC/DC convertor
  Wire.endTransmission();
}

void measure_scd30() { // Function to measure SCD30
  tcaselect(i_pcf); Wire.beginTransmission(a_pcf);
// Starting transmission to PCF8575 GPIO expander
  pcf8575.digitalWrite(s_3v3, HIGH);
// Switching on 3V3 DC/DC convertor
  pcf8575.digitalWrite(s_scd, HIGH);
// Switching on load switch to measure SCD30
  Wire.endTransmission();
  tcaselect(i_scd); Wire.beginTransmission(a_scd);
// Starting transmission to SCD30
  timer = millis();
  while (! airSensor.begin()) {
// Initialising SCD30 sensor
  }
  Wire.endTransmission();
  measure_sps30();
// Measuring SPS30 during 20s response time
  measure_sgp30();
// Measuring SGP30 during 20s response time
  //measure_sgp40();
// Measuring SGP40 during 20s response time
  tcaselect(i_scd); Wire.beginTransmission(a_scd);
// Re-Starting transmission to SCD30
  while (! airSensor.dataAvailable()) {
// Starting SCD30 measurement
  }
  co2 = airSensor.getCO2();
// Measuring CO2
  stemperature = airSensor.getTemperature();
// Measuring temperature
  shumidity = airSensor.getHumidity();
// Measuring humidity
  serial.print("CO2         : "); serial.print(co2);
  serial.println(" ppm");
  serial.print("Temperature : "); serial.print(stemperature);
  serial.println(" *C");
  serial.print("Humidity    : "); serial.print(shumidity);
  serial.println(" %");
```

```
  serial.print(millis() - timer); serial.println(" ms");
  Wire.endTransmission();
  tcaselect(i_pcf); Wire.beginTransmission(a_pcf);
// Starting transmission to PCF8575 GPIO expander
  pcf8575.digitalWrite(s_scd, LOW);
// Switching off load switch to measure SCD30
  pcf8575.digitalWrite(s_3v3, LOW);
// Switching off 3V3 DC/DC convertor
  Wire.endTransmission();
}

void measure_sps30() { // Function to measure SPS30
  tcaselect(i_pcf); Wire.beginTransmission(a_pcf);
// Starting transmission to PCF8575 GPIO expander
  pcf8575.digitalWrite(s_5v0, HIGH);
// Switching on 5V0 DC/DC convertor
  pcf8575.digitalWrite(s_sps, HIGH);
// Switching on load switch to measure SPS30
  Wire.endTransmission();
  tcaselect(i_sps); Wire.beginTransmission(a_sps);
// Starting transmission to SPS30
  timer = millis();
  while (measurement.nc_0p5 == 0) {
    sps30_start_measurement();
// Starting measurement
    delay(4000);
// Delay time to get air flowing into the sensor
    ret = sps30_read_measurement(&measurement);
// Getting measurement
    sps30_stop_measurement();
// Stopping measurement
  }
  if (ret < 0) {
    serial.write("read measurement failed\n");
// Checking if measurement was performed correctly
  } else {
    serial.print("PM 0.5      : ");
    serial.print(measurement.nc_0p5, DEC);
    serial.println("/cm³");
    serial.print("PM 1        : ");
    serial.print(measurement.mc_1p0, DEC);
    serial.print(" µg/m³, ");
    serial.print(measurement.nc_1p0, DEC);
    serial.println("/cm³");
    serial.print("PM 2.5      : ");
    serial.print(measurement.mc_2p5, DEC);
    serial.print(" µg/m³, ");
    serial.print(measurement.nc_2p5, DEC);
    serial.println("/cm³");
    serial.print("PM 4        : ");
    serial.print(measurement.mc_4p0, DEC);
    serial.print(" µg/m³, ");
    serial.print(measurement.nc_4p0, DEC);
    serial.println("/cm³");
    serial.print("PM 10       : ");
```

```
    serial.print(measurement.mc_10p0, DEC);
    serial.print(" µg/m³, ");
    serial.print(measurement.nc_10p0, DEC);
    serial.println("/cm³");
    serial.print("TPS          : ");
    serial.print(measurement.typical_particle_size, DEC);
    serial.println("µm");
  }
  serial.print(millis() - timer); serial.println(" ms");
  Wire.endTransmission();
  tcaselect(i_pcf); Wire.beginTransmission(a_pcf);
// Starting transmission to PCF8575 GPIO expander
  pcf8575.digitalWrite(s_sps, LOW);
// Switching off load switch to measure sps30
  pcf8575.digitalWrite(s_5v0, LOW);
// Switching off 5V0 DC/DC convertor
  Wire.endTransmission();
}

void measure_sgp30() { // Function to measure SGP30
  tcaselect(i_pcf); Wire.beginTransmission(a_pcf);
// Starting transmission to PCF8575 GPIO expander
  pcf8575.digitalWrite(s_1v8, HIGH);
// Switching on 1V8 DC/DC convertor
  pcf8575.digitalWrite(s_sgp, HIGH);
// Switching on load switch to measure SGP30
  Wire.endTransmission();
  delay(100);
  tcaselect(i_sgp); Wire.beginTransmission(a_sgp);
// Starting transmission to SGP30
  sgp.begin();
  //serial.print("Found SGP30 serial #");
  //serial.print(sgp.serialnumber[0], HEX);
  //serial.print(sgp.serialnumber[1], HEX);
  //serial.println(sgp.serialnumber[2], HEX);
  sgpcount = 1400;
// Counter for readings to stabilise
  timer = millis();
  sgp.setHumidity(getAbsoluteHumidity(temperature, humidity));
//evaluating absolute humidity
  while (sgpcount > 0) {
    if (! sgp.IAQmeasure()) {
      serial.println("Measurement failed");
      return;
    }
    tvoc = sgp.TVOC;
    eco2 = sgp.eCO2;
    sgpcount = sgpcount - 1;
  }
  serial.print("TVOC "); serial.print(sgp.TVOC); serial.print(" ppb\t");
  serial.print("eCO2 "); serial.print(sgp.eCO2); serial.println(" ppm");
  serial.print(millis() - timer); serial.println(" ms");
  Wire.endTransmission();
  tcaselect(i_pcf); Wire.beginTransmission(a_pcf);
// Starting transmission to PCF8575 GPIO expander
```

```
  pcf8575.digitalWrite(s_sgp, LOW);
// Switching off load switch to measure SGP30
  pcf8575.digitalWrite(s_1v8, LOW);
// Switching off 1V8 DC/DC convertor
  Wire.endTransmission();
}

void readEUI() { // Function to read MAC-EUI
  tcaselect(i_pcf); Wire.beginTransmission(a_pcf);
// Starting transmission to PCF8575 GPIO expander
  pcf8575.digitalWrite(s_mac, HIGH);
// Switching on load switch to read MAC-EUI
  Wire.endTransmission();
  tcaselect(i_mac); Wire.beginTransmission(a_mac);
// Starting transmission to MAC-EUI
  Wire.write(0xF8);
// Memory address where read only MAC address resides
  Wire.endTransmission();
  Wire.requestFrom(0x50, 8);
// Request 8 bytes from the device
  while (Wire.available()) {
    serial.print("0x");
    serial.print(Wire.read(), HEX);
    serial.print(" ");
  }
  serial.println();
  Wire.endTransmission();
  tcaselect(i_pcf); Wire.beginTransmission(a_pcf);
// Starting transmission to PCF8575 GPIO expander
  pcf8575.digitalWrite(s_mac, LOW);
// Switching off load switch of MAC-EUI
  Wire.endTransmission();
}
```

Appendix 6: Code excerpts from the theoretical LoRa simulation model

```
%% Simulation and Building Parameters
levels = [-2, -1, 0, 1];
% Floor indices
floor_height = 5;
% Height per level (m)

% Block A (left) and Block B (right) dimensions on x-y plane
blockA.x_min = -42.5; blockA.x_max = -2.5;
blockA.y_min = -20;   blockA.y_max = 20;
blockB.x_min = 2.5;   blockB.x_max = 42.5;
blockB.y_min = -20;   blockB.y_max = 20;

% Corridor linking blocks
corridor.x_min = -2.5; corridor.x_max = 2.5;
corridor.y_min = -10;  corridor.y_max = 10;

% LoRa/Gateway parameters
gateway = [0, 0, 0];
% centre of footprint at mid-floor
P_t = 14; G_t = 0; G_r = 0;
% Tx power and antenna gains (dBm, dBi)
f = 868e6; f_MHz = f/1e6;
SF = 7; BW = 125e3; NF = 6;
% Spreading factor, bandwidth and noise figure
k_B = 1.38e-23; T0 = 290;

%% Node Deployment
numNodesPerBlock = 20;
% per level
numNodesCorridor = 1;
% only on each floor
positions = [];
nodeArea = {};
for lev = levels
    z = (lev - levels(1)) * floor_height;
    % z offset, starting at level -2
    % Block A nodes
    xA = blockA.x_min + rand(numNodesPerBlock,1)*
    (blockA.x_max - blockA.x_min);
    yA = blockA.y_min + rand(numNodesPerBlock,1)*
    (blockA.y_max - blockA.y_min);
    positions = [positions; xA, yA, z*ones(numNodesPerBlock,1)];
    nodeArea = [nodeArea; repmat({'BlockA'}, numNodesPerBlock,1)];
    % Block B nodes
    xB = blockB.x_min + rand(numNodesPerBlock,1)*
    (blockB.x_max - blockB.x_min);
    yB = blockB.y_min + rand(numNodesPerBlock,1)*
    (blockB.y_max - blockB.y_min);
    positions = [positions; xB, yB, z*ones(numNodesPerBlock,1)];
    nodeArea = [nodeArea; repmat({'BlockB'}, numNodesPerBlock,1)];
    % Corridor nodes
```

```
    xC = corridor.x_min + rand(numNodesCorridor,1)*
    (corridor.x_max - corridor.x_min);
    yC = corridor.y_min + rand(numNodesCorridor,1)*
    (corridor.y_max - corridor.y_min);
    positions = [positions; xC, yC, z*ones(numNodesCorridor,1)];
    nodeArea = [nodeArea; repmat({'Corridor'}, numNodesCorridor,1)];
end

numNodesTotal = size(positions,1);
% Radial 3D distances
distances = sqrt(sum((positions - gateway).^2,2));
% Signed horizontal distances (x-axis)
signedX = positions(:,1) - gateway(1);

%% Wall Loss Assignment for COST-231
numWalls = zeros(numNodesTotal,1);
for i = 1:numNodesTotal
    numWalls(i) = strcmp(nodeArea{i}, 'Corridor')*0 +
~strcmp(nodeArea{i}, 'Corridor')*2;
end

%% Path Loss Models
% Reference path-loss @ 1 m
d0 = 1; PL0 = 20*log10(4*pi*(d0)/(3e8/f));
% COST-231 Multi-Wall
n_cost = 3; L_wall = 8;
PL_cost = PL0 + 10*n_cost*log10(distances/d0) + numWalls*L_wall;
% Log-Distance with shadowing
n_log = 3; sigma = 6;
PL_log = PL0 + 10*n_log*log10(distances/d0) +
sigma*randn(numNodesTotal,1);
% ITU-R P.1238
N_itu = 35; Kf = 4;
floorIdx = positions(:,3)/floor_height + 1;
Lf = Kf*(floorIdx-1);
PL_itu = 20*log10(f_MHz) + N_itu*log10(distances) + Lf - 28;
% 3GPP InH NLOS
PL_3gpp = 32.4 + 20*log10(f_MHz) + 30*log10(distances);

%% RSSI and SNR Calculations
RSSI_cost = P_t + G_t + G_r - PL_cost;
RSSI_log  = P_t + G_t + G_r - PL_log;
RSSI_itu  = P_t + G_t + G_r - PL_itu;
RSSI_3gpp = P_t + G_t + G_r - PL_3gpp;
noise_floor = -174 + 10*log10(BW) + NF;
SNR_cost  = RSSI_cost - noise_floor;
SNR_log   = RSSI_log  - noise_floor;
SNR_itu   = RSSI_itu  - noise_floor;
SNR_3gpp  = RSSI_3gpp - noise_floor;

%% Collision Probability & Throughput (Pure ALOHA)
G_vals = linspace(0.01,1.5,100);
Throughput = G_vals .* exp(-2*G_vals);
P_success = exp(-2*G_vals);
Collision_probability = 1 - P_success;
```

```
%% Packet Loss Rate
dutyCycle = 0.01; T_obs = 3600;
PL   = 42;
CR   = 1; CRC_on = 1; IH = 0; DE = 0; Npreamble = 8;
T_sym      = 2^SF/BW;
T_preamble = (Npreamble+4.25)*T_sym;
tmp        = (8*PL-4*SF+28+16*CRC_on-20*IH)/(4*(SF-2*DE));
N_payload  = 8 + max(ceil(tmp)*(CR+4),0);
T_payload  = N_payload*T_sym;
T_packet   = T_preamble + T_payload;
N_max      = floor((dutyCycle*T_obs)/T_packet);

%% Visualization
% 1. Node Positions by Level (2x2)
figure;
for i = 1:4
    subplot(2,2,i); hold on; grid on;
    z_level = (levels(i) - levels(1)) * floor_height;
    idxA = strcmp(nodeArea,'BlockA')&(abs(positions(:,3)-z_level)<1e-3);
    idxB = strcmp(nodeArea,'BlockB')&(abs(positions(:,3)-z_level)<1e-3);
    idxC = strcmp(nodeArea,'Corridor')&(abs(positions(:,3)-z_level)<1e-
3);
    scatter(positions(idxA,1),positions(idxA,2),'ro','filled');
    scatter(positions(idxB,1),positions(idxB,2),'bs','filled');
    scatter(positions(idxC,1),positions(idxC,2),'g^','filled');
    rectangle('Position',[blockA.x_min,blockA.y_min,blockA.x_max-
    blockA.x_min,blockA.y_max blockA.y_min],
    'EdgeColor','r','LineWidth',2);
    rectangle('Position',[blockB.x_min,blockB.y_min,blockB.x_max-
    blockB.x_min,blockB.y_max blockB.y_min],
    'EdgeColor','b','LineWidth',2);
    rectangle('Position',[corridor.x_min,corridor.y_min,corridor.x_max-
    corridor.x_min,corridor.y_maxcorridor.y_min],
    'EdgeColor','g','LineWidth',2);
    if i == 3

plot(gateway(1),gateway(2),'kp','MarkerSize',12,'MarkerFaceColor','k');
    end
    xlabel('X (m)'); ylabel('Y (m)');
    title(sprintf('Node Positions: Level %d', levels(i)));
    if i == 3
    legend('Block A','Block B','Corridor','Gateway','Location','Best');
    else
    legend('Block A','Block B','Corridor','Location','Best');
    end
    set(gcf, 'Color', 'w')  % gcf = get current figure
end

% 2. Distance Histogram
figure; histogram(distances,20);
xlabel('Distance to Gateway (m)'); ylabel('Node Count');
title('Histogram of 3D Distances');
set(gcf, 'Color', 'w')  % gcf = get current figure
```

```
% 3. RSSI vs Distance by Level
figure;
for i = 1:4
    subplot(2,2,i); hold on; grid on;
    zlvl = (levels(i)-levels(1))*floor_height;
    idx = abs(positions(:,3)-zlvl)<1e-3;
    scatter(signedX(idx), RSSI_cost(idx),'ro','filled');
    scatter(signedX(idx), RSSI_log(idx),'bs','filled');
    scatter(signedX(idx), RSSI_itu(idx),'g^','filled');
    scatter(signedX(idx), RSSI_3gpp(idx),'md','filled');
    set(gcf, 'Color', 'w')  % gcf = get current figure
    xlabel('Distance (m)'); ylabel('RSSI (dBm)'); xlim([-60 60]); ylim([-
    140 -40]);
    title(sprintf('Level %d: RSSI', levels(i)));
    legend('Cost','Log','ITU','3GPP','Location','Best');
end

% 4. SNR vs Distance by Level
figure;
for i = 1:4
    subplot(2,2,i); hold on; grid on;
    zlvl = (levels(i)-levels(1))*floor_height;
    idx = abs(positions(:,3)-zlvl)<1e-3;
    scatter(signedX(idx), SNR_cost(idx),'ro','filled');
    scatter(signedX(idx), SNR_log(idx),'bs','filled');
    scatter(signedX(idx), SNR_itu(idx),'g^','filled');
    scatter(signedX(idx), SNR_3gpp(idx),'md','filled');
    set(gcf, 'Color', 'w')  % gcf = get current figure
    xlabel('Distance (m)'); ylabel('SNR (dB)'); xlim([-60 60]); ylim([-20
    100]);
    title(sprintf('Level %d: SNR', levels(i)));
    legend('Cost','Log','ITU','3GPP','Location','Best');
end

% 5. Pure ALOHA Throughput & Collision
figure; yyaxis left; plot(G_vals,Throughput,'-','LineWidth',2);
ylabel('Throughput S');
yyaxis right; plot(G_vals,Collision_probability,'--','LineWidth',2);
ylabel('Collision Probability');
xlabel('Offered Traffic G');
title('Pure ALOHA Throughput & Collision');
legend('Throughput','Collision','Location','Best');
grid on;
set(gcf, 'Color', 'w')  % gcf = get current figure

% Display duty cycle info
fprintf('Duty Cycle: %.2f%%\n',dutyCycle*100);
fprintf('Observation Period: %d s\n',T_obs);
fprintf('Time-on-Air per Packet: %.2f s\n',T_packet);
fprintf('Max Supported Nodes: %d\n',N_max);

%% 6. PLR vs Number of Nodes for Each Path Loss Model
% Precompute bit rate and packet timing
Rb        = SF*BW/2^SF * 4/(4+CR); % bits/s
T_obs     = 3600; % s (one transmission per node per hour)
```

```
T_packet  = (8*42 + 4)/BW * 2^SF; % s (as before)
N_bits    = 8*42 + 4; % bits/frame

% Number of nodes range
N_vals = 1 : N_max;

% Offered traffic G(N) for pure ALOHA
G = (N_vals .* T_packet) / T_obs;

% MAC layer success
PsuccMAC = exp(-2*G);

% Preallocate
PLR_cost = zeros(size(N_vals));
PLR_log  = zeros(size(N_vals));
PLR_itu  = zeros(size(N_vals));
PLR_3gpp = zeros(size(N_vals));

meanRSSI_dB = [ mean(RSSI_cost)
                mean(RSSI_log)
                mean(RSSI_itu)
                mean(RSSI_3gpp) ];
models = {'COST','Log Dist','ITU','3GPP'};
T = table(models', meanRSSI_dB, ...
          'VariableNames',{'Model','MeanRSSI_dB'});
disp(T);

meanSNR_dB = [ mean(SNR_cost)
               mean(SNR_log)
               mean(SNR_itu)
               mean(SNR_3gpp) ];
models = {'COST','LogDist','ITU','3GPP'};
T2 = table(models', meanSNR_dB, ...
          'VariableNames',{'Model','MeanSNR_dB'});
disp(T2);
meanSNR_lin = 10.^( meanSNR_dB/10 );


% For each model compute average BER, PsuccPHY, combined PLR
models = {'cost','log','itu','3gpp'};
for m = 1:4
    % Use the mean Eb/N0 over all nodes:
    EbN0    = (meanSNR_lin(m) * BW) / Rb;
    BER     = 0.5 * erfc( sqrt(EbN0/2) );
    PsuccPHY = (1 - BER)^N_bits;

    % Combined PLR for each N
    PLR = 1 - (PsuccMAC * PsuccPHY);

    % Store
    switch models{m}
      case 'cost'; PLR_cost = PLR;
      case 'log';  PLR_log  = PLR;
      case 'itu';  PLR_itu  = PLR;
      case '3gpp'; PLR_3gpp = PLR;
```

```
    end
end

% Plot
figure; hold on; grid on;
plot(N_vals, PLR_cost*100, 'r-', 'LineWidth',1.5);
plot(N_vals, PLR_log*100,  'b--','LineWidth',1.5);
plot(N_vals, PLR_itu*100,  'g-.','LineWidth',1.5);
plot(N_vals, PLR_3gpp*100, 'm:','LineWidth',1.5);
xlabel('Number of Nodes'); ylabel('Packet Loss Rate (%)');
title('PLR vs. Number of Nodes for Each Propagation Model');
legend('COST','Log Dist.','ITU','3GPP','Location','Best');
set(gcf,'Color','w');


% 7. Updated RSSI Comparison: All Models vs Excel Measurements
figure;
for i = 1:4
    subplot(2,2,i); hold on; grid on;
    % Compute z-offset for this level
    z_lv = (levels(i) - levels(1)) * floor_height;
    % Load measurements for this level
    sheetName = sprintf('Level %d', levels(i));
    T = readtable('SignalStrengthFinal.xlsx', 'Sheet', sheetName);
    x_meas = T.('DiagonalDistance_m_');
    rssi_meas = T.('RSSI_dBm_');
    % Model data
    idx_model = abs(positions(:,3) - z_lv) < 1e-3;
    x_model = signedX(idx_model);
    % RSSI from each model
    rssi_cost_model = RSSI_cost(idx_model);
    rssi_3gpp_model = RSSI_3gpp(idx_model);
    rssi_itu_model = RSSI_itu(idx_model);
    rssi_log_model = RSSI_log(idx_model);
    % Plot each
    scatter(x_model, rssi_cost_model, 'ro', 'filled');
    scatter(x_model, rssi_3gpp_model, 'md', 'filled');
    scatter(x_model, rssi_itu_model, 'g^', 'filled');
    scatter(x_model, rssi_log_model, 'bs', 'filled');
    scatter(x_meas, rssi_meas, 'kv', 'filled');
    xlabel('Distance (m)'); ylabel('RSSI (dBm)');
    title(sprintf('Level %d: RSSI Comparison', levels(i)));
    legend('COST Model','3GPP Model','ITU Model','Log-Distance
Model','Actual Measurements','Location','Best');
    xlim([-60 60]); ylim([-140 -40]);
    set(gcf, 'Color', 'w');
end

% 8. Updated SNR Comparison: All Models vs Excel Measurements
figure;
for i = 1:4
    subplot(2,2,i); hold on; grid on;
    % Compute z-offset for this level
    z_lv = (levels(i) - levels(1)) * floor_height;
    % Load measurements for this level
```

```
    sheetName = sprintf('Level %d', levels(i));
    T = readtable('SignalStrengthFinal.xlsx', 'Sheet', sheetName);
    x_meas = T.('DiagonalDistance_m_');
    snr_meas = T.('SNR_dB_');
    % Model data
    idx_model = abs(positions(:,3) - z_lv) < 1e-3;
    x_model = signedX(idx_model);
    % SNR from each model
    snr_cost_model = SNR_cost(idx_model);
    snr_3gpp_model = SNR_3gpp(idx_model);
    snr_itu_model = SNR_itu(idx_model);
    snr_log_model = SNR_log(idx_model);
    % Plot each
    scatter(x_model, snr_cost_model, 'ro', 'filled');
    scatter(x_model, snr_3gpp_model, 'md', 'filled');
    scatter(x_model, snr_itu_model, 'g^', 'filled');
    scatter(x_model, snr_log_model, 'bs', 'filled');
    scatter(x_meas, snr_meas, 'kv', 'filled');
    xlabel('Distance (m)'); ylabel('SNR (dB)');
    title(sprintf('Level %d: SNR Comparison', levels(i)));
    legend('COST Model','3GPP Model','ITU Model','Log-Distance
    Model','Actual Measurements','Location','Best');
    xlim([-60 60]); ylim([-20 100]);
    set(gcf, 'Color', 'w');
end
```

Appendix 7: Code excerpts from the data forwarding server

```
mongodb.MongoClient.connect(mongoUri, function (error, database) {
    if (error != null) {
        throw error;
    }
    client.on('message', function (topic, message) {
        var jsonstr = message.toString();
        var doc = JSON.parse(jsonstr);
        if (typeof doc.payload_fields.temperature_1 != "undefined") {
            var collection =
            database.collection(config.mongodb.collection);
            var datetimestr = doc.metadata.time.toString();
            var datetime = new Date(datetimestr);
            datetime.setHours(datetime.getHours() + 2);

            if (doc.dev_id.slice(4,5) == '-') {
                var floor = Number(doc.dev_id.slice(5,6));
                var block = doc.dev_id.slice(6,7);
                var room = Number(doc.dev_id.slice(7,9));
            } else {

                var floor = Number(doc.dev_id.slice(4,5));
                var block = doc.dev_id.slice(5,6);
                var room = Number(doc.dev_id.slice(6,8));
            }
            var messageObject = {
                app_id: doc.app_id,
                dev_id: doc.dev_id,
                floor: floor,
                block: block,
                room: room,
                hardware_serial: doc.hardware_serial,
                port: doc.port,
                counter: doc.counter,
                payload_raw: doc.payload_raw,
                battery_voltage_V: doc.payload_fields.analog_in_3,
                datetime: datetime,
                frequency: doc.metadata.frequency,
                modulation: doc.metadata.modulation,
                data_rate: doc.metadata.data_rate,
                coding_rate: doc.metadata.coding_rate,
                airtime: doc.metadata.airtime,
                gateway: doc.metadata.gateways[0].gtw_id,
                channel: doc.metadata.gateways[0].channel,
                rssi: doc.metadata.gateways[0].rssi,
                snr: doc.metadata.gateways[0].snr
            };
            collection.insert(messageObject, function (error, result) {
                if (error != null) {
                    console.log("ERROR: " + error);
                }
            });
```

```
            var collection =
            database.collection(config.mongodb.collection2);

            if (doc.payload_fields.temperature_1 >= 20 &&
               doc.payload_fields.temperature_1 <= 26) {
                var t1_thermal_comfort_index = 1;
            } else if ((doc.payload_fields.temperature_1 >= 17 &&
                        doc.payload_fields.temperature_1 < 20) ||
                       (doc.payload_fields.temperature_1 > 26 &&
                        doc.payload_fields.temperature_1 <= 29)) {
                var t1_thermal_comfort_index = 2;
            } else if ((doc.payload_fields.temperature_1 >= 7 &&
                        doc.payload_fields.temperature_1 < 17) ||
                       (doc.payload_fields.temperature_1 > 29 &&
                        doc.payload_fields.temperature_1 <= 39)) {
                var t1_thermal_comfort_index = 3;
            } else if ((doc.payload_fields.temperature_1 >= 0 &&
                        doc.payload_fields.temperature_1 < 7) ||
                       (doc.payload_fields.temperature_1 > 39 &&
                        doc.payload_fields.temperature_1 <= 45)) {
                var t1_thermal_comfort_index = 4;
            } else {
                var t1_thermal_comfort_index = 5;
            }
            if (doc.payload_fields.relative_humidity_2 >= 40 &&
                doc.payload_fields.relative_humidity_2 < 70) {
                var t2_thermal_comfort_index = 1;
            } else if ((doc.payload_fields.relative_humidity_2 >= 70 &&
                        doc.payload_fields.relative_humidity_2 < 80)) {
                var t2_thermal_comfort_index = 2;
            } else if ((doc.payload_fields.relative_humidity_2 >= 80 &&
                        doc.payload_fields.relative_humidity_2 < 90)) {
                var t2_thermal_comfort_index = 3;
            } else if ((doc.payload_fields.relative_humidity_2 >= 90 &&
                        doc.payload_fields.relative_humidity_2 < 100)) {
                var t2_thermal_comfort_index = 4;
            } else {
                var t2_thermal_comfort_index = 5;
            }
            var thermal_comfort_index =
Math.max(t1_thermal_comfort_index,
                t2_thermal_comfort_index);
            if (doc.payload_fields.luminosity_6 < 600) {
                var t1_air_quality_index = 1;
                var t1_air_quality_index_ratio =
                    doc.payload_fields.luminosity_6 / 600;
            } else if (doc.payload_fields.luminosity_6 < 1000) {
                var t1_air_quality_index = 2;
                var t1_air_quality_index_ratio = 1 +
                   (doc.payload_fields.luminosity_6 / 1000);
            } else if (doc.payload_fields.luminosity_6 < 1500) {
                var t1_air_quality_index = 3;
                var t1_air_quality_index_ratio = 2 +
                    (doc.payload_fields.luminosity_6 / 1500);
            } else if (doc.payload_fields.luminosity_6 < 2000) {
```

```
    var t1_air_quality_index = 4;
    var t1_air_quality_index_ratio = 3 +
        doc.payload_fields.luminosity_6 / 2000;
} else {
    var t1_air_quality_index = 5;
    var t1_air_quality_index_ratio = 4 +
        (doc.payload_fields.luminosity_6 / 2000);
}
if (doc.payload_fields.luminosity_4 < 50) {
    var t2_air_quality_index = 1;
    var t2_air_quality_index_ratio =
        doc.payload_fields.luminosity_4 / 50;
} else if (doc.payload_fields.luminosity_4 < 100) {
    var t2_air_quality_index = 2;
    var t2_air_quality_index_ratio = 1 +
        (doc.payload_fields.luminosity_4 / 100);
} else if (doc.payload_fields.luminosity_4 < 300) {
    var t2_air_quality_index = 3;
    var t2_air_quality_index_ratio = 2 +
        (doc.payload_fields.luminosity_4 / 300);
} else if (doc.payload_fields.luminosity_4 < 600) {
    var t2_air_quality_index = 4;
    var t2_air_quality_index_ratio = 3 +
        (doc.payload_fields.luminosity_4 / 600);
} else {
    var t2_air_quality_index = 5;
    var t2_air_quality_index_ratio = 4 +
        (doc.payload_fields.luminosity_4 / 600);
}
if (doc.payload_fields.analog_in_10 < 20) {
    var t3_air_quality_index = 1;
    var t3_air_quality_index_ratio =
        doc.payload_fields.analog_in_10 / 20;
} else if (doc.payload_fields.analog_in_10 < 35) {
    var t3_air_quality_index = 2;
    var t3_air_quality_index_ratio = 1 +
        (doc.payload_fields.analog_in_10 / 35);
} else if (doc.payload_fields.analog_in_10 < 50) {
    var t3_air_quality_index = 3;
    var t3_air_quality_index_ratio = 2 +
       (doc.payload_fields.analog_in_10 / 50);
} else if (doc.payload_fields.analog_in_10 < 100) {
    var t3_air_quality_index = 4;
    var t3_air_quality_index_ratio = 3 +
        (doc.payload_fields.analog_in_10 / 100);
} else {
    var t3_air_quality_index = 5;
    var t3_air_quality_index_ratio = 4 +
        (doc.payload_fields.analog_in_10 / 100);
}
if (doc.payload_fields.analog_in_8 < 10) {
    var t4_air_quality_index = 1;
    var t4_air_quality_index_ratio =
        doc.payload_fields.analog_in_8 / 10;
} else if (doc.payload_fields.analog_in_8 < 20) {
```

```
    var t4_air_quality_index = 2;
    var t4_air_quality_index_ratio = 1 +
       (doc.payload_fields.analog_in_8 / 20);
} else if (doc.payload_fields.analog_in_8 < 25) {
    var t4_air_quality_index = 3;
    var t4_air_quality_index_ratio = 2 +
       (doc.payload_fields.analog_in_8 / 25);
} else if (doc.payload_fields.analog_in_8 < 50) {
    var t4_air_quality_index = 4;
    var t4_air_quality_index_ratio = 3 +
        (doc.payload_fields.analog_in_8 / 50);
} else {
    var t4_air_quality_index = 5;
    var t4_air_quality_index_ratio = 4 +
        (doc.payload_fields.analog_in_8 / 50);
}
var air_quality_index_ratio =
    Math.max(t1_air_quality_index_ratio,
    t2_air_quality_index_ratio, t3_air_quality_index_ratio,
    t4_air_quality_index_ratio);

if (t1_air_quality_index_ratio == air_quality_index_ratio) {
    var main_pollutant = "CO2";
    var air_quality_index = t1_air_quality_index;
} else if (t2_air_quality_index_ratio ==
          air_quality_index_ratio) {
    var main_pollutant = "VOC";
    var air_quality_index = t2_air_quality_index;
} else if (t3_air_quality_index_ratio ==
         air_quality_index_ratio) {
    var main_pollutant = "PM10";
    var air_quality_index = t3_air_quality_index;
} else if (t4_air_quality_index_ratio ==
         air_quality_index_ratio) {
    var main_pollutant = "PM2.5";
    var air_quality_index = t4_air_quality_index;
}
var messageObject = {
    dev_id: doc.dev_id,
    floor: floor,
    block: block,
    room: room,
    temperature_C: doc.payload_fields.temperature_1,
    relative_humidity_RH:
    doc.payload_fields.relative_humidity_2,
    barometric_pressure_hPa:
    doc.payload_fields.barometric_pressure_3,
    t_voc_ppb: doc.payload_fields.luminosity_4,
    e_co2_ppm: doc.payload_fields.luminosity_5,
    co2_ppm: doc.payload_fields.luminosity_6,
    pm_1_0_µg_m3: doc.payload_fields.analog_in_7,
    pm_2_5_µg_m3: doc.payload_fields.analog_in_8,
    pm_4_0_µg_m3: doc.payload_fields.analog_in_9,
    pm_10_0_µg_m3: doc.payload_fields.analog_in_10,
```

```
                typical_particle_size_µm:
doc.payload_fields.analog_in_11,
                air_quality_index: air_quality_index,
                thermal_comfort_index: thermal_comfort_index,
                main_pollutant: main_pollutant,
                datetime: datetime
            };
            collection.insert(messageObject, function (error, result) {
                if (error != null) {
                    console.log("ERROR: " + error);
                }
            });
            var collection =
            database.collection(config.mongodb.collection3);
            collection.update({dev_id: doc.dev_id}, {$set:{aqi:
            air_quality_index, tci: thermal_comfort_index}},
{multi:true});
        }
    });
});
```

Appendix 8: Writing Tools

In preparing this dissertation, generative AI tools were employed to enhance clarity, coherence, and grammatical precision. ChatGPT and Gemini were used specifically to assist with rephrasing, refining technical explanations, and improving sentence structure where appropriate. These tools did not create original content or analysis; rather, they were applied solely to support the writing process and strengthen overall readability.